



**STUDY ON 3D FORWARD MODELING & INVERSION OF SURFACE-BOREHOLE  
ELECTROMAGNETIC DATA**

**Par**

**Chong Liu**

**Sous la direction de**

**La professeure Li Zhen CHENG**

**et les co-directions des professeurs Fouad ERCHIQUI**

**et Michel CHOUTEAU**

**Thèse présentée à l'Université du Québec à Chicoutimi en vue de l'obtention du grade de  
Philosophiae Doctor (Ph.D.) en Doctorat en ingénierie**

**Soutenue le 25 June 2021**

Jury :

M. Marin Ene, Ph.D., Université du Québec en Abitibi-Témiscamingue, Président du Jury

M. Jiateng Guo, Ph.D., Northeastern University, Membre externe ou rapporteur

Mme Li Zhen Cheng, Ph.D., Université du Québec en Abitibi-Témiscamingue, Membre interne

M. Michel Chouteau, Ph.D., Polytechnique Montréal, Université de Montréal, Membre interne

Québec, Canada

© Chong Liu, 2021



# BIBLIOTHÈQUE

CÉGEP DE L'ABITIBI-TÉMISCAMINGUE  
UNIVERSITÉ DU QUÉBEC EN ABITIBI-TÉMISCAMINGUE

## Mise en garde

La bibliothèque du Cégep de l'Abitibi-Témiscamingue et de l'Université du Québec en Abitibi-Témiscamingue (UQAT) a obtenu l'autorisation de l'auteur de ce document afin de diffuser, dans un but non lucratif, une copie de son œuvre dans [Depositum](#), site d'archives numériques, gratuit et accessible à tous. L'auteur conserve néanmoins ses droits de propriété intellectuelle, dont son droit d'auteur, sur cette œuvre.

## Warning

The library of the Cégep de l'Abitibi-Témiscamingue and the Université du Québec en Abitibi-Témiscamingue (UQAT) obtained the permission of the author to use a copy of this document for nonprofit purposes in order to put it in the open archives [Depositum](#), which is free and accessible to all. The author retains ownership of the copyright on this document.

## TABLE OF CONTENTS

TABLE OF CONTENTS.....	i
LIST OF TABLES.....	v
LIST OF FIGURES.....	vi
LIST OF SYMBOLS AND ABBREVIATIONS.....	xii
ACKNOWLEDGMENTS.....	xv
ABSTRACT.....	xvii
CHAPTER 1 INTRODUCTION.....	1
1.1 Problems statement.....	1
1.1.1 Context of the Ph.D. study.....	1
1.1.2 An overview of BHEM forward modeling.....	5
1.1.3 An overview of BHEM inversion.....	9
1.2 Research objectives.....	16
1.3 Methodology and Originality.....	17
1.4 Outline of the thesis.....	18
CHAPTER 2 DESIGN OF A 3D MODEL CONSTRUCTOR.....	20
2.1 Development of an interface for model design.....	20
2.2 Measurement system parameters.....	22
2.3 Design of 3D model and discretization.....	27
2.3.1 3D model design.....	27

2.3.2 Discretization.....	28
2.4 Data for BHTEM forward modeling and inversion.....	30
2.5 Visualization .....	33
2.6 Conclusions .....	35
CHAPTER 3 3D PARALLEL SURFACE-BOREHOLE TEM FORWARD MODELING WITH MULTIPLE MESHES .....	36
3.1 Introduction .....	36
3.2 Edge-based finite element in TEM forward modeling.....	38
3.3 Parallelization.....	41
3.3.1 Design of parallel algorithms .....	41
3.3.2 Test of the parallel computation and the efficiency analysis .....	45
3.4 Multiple meshes technology .....	51
3.4.1 Multiple meshes design.....	52
3.4.2 Analysis of multiple meshes.....	55
3.4.3 Parallel computing with multiple meshes.....	59
3.5 Conclusions .....	61
CHAPTER 4 IMPROVEMENT OF THE EFFICIENCY OF TIME-DOMAIN ELECTROMAGNETIC MEASUREMENT.....	62
4.1 Introduction .....	62
4.2 Pulse width study .....	65
4.2.1 Theoretical analysis of pulse width.....	65
4.2.2 Effect of pulse width .....	68

4.3 Simulations and verifications.....	71
4.3.1 Surface-borehole TEM.....	72
4.3.2 Ground TEM.....	74
4.3.3 Airborne TEM.....	74
4.4 Formula of optimal pulse width and measurement time.....	75
4.4.1 Optimal pulse width.....	75
4.4.2 Robustness of the method.....	77
4.5 Conclusions.....	82
 CHAPTER 5 3D GAUSS-NEWTON INVERSION OF SURFACE-BOREHOLE TEM	
DATA.....	83
5.1 Introduction.....	83
5.2 Basic theory and improvement.....	87
5.2.1 Governing equations.....	87
5.2.2 Regularized Gauss-Newton method.....	89
5.2.3 Jacobian matrix.....	94
5.2.4 Improvement in TEM data inversion.....	97
5.3. Applications of Gauss-Newton inversion to modeled data.....	102
5.3.1 Case 1: one conductive prism.....	102
5.3.2 Case 2: two conductive prisms.....	107
5.3.3 Case study.....	110
5.4. Conclusions.....	114
 CHAPTER 6 CONCLUSIONS, MAIN CONTRIBUTIONS AND DISCUSSION.....	
	116

REFERENCES .....120

## LIST OF TABLES

TABLE 1.1: LIST OF AVAILABLE BHTEM INVERSION PROGRAMS .....	15
TABLE 2.1: LIST OF THE MODULES AND CONTROL FILES IN THE 3D MODEL BUILDER .....	21
TABLE 3.1: THE PARALLEL EFFICIENCY (E) FOR EVEN/UNEVEN MODE MPI PARALLELIZATIONS.....	46
TABLE 3.2: COMPUTATION TIME FOR OPENMP PARALLELIZATION IN ONE FREQUENCY POINT (0.1Hz).....	48
TABLE 3.3: COMPUTATION TIME FOR HYBRID MPI/OPENMP WITH THE UNEVEN MODE ON THE ENTIRE FORWARD MODELING.....	50
TABLE 3.4: SPECIFICATIONS OF GRIDS .....	55
TABLE 3.5: SPECIFICATIONS OF GRIDS AND MESHES. ....	57
TABLE 3.6: SPEEDUP OF TYPE A AND TYPE B WITH MULTIPLE MESHES (ONLY THREE CASES (1, 5, AND 9 PROCESSORS) ARE USED IN TYPE B) .....	60
TABLE 4.1: PARAMETERS OF SOME COMMON TEM SYSTEMS WITH TRAPEZOIDAL OR SQUARE WAVEFORMS. ....	71
TABLE 5.1: LOCATION AND GEOMETRY FOR THE 14 BOREHOLES IN WHICH RECEIVER DATA WERE COLLECTED .....	111

## LIST OF FIGURES

FIGURE 1.1: WORKFLOW OF THE PROJECT .....	17
FIGURE 2.1: THE GENERAL FLOW CHART OF DATA AND THE MAIN MODULES FOR TEM EXPLORATION .....	20
FIGURE 2.2: SETTING TX ON THE SURFACE AND RX IN THE BOREHOLES. THE RELATIVE COORDINATE SYSTEM IS USED FOR ALL THE FIGURES IN THIS THESIS. ONE ALSO CAN USE THE GEOGRAPHIC COORDINATE.....	23
FIGURE 2.3: THE DEFINITION OF BOREHOLE PARAMETERS, $\alpha$ IS THE DIP ANGLE BETWEEN THE BOREHOLE AND HORIZONTAL PLANE, $\Gamma$ IS THE AZIMUTH ANGLE BETWEEN THE NORTH AND SURVEY AZIMUTH.....	24
FIGURE 2.4: TRAPEZOIDAL WAVEFORM .....	25
FIGURE 2.5: HALF-SINE WAVEFORM .....	25
FIGURE 2.6: TRIANGULAR WAVEFORM .....	26
FIGURE 2.7: THE DISTRIBUTION OF PRIMARY FIELD AND THE COUPLING BETWEEN TX, RX, AND CONDUCTOR.....	26
FIGURE 2.8: THE GEOLOGICAL MODEL .....	29
FIGURE 2.9: THE TABLE 1 SHOWS INITIAL RESISTIVITY VALUES IN THE GEOLOGICAL MODEL (LITHOLOGIES FOR GEO-MODEL). THE TABLE 2 SHOWS THE RESISTIVITY VALUES AFTER RE-MESHING THE MODEL (LITHOLOGIES AFTER MESHING).....	30
FIGURE 2.10: BHTEM FORWARD MODELING AND THREE-COMPONENT RESPONSES (A, U, V) .....	31
FIGURE 2.11: THE DEFINITION OF THREE COMPONENTS OF THE BHTEM FIELD, IN WHICH THE AZIMUTH OF THE DRILLHOLE IS REGARDED AS A REFERENCE. A: PARALLEL TO	

DRILLHOLE TRAJECTORY. U: IN THE VERTICAL PLANE CONTAINING A. V:  
PERPENDICULAR TO A AND U IN A RIGHT-HAND COORDINATE SYSTEM (BISHOP, 1996;  
HUGHES, 1996).....32

FIGURE 2.12: BHTEM RESPONSE ALONG A BOREHOLE (UPPER) AND THE DECAY CURVES AT  
DIFFERENT SURVEY STATIONS (BOTTOM) .....33

FIGURE 2.13: 3D VISUALIZATION OF INVERSION RESULT .....34

FIGURE 2.14: THE SCATTERPLOT TO SHOW THE DISTRIBUTION OF RESISTIVITY FROM THE  
INVERSION RESULT, THE VERTICAL AXIS IS USED TO SEPARATE THE SAME VALUES. ....35

FIGURE 3.1: SKETCH OF THE CONFIGURATION OF SURFACE-BOREHOLE TEM, AND THE  
ILLUSTRATION OF THE PRIMARY FIELD GENERATED BY THE LOOP SOURCE AND THE  
SECONDARY MAGNETIC FIELD INDUCED IN THE CONDUCTOR. ....39

FIGURE 3.2: THE PROCEDURE OF PARALLEL COMPUTATION BASED ON MPI, (A) MASTER  
PROCESSOR, (B) SLAVE PROCESSORS, AND (C) FURTHER PARALLELIZATION BASED ON  
OPENMP .....42

FIGURE 3.3: RESULTS OF MPI PARALLEL COMPUTATION ON EVEN/UNEVEN MODE: THE  
COMPUTATION TIME (A), THE SPEEDUP (B). ....46

FIGURE 3.4: AVERAGE OF ACCUMULATIVELY CONSUMED TIME FOR ALL FREQUENCIES WHEN A  
DIFFERENT NUMBER OF PROCESSORS IS USED, AND THE INCREASED RATE RELATIVE TO  
THE AVERAGE TIME IN THE SEQUENTIAL COMPUTATION. ON THE Y AXIS,  $time = \frac{1}{p} \sum_i^a t_i$ ,  
T<sub>1</sub> IS THE COMPUTATION TIME OF I<sup>TH</sup> ASSIGNMENT IN ONE PROCESSOR, A IS THE NUMBER  
OF ASSIGNMENTS. ....48

FIGURE 3.5: GEOMETRY OF THE FINE AND COARSE CELLS IN ONE SLICE.....53

FIGURE 3.6: TIME TAKEN AT DIFFERENT FREQUENCIES .....56

FIGURE 3.7: COMPARISONS OF TIME BETWEEN TWO TYPES OF MESHES.....	58
FIGURE 3.8: SPEEDUP OF THE PARALLELIZED SURFACE-BOREHOLE TEM WITH MULTIPLE MESHES. ....	60
FIGURE 4.1: THE TRANSMITTER WAVEFORMS USED IN THIS STUDY, (A) SQUARE PULSE, (B) TRAPEZOIDAL PULSE .....	65
FIGURE 4.2: THE RATIO (R) AS A FUNCTION OF THE RATIO OF THE PULSE WIDTH TO THE TARGET TIME CONSTANT. (A) SQUARE WAVEFORM, (B) TRAPEZOIDAL WAVEFORM WITH A FIXED RAMP TURN-OFF TIME (D=0.1, 0.3 AND 0.5MS). THE DUTY CYCLES FOR BOTH PULSES ARE 0.5. ....	68
FIGURE 4.3: THE MODEL M1 CONSISTS OF A PRISM WITH $1\Omega\cdot\text{M}$ RESISTIVITY IN A $500\Omega\cdot\text{M}$ HALF-SPACE, (A) TOP VIEW, (B) SECTION VIEW.....	69
FIGURE 4.4: SURFACE-BOREHOLE TEM DECAYS (A COMPONENTS) AND THE RATIO R WITH DIFFERENT PULSE WIDTHS FOR THE MODEL M1, (A, B) SQUARE PULSE IN BH1, (C, D) SQUARE PULSE IN BH2, (E, F) TRAPEZOIDAL PULSE IN BH1, (G, H) TRAPEZOIDAL PULSE IN BH2.....	70
FIGURE 4.5: THE LAYERED MODEL M2, AND THE CONFIGURATION OF THE TRANSMITTER LOOP (Tx), THE BOREHOLE BH, AND THE SURVEY LINE. ....	72
FIGURE 4.6: DECAYS OF TEM RESPONSES GENERATED BY SQUARE AND TRAPEZOIDAL PULSES, AND THE RATIO R WITH VARYING PULSE WIDTHS FOR THE MODEL M2. THE SIMULATIONS ARE IMPLEMENTED FOR SURFACE-BOREHOLE TEM (A TO D), GROUND TEM (E TO H), AND AIRBORNE TEM (I TO L). ....	73
FIGURE 4.7: RATIO R AS THE FUNCTION OF TIME TO DIFFERENT VALUES OF $(\Delta/\tau)$ FOR THE MODEL M1 WITH SURFACE-BOREHOLE TEM (A), GROUND TEM (B) AND AIRBORNE TEM (C).....	76

FIGURE 4.8: PARAMETER $\Delta/\tau$ AS FUNCTION OF TIME T FOR R = 80% AND 90%.....	77
FIGURE 4.9: (A) RANDOM BACKGROUND NOISE. (B) SURFACE-BOREHOLE TEM NOISY SIGNAL, (C) GROUND TEM NOISY SIGNAL, (D) AIRBORNE TEM NOISY SIGNAL FOR THE MODEL M1. T <sub>0</sub> INDICATES WHEN THE NOISE IS LARGER THAN THE SIGNAL.....	78
FIGURE 4.10: SIGNAL-TO-NOISE RATIO (SNR) FOR EACH CHANNEL, SURFACE-BOREHOLE TEM (A), GROUND TEM (B) AND AIRBORNE TEM (C).....	79
FIGURE 4.11: RATIO R AS THE FUNCTION OF TIME TO DIFFERENT VALUES OF ( $\Delta/\tau$ ) FOR THE NOISY DATA OF SURFACE-BOREHOLE TEM (A, B), GROUND TEM (C,D) AND AIRBORNE TEM (E,F). 1nT/S NOISY LEVEL IN (A, C, E), 10nT/S NOISY LEVEL IN (B, D, F). MODEL M1 IS USED FOR GENERATING THEORETICAL DATA. T <sub>0</sub> INDICATES WHEN THE NOISE LEVEL IS LARGER THAN THE SIGNAL.....	81
FIGURE 5.1: BHTEM SYSTEM IN A DISCRETIZED 3D SPACE.....	88
FIGURE 5.2: (A) SCHEMATIC OVERVIEW OF THE BHTEM INVERSION, (B) MODIFICATION AND IMPROVEMENT OF THE PREDICTED MODEL IN THE INVERSION PROCESS.....	99
FIGURE 5.3: SCATTER PLOT OF RESISTIVITY DISTRIBUTION.....	100
FIGURE 5.4: GENERAL OUTLINE MAP OF INVERSION RESULTS, (A) TOP VIEW, (B) SECTION VIEW. (C) TOP VIEW AND (D) SECTION VIEW AFTER INVERSION RESULTS ARE IMPROVED WITH NS, 3D TRACE ENVELOPE, AND FALSE TARGETS ELIMINATION. R IS THE DISTANCE TO THE BOUNDARY OF C <sub>1</sub> .....	101
FIGURE 5.5: CASE 1 – A 5 $\Omega\cdot\text{M}$ CONDUCTIVE PRISM BURIED IN A UNIFORM 1,000 $\Omega\cdot\text{M}$ HALF- SPACE, TWO BOREHOLES (BH1 AND BH2) ARE USED.....	103
FIGURE 5.6: FORWARD MODELING DATA ALONG THE BOREHOLES (BH1 AND BH2) ON CASE 1 .....	103

FIGURE 5.7: INVERSION RESULTS OF CASE 1 WITH A UNIFORM  $1000 \Omega \cdot \text{M}$  INITIAL MODEL. (A) TOP VIEW AT  $Z = -180\text{M}$ , (B) SECTION VIEW AT  $Y = 210\text{M}$ , (C) CROSS-SECTIONS VIEW OF THE PREDICTED MODEL (A, B AND C SHARE THE SAME COLOR BAR), AND (D) BODIES DEFINED BY ISOSURFACES OF  $5 \Omega \cdot \text{M}$  ..... 104

FIGURE 5.8: INVERSION RESULTS OF CASE 1 WITH ISOSURFACE, NS, 3D TRACE ENVELOPE AND FALSE TARGET ELIMINATION. (A) TOP VIEW AT  $Z = -180\text{M}$ , (B) SECTION VIEW AT  $Y = 210\text{M}$ , (C) CROSS-SECTIONS VIEW OF THE PREDICTED MODEL (A, B AND C SHARE THE SAME COLOR BAR), AND (D) BODIES DEFINED BY ISOSURFACES OF  $5 \Omega \cdot \text{M}$  ..... 105

FIGURE 5.9: (A) DATA MISFIT OF 3D INVERSION FOR CASE 1, (B) SKETCH OF IMITATED INVERSION PROCESS WITH OUR STRATEGY ..... 106

FIGURE 5.10: CASE 2 – TWO  $5 \Omega \cdot \text{M}$  CONDUCTIVE PRISMS BURIED IN A UNIFORM  $1000 \Omega \cdot \text{M}$  HALF-SPACE, THREE BOREHOLES ARE USED. .... 107

FIGURE 5.11: INVERSION RESULTS OF CASE 2 WITH A UNIFORM  $1000 \Omega \cdot \text{M}$  HOST ROCK MODEL. (A) TOP VIEW AT  $Z = -170\text{M}$ , (B) SECTION VIEW AT  $Y = 180\text{M}$ , (C) CUT-AWAY VIEW OF THE PREDICTED MODEL (A, B AND C SHARE THE SAME COLOR BAR), AND (D) BODIES DEFINED BY ISOSURFACES OF  $10 \Omega \cdot \text{M}$ . .... 108

FIGURE 5.12: INVERSION RESULTS OF CASE 2 WITH ISOSURFACE, NEIGHBORHOOD SEARCH, 3D TRACE ENVELOPE, AND FALSE TARGET ELIMINATION. (A) TOP VIEW AT  $Z = -170\text{M}$ , (B) SECTION VIEW AT  $Y = 180\text{M}$ , (C) CUT-AWAY VIEW OF THE PREDICTED MODEL (A, B AND C SHARE THE SAME COLOR BAR), AND (D) INTERPRETATION BASED ON THE INVERSION RESULTS. .... 109

FIGURE 5.13: LOCATION OF THE SURVEY AREA AND GEOLOGY OF THE ISO AREA (MODIFIED FROM CHENG ET. AL., 2006); THE CONFIGURATION OF THE MEASUREMENT SYSTEM IS

SHOWN. A RELATIVE COORDINATE SYSTEM IN METERS IS USED. ONE TRANSMITTER LOOP (TX) IS LOCATED AT (350M, 400M, 0) AT THE SURFACE, 14 BOREHOLES ARE AROUND TX.

..... 112

FIGURE 5.14: INVERSION RESULTS FOR THE ISO VMS DEPOSIT WITH (A) A 1000  $\Omega \cdot \text{M}$  UNIFORM HALF-SPACE INITIAL MODEL, (B) IMPROVEMENT WITH ISOSURFACE, NEIGHBORHOOD SEARCH, 3D TRACE ENVELOPE, AND FALSE TARGETS ELIMINATION. (C) INTERPRETATION BASED ON THE INVERSION RESULTS. (D) THE PROFILE E-F (ABOUT 269M) THROUGH BOREHOLES M7, M9, AND M77, AND THE PROFILE F-G (ABOUT 325M) FROM BOREHOLES M77 TO M30..... 113

## LIST OF SYMBOLS AND ABBREVIATIONS

<b>Symbol or Abbreviation:</b>	<b>Definition:</b>
<b>E</b>	Electric field
<b>H</b>	Magnetic field
<b><math>\mathbf{J}_e</math></b>	Current density
$\omega$	Angular frequency
$\sigma$	Electric conductivity
$\sigma_s$	Anomalous conductivity
$\mu_0$	Magnetic permeability
$\epsilon$	Dielectric permittivity
$\rho$	The density of charge or resistivity
$\nabla$	Laplace operator
<b>A</b>	Magnetic vector potential
<b><math>A^P</math></b>	Primary magnetic vector potential
<b><math>A^S</math></b>	Secondary magnetic vector potential
<b>K</b>	Global stiffness matrix
<b>b</b>	Vector
$T_1$	Sequential computation time
$p$	The number of processors in the parallel calculation
$T_P$	Parallel computation time on $p$ processors
<b>S</b>	Speedup – the ratio of serial run time to parallel run time ( $S = T_1/T_P$ )

e	Parallel efficiency is the ratio of speedup to the number of processors used ( $e = S/p$ )
d	Distance
$V$	Induced voltage by a finite-width pulse
$V_{\Delta_x}$	Induced voltage by infinite-width pulse
R	The ratio of $V$ to $V_{\Delta_x}$
$\tau$	Time constant
t	time
$\Phi$	Objective function
$\mathbf{W}_d$	Data weighting matrix
$\mathbf{W}_m$	Model weighting matrix
$\mathbf{C}$	Weighting matrix related to $\mathbf{W}_d$ and $\mathbf{W}_m$
$\mathbf{d}$	Field data (one or more components of $\mathbf{A}$ , $\mathbf{U}$ and $\mathbf{V}$ )
$\Delta\mathbf{d}$	Error vector between modeling responses and field data
$\mathbf{m}$	Model parameters
$\mathbf{m}_0$	Initial model parameters
$\lambda$	Regularization parameter
$\mathbf{I}$	Unit matrix
$\mathbf{J}$	Sensitivity matrix
s	Step size
r	Residual
M	The number of model parameters

N	The number of observations
1D	One dimension
2D	Two dimensions
3D	Three dimensions
EM	Electromagnetic
TEM / TDEM	Time domain electromagnetic method
FDEM	Frequency domain EM method
BHTEM	Surface-borehole TEM method
BHEM	Surface-borehole EM method
SNR	Signal-to-noise ratio
FEM	Finite element method
Tx	Transmitter
Rx	Receiver
MPI	Message passing interface
OpenMP	Open multi-processing
GN	Gauss-Newton method
CG	Conjugate gradient
VMS	Volcanogenic massive sulfide

## ACKNOWLEDGMENTS

First and foremost, I am grateful to my supervisor, Prof. Li Zhen Cheng of the Université du Québec en Abitibi-Témiscamingue, for her enormous support and encouragement in my research and her contribution to the thesis. Through a large number of valuable discussions with Prof Cheng, she provided me with helpful comments and suggestions that inspired me to guide me in the right direction so that I can fully realize my ideas. I am very grateful to Prof. Cheng for her confidence, patience, and assistance in my research.

I would like to thank my vice-supervisor, Prof. Fouad Erchiqui of the Université du Québec en Abitibi-Témiscamingue, for his generous support in my Ph.D. program. His insightful suggestions are very helpful for resolving my problems in my research.

I would like to thank my vice-supervisor, Prof. Michel Chouteau from the École Polytechnique de Montréal, for his comments and insightful advice. I was inspired by his passion and extensive knowledge. His valuable comments on my research are essential to improve my work and to guide me in the continuation of my future research.

I would like to express my special thanks to the members of the committee: Prof. Jiateng Guo, Prof. Marin Ene, whose comments and suggestions contribute to the improvement of this thesis.

I am extremely grateful to my family for always being there by my side with their love, encouragement and support. Especially to my parents Fanci Meng and Chaogen Liu, my

younger brother Chuanyun Liu, and my wife Bomei Zheng, who provided me with unconditional and daily support.

This work was funded by le Fonds de Recherche du Québec – Nature et Technologies (FRQNT) and the industry partners Abitibi Geophysique Inc. and Agnico Eagle Mines Limited. I would like to acknowledge my colleagues and all the persons at the Université du Québec en Abitibi-Témiscamingue for their generous help throughout my doctoral program. I also would like to thank the Electromagnetic Modeling Group – CSIRO Exploration & Mining in Australia for making its excellent code Loki available to the EM community.

I thank all of you who played a larger role in extending my knowledge and research capability with your encouragement and support.

Thank you all very much!

*Chong Liu*

## ABSTRACT

The purpose of this research is to develop an interpretive tool to meet the requirements of deep mineral exploration. Therefore, we carried out a series of research work as part of a doctoral training program and achieved the relevant objectives below.

The core of this doctoral thesis is the development of 3D modeling tools to interpret the electromagnetic data collected in boreholes. First, a 3D model creation tool is designed, with which we can easily build a 3D geological model from sections and quickly discretize it. The sections could be true geological cross-sections or from a conceptual geological model. The utility of this tool is to facilitate the tests of the algorithms developed within the framework of this thesis, in order to model the electromagnetic responses in various geological situations and allow to easily change the parameters of the geophysical measurement system.

Two parallelization algorithms, MPI-based and hybrid MPI/OpenMP-based methods, are designed for surface-borehole time domain electromagnetic (BHTEM) forward modeling. The BHTEM responses are calculated from anomalous regions distributed in a 3D model (discretized into cells). The forward modeling additionally uses multiple meshes, fine meshes are used for the anomalous region in the high-frequency range and coarser meshes for geological background in the low-frequency range. Based on varying meshes for different frequency ranges, the parallel computation greatly reduces the computation time of the TEM forward modeling.

An optimal survey design benefits from quick forward modeling. We found that the target BHTEM response depends upon the transmitting pulse width, target time constant, and the duration of measurement time. We proposed the formula with respect to the three variables to design optimal pulse widths in advance for different off-times in order to maximize the efficiency of TEM measurement in the field.

Finally, a 3D BHTEM inversion algorithm is developed based on the Gauss-Newton method with high spatial resolution. By introducing the isosurface, neighborhood anomalies search, 3D trace envelope, and false targets elimination into the inversion process, the predicted model is improved through iterations and interactions between the computation and the user intervention.

# CHAPTER 1

## INTRODUCTION

### **1.1 Problems statement**

The theme of my research is the development of a new tool for interpreting the surface-borehole electromagnetic data in the time domain (BHTEM). This chapter begins with a contextualization of my study, followed by a review of previous work on the modeling and inversion of electromagnetic data to define specific objectives and justify the originality of my research. Finally, it describes the structure of this doctoral thesis.

#### **1.1.1 Context of the Ph.D. study**

As the large shallow (a few hundreds of meters deep) mineral deposits and energy resources have been extracted, while the needs from human activities for both mineral and energy resources keep growing, the challenge is thus to discover deeper resources hidden in the earth. Geophysical exploration is one of the most useful tools to face this challenge. The electromagnetic (EM) method can detect metallic deposits; however, the exploration depth in airborne and ground electromagnetic surveys is limited to a few hundred meters up to one thousand meters, depending upon the contrast of electrical conductivity between host rocks and the exploration target. The time domain EM signals in the late time are easily corrupted by noises due to their weak amplitude, especially for the signals recorded at the later time. To improve the detecting ability of electromagnetic (EM) methods, surface-borehole EM measurement has been developed for the exploration of deep mineral deposits, mapping structures and characterizing litho-stratigraphy. Compared with the ground and airborne EM, surface-borehole EM has greater exploration depth and higher spatial resolution, because the

receiver is located closer to deep targets, significantly improving the signal-to-noise ratio (SNR) in the late time channels for time domain surveys.

In general, there are three key elements to ensure the efficiency of applied geophysics: instrumentation, measurement protocol, and data interpretation. The development of the instrument mainly involves professional companies and university research institutes, which have developed different types of borehole measurement systems. For example, in-hole EM logging system (Sato et al., 1996), cross-borehole EM logging system (Lytle et al., 1979; Wilt et al., 1995 and 1996), borehole-surface EM system (Pardo et al., 2008), and surface-borehole EM system (hereinafter referred to BHEM in this thesis) of which is also called downhole EM system (Dyck, 1991; Tweeton et al., 1994; Geonics Limited, 2012). The current progression of instrumentation ranges from single-component to multi-components measurement, consequently it requires more efficient data interpretation tools.

In carrying out a BHEM survey, Mutton (1987) studied a massive sulfide deposit in the Agnew Nickel Belt. The same year, Richards (1987) also used the BHEM to detect massive base metal sulfides in the Broken Hill district; and Bishop et al. (1987) explored off-hole lodes cassiterite-bearing pyrrhotite at a depth of about 1 km. In 1991, Wilt et al. conducted a study of reservoir characterization using BHEM and cross-borehole EM field tests in Devine, Texas. They indicated that the sensitivity on the variation in stratigraphy is one meter for the cross-holes EM observation between the two holes separated by 100 meters; although BHEM is less sensitive to the strata variation, the EM field is strong enough to overcome the obstacle of steel well casing. Later, the U.S. Bureau of Mines, the University of Arizona, Sandia National Laboratories, and Zonge Engineering and Research Organization, Inc. (Tweeton et.

al., 1994) conducted a cooperative field test in order to compare the efficiency of six EM methods (ground: CSAMT, TEM, FDEM, and BHFDEM, borehole-borehole FDEM, BHTEM) for fracture mapping. They injected the brine solution into a known fracture zone and made 12 measurements before and after the injection. They concluded that BHEM methods detected the location of the fracture zone with high resolution. The BHEM method is, therefore, widely used in mineral exploration, especially for the exploration of large deep metal ore bodies, such as nickel/copper sulfides (King, 1996), copper/lead/zinc mine (Jackson et al., 1996), massive sulfides (Bishop, 1996), copper-gold ore deposit (Asten, 1987 and 1996) and gold mine (Stolz, 2003). Lamontagne (2007) summarized the applications of BHEM on finding off-hole conductors or defining the extent of conductors beyond boreholes for resource estimation using BHEM.

We have shown that numerical modeling can help to choose optimal survey protocols (Liu et al. 2020). With the advancement of computer technology, the development of BHEM data interpretation has been achieved a remarkable evolution from one dimension (1D) to three dimensions (3D). 1D simulation studies only the variation in conductivity along an axis, for example, the vertical variation across horizontal layers, such as BEOWULF (Raiche and Sugeng, 2008) and ORPHEO (Raiche and Bennett, 1987). 2D simulation studies the variation of conductivity in a profile, assuming that the conductivity is constant in the direction perpendicular to the profile, such as 2D TEM damped least squares based on FEM-based forward modeling (Oristaglio, 1980), MARCO and ARJUNA (Raiche and Sugeng, 2008), fast 2D inversion with Gauss-Newton (Wang, et al., 2009). Due to that the conductivities of geological bodies (metal deposits) are much higher than that of rocks in general in 3D space,

except for some minerals like graphite, therefore, the algorithms based on simple models (thin plate, sphere, etc.) were developed to simulate the electromagnetic anomaly. PLATE, SPHERE and OZPLTZ simulate BHTEM signals of simple models in a homogeneous half-space (Nabighian, 1988). MARCO and LEROI (Raiche and Sugeng, 2008) use thin plates models in a layered structure. And they fit the field data with the responses of simple models. Therefore, they all do not meet the requirement of the real geological environment. In the past decades, many software and open sources of 3D inversion have been developed, e.g., CSIRO Modules in software EMIT's Maxwell (EMIT, 2021), EH3DTD (Napier, 2007), VPem3D (Fullagar et al., 2016), ModEM3D (Egbert and Kelbert, 2012), SimPEG (Oldenburg et al., 2018) and GEM3D (Liu et al., 2019), etc. LOKI (Raiche et al., 2003), VPem3D (Fullagar, 2016), and SAMAYA (Raiche and Sugeng, 2008) can do 3D BHTEM forward modeling to satisfy the complex geological situation, however, VPem3D and SAMAYA cannot properly model the inclined conductors and complicated topography. VPem3D requires arbitrary stabilization techniques such as 'smoothing' or minimal departure from an assumed starting model, very significant computer time and memory resources for complex geological situations. In addition, it cannot properly model the conductors with dips or strikes much different from  $0^\circ$  or  $90^\circ$ , with the worst cases at  $45^\circ$  (Minami and Toh, 2012; Macnae, 2015). While Loki can build a complex geologic model as well as take topography into account, but the forward modeling takes a long time. Considering a realistic timeline within the doctoral program, we decided to improve the efficiency of the Loki forward modeling algorithm by using parallel computation in the first; and then to develop a new algorithm for the 3D inversion.

Abitibi Geophysique and the Royal Melbourne Institute of Technology have developed in recent years a new BHEM - ARMIT probe, which represents a new generation of technology that measures three components in B-field data and dB/dt data simultaneously. The improvement of the 3D forward modeling algorithm (Loki) and the development of a new 3D inversion algorithm, therefore, contribute to increasing the performance of ARMIT and the interpretation of field data. Our method is different from others by adding control techniques on the quality of the conductivity model in the inversion process.

### **1.1.2 An overview of BHEM forward modeling**

The software development for BHEM data interpretation is back to 1975. Woods (1975) built a physical scaled model facility to study plate-shaped conductors with Crone Borehole Pulse EM (PEM) (Crone, 1977 and 1979). They compiled the first comprehensive suite of BHEM responses generated by a finite thin conductive sheet. The BHEM response depends on the position of the probe and the direction of the secondary field arising from eddy currents generated in the sheet. The eddy currents in a finite thin conductive sheet can be regarded as rounded rectangular shaped current filaments, which are initiated near the edge of the sheet and moves inwards with time at a rate that has an inverse relation to the conductance of the sheet. In 1979, the Bureau of Mineral Resources (BMR) and the Commonwealth Scientific and Industrial Research Organization (CSIRO) tested the prototype SIROTEM down-hole logging probe in three drillholes (BMR 1, E36, and shaft) at Elura (Hone and Pik, 1980). Strong anomalies are recorded in the shaft and all logs recorded overburden responses. 1980, Macnae compiled the amplitude and direction of the primary field at positions beneath various rectangular transmitter loops, which is useful to assess the relative strength of secondary fields caused by induction, and in the determination of optimum loop sizes. In

addition, an analogical comparison between the diagram of the theoretical BHEM responses' curves and field data can help the estimation of unknown conductor parameters. Therefore, in order to fully study the patterns of BHEM responses, many studies of the forward modeling, based on BHEM system configuration, have been done from the physical scale modeling, simple models (sphere, plate, thin sheet, and confined conductor), one/two dimensions (1D/2D), to three dimensions (3D).

The physical scale modeling of BHEM responses carried out in the early time (Woods, 1975; Woods and Crone, 1980; and Major, 1984) is a direct and expensive way to modeling the responses due to the lack of computation facility, but it is more precise. The EM responses generated by tabular and prism conductor models with varying system parameters achieved an atlas of BHEM decay curves, which helped the field data interpretation in the early time. Later, Buselli and Lee (1996) studied the effect of overburden in free space, using the SIROTEM system configuration. They observed that the current channeling in conductive overburden produces a galvanic current that may suppress or enhance the BHEM response.

With the development of computer technology, the software for the forward modeling of simple models has become available. The typical programs include PLATE (Dyck et al., 1980; Dyck, 1981) and SPHERE (Dyck and West, 1984; Dyck, 1991), wherein a thin conductive sheet or sphere produces EM response in a resistive host. OZPLTE models the EM response of dyke-likely body in a half-space (CSIRO, 1984). These programs allow the user to analyze the distribution of the eddy currents within conductors and to study how the conductors react in an induced primary electromagnetic field and predict the locations of the simple models (McNeill et al., 1984; Levy and McNeill, 1984; Macnae and Staltari, 1987;

Thomas, 1987; Schmidt and Cull, 1995). Previous modeling results showed that the induced moment from the thin plate is perpendicular to the plate, and is independent of the primary field direction. The induced moment from the sphere is aligned with the primary field direction. Diffusion properties are quite different in plates and spheres: the current vortex collapses toward the center of the plate, and the vortex diffuses radially inward from the surface and migrates laterally through the sphere as a diffused current ring.

1D BHEM forward modeling is often used to study the effect of overburden or to detect the buried conductive/resistive layers in a layer structure environment. Kristensson (1983) has developed a general mathematical model of the electromagnetic field for any current distribution (dipole, circular and rectangular loops) in a layered earth. Raiche and Bennett (1987) developed the program ORPHEO to model the dB/dt responses of the conductive or resistive layers at the arbitrarily oriented receiver in boreholes. Augustin et al. (1989) developed a numerical modeling method of BHFDEM in a cylindrical layer model to model the EM response of casing, and show that the casing is uncoupled with geological formation at the low frequencies. Malmqvist et al. (1990) made a comparison of experimental BHEM measurements with the forward modeling response in the Finnsjo and Kankberg areas in Sweden, in which the mathematical model is based on a stratified half-space, and presented that BHEM has the capability to detect ore bodies.

In 2D BHEM forward modeling, Oristaglio and Worthington (1980) used the finite element numerical method with rectangular cells to model the responses of 2D conductivity structure. Eaton and Hohmann (1984) studied the impact of a conductive host on the BHEM response of a 2D target based on the finite difference algorithm, in which the transmitter source is a

two-infinite line parallel to the strike direction; Wang et al. (2009) developed a 2D axisymmetric formation model based on the numerical mode-matching method (NMM) in a vertical borehole.

In the past few decades, lots of 3D BHEM forward modeling algorithms are developed to fit the real geological environment. Using prism models, SanFilipo and Holmann (1985) found that the decay of prismatic conductor's response is as an inverse power law with a fall off  $t^{-\nu}$  ( $\nu$  is an exponent,  $t$  (time) is the base) for the late times in a very conductive half-space (100  $\Omega.m$ ), but it decays exponentially in the resistive half-space (Newman and Hohmann, 1988). Newton and Hohmann (1988) inserted prism models in a layered half-space and did forward modeling by using the integral equation method. EH3DTD, developed by UBC (University of British Columbia), is based on the finite volume method on staggered grid spatial discretization (Napier, 2007), in which the time step is discretized with the backward Euler method. Chung et al. (2011) used the edge-based finite element method to model the 3D controlled-source BHEM; and Li and He (2012) proposed the vertical walkaway BHEM method based on the integral equation, in which the transmitter is moved away from the borehole and the S/N can be increased by stacking the forward responses. Loki program is developed based on edge-based finite element method that precludes any conflict between continuous basis functions and discontinuous normal electric fields (Raiche and Sugeng, 2008), in which it accounts for topography and any irregular subsurface structure using hexahedral elements. VPem3D is based on linear and non-linear resistive limit forward algorithms (Fullagar, 2016), in which the sub-surface is discretized into close-packed vertical rectangular prisms, each prism is also divided into cells by a succession of geological units.

Currently, three computer programs are feasible for 3D BHTEM forward modeling, including EH3DTD, VPem3D, and Loki (Table 1.1). Several key factors play important roles in the forward modeling, such as the discretization method, required memory, and computation time. EH3DTD and VPem3D use regular rectangular cells to discretize 3D models, which have lower model resolution compare with the irregular cell design as Loki does, especially for inclined bodies as dyke, faults. VPem3D converts TEM decays to the resistive limit in order to reduce run times by a factor of 10 or more relative to conventional programs. It has several disadvantages, such as that it requires somewhat arbitrary stabilization techniques as ‘smoothing’ or minimal departure from an assumed starting model; it consumes very significantly the computer time and memory resources when more cells are required to fit the complex geological structure. Loki uses the edge-based finite element method, the electromagnetic response is computed in the frequency domain and then transformed into the time domain. It models the ground/downhole EM response (dB/dt or B) for any arbitrary 3D structure with topography due to the hexahedral elements with linear shape functions. However, one of the challenges for the finite element method used in Loki is the computer cost (memory and time). In order to make its calculation more feasible and to help us study the effect of system parameters on EM responses with a quick BHEM forward modeling, two parallelization algorithms are developed during this Ph.D. study.

### **1.1.3 An overview of BHEM inversion**

In the past few decades, significant work improving TEM data interpretation has been done from simple target-fitting, one/two-dimensional (1D/2D) inversion to three-dimensional (3D) inversion. The simple target fitting tools and methods include PLATE and SPHERE (Dyck et al., 1980; Dyck, 1981; Dyck and West, 1984), Multiloop (Lamontagne, 2007),

OPTEM (Fullagar, 1987), and the equivalent current filament (Barnett, 1984; Duncan, 1987; Duncan and Cull, 1988). The numerical methods used in 1D inversion include the adaptive nonlinear least-squares approach based on the Gauss-Newton algorithm (Deszcz-Pan et al., 1989) and joint inversion of surface and borehole TEM data based on the Gauss-Newton algorithm (Zhang and Xiao, 2001). Accordingly, Raiche and Sugeng (2008) developed BHEM interpretation programs, BOWULF for layered earth and LEROI for a thin plate in layered earth, both based on the nonlinear least-squares inversion. Some 2D inversion uses the damped least-squares method (Oristaglio et al., 1980) or fast 2D borehole EM regularization inversion (Wang et al., 2009). However, they are not feasible to map complex structure deposits or a complex geological environment in 3D. Therefore, we seek at developing a 3D inversion for the interpretation of BHEM field data.

3D inversion of electromagnetic data is an optimization problem with substantial requirements of storage and time. Due to the high cost in the computation of the Jacobian matrix and (or) Hessian matrix, low spatial resolution in TEM exploration, noise contamination in field data, etc., 3D TEM inversion is far from reaching the practical stage of field data interpretation. A very large amount of model parameters cause 3D inversion to be underdetermined and unstable, even ill-posed when the sensitivity matrix and its relevant matrix ( $\mathbf{J}$ ,  $\mathbf{J}^T\mathbf{J}$ ) are quasi-singular to singular in the ordinary least squares. Therefore, the constraint ( $\beta$ ) is introduced ( $\mathbf{J}^T\mathbf{J} + \beta\mathbf{I}$ ) to solve a stable search direction, e.g. the Marquardt-Levenberg inversion scheme (Commer, 2003).

The ordinary least squares can achieve the best-fitting data to the observed data, but the best-fitting model may be far away from the true model. Therefore, in order to find stable search

directions and reliable model estimates a-priori information and regularization are introduced. In this approach, the early iterations are dominated by the model stabilizing function, which can achieve a fast convergence to the main conductivity structures; data misfit dominates the later iterations to meet convergence of inversion as well as stability of the relevant matrix. Many algorithms have been applied to solve the 3D EM regularization inversion problem. For example, conjugate gradient (Newman and Alumbaugh, 1997; Newman and Boggs, 2004) and non-linear conjugate gradient (Newman and Alumbaugh, 2000; Commer, 2003; Kelbert et al., 2008 and 2014; Singh et al., 2017) can be restarted once the angle of two adjacent gradients is very small to avoid the low convergence in late time. The quasi-linear approximation (Zhdanov and Tartaras, 2002) and the localized quasi-linear inversion in EM (Zhdanov and Chernyavskiy, 2004; Cox and Zhdanov, 2008; Cox et al., 2010 and 2012) are based on the regularized conjugate gradient algorithms, which provide fast target imaging based on the assumption that the anomalous field within the inhomogeneous domain is linearly proportional to the background field. The Gauss-Newton method (Haber et al., 2004; Napier, 2007; Liu and Yin, 2016; Dehiya et al., 2017) only considers the first-order derivative in the Hessian matrix to reduce the storage requirements and time-consuming. The Quasi-Newton method (Avdeev, 2005; Haber 2005; Haber and Oldenburg, 2007; Napier, 2007; Egbert and Kelbert, 2012; Kelbert et al., 2014) and limited-memory Quasi-Newton method (Avdeeva and Avdeev, 2006; Avdeev and Avdeeva, 2009) only calculate the gradient of data misfit, and the correction vectors are introduced to avoid calculating the Hessian matrix, thus reducing the storage requirements. The resistive limit inversion of the steepest descent method is based on TEM moment approximation (Fullagar and Schaa, 2014; Fullagar et al., 2015; Fullagar, 2016), in which TEM quasi-magnetic problem is introduced to generate resistive limit data rapidly. Moreover, in order to overcome

the computation cost in 3D EM inversion, parallel computation has been introduced (Newman and Alumbaugh, 1997; Commer and Newman, 2004; Grayver et al., 2013; Kelbert et al., 2014; Yang et al., 2014; Cuma et al., 2016; Liu et al., 2016). All these different inversion algorithms share many common elements, e.g. data types, model parameterization, derivative calculation, etc., therefore, Egbert and Kelbert (2012) and Kelbert et al. (2014) developed a general mathematical framework for EM inverse problem to provide more efficient inversion algorithms.

There are differences between 3D inversions in the time domain and frequency domain. In the frequency-domain, to avoid the explicit computation and storage of sensitivity matrix, only the products of (Jacobian) matrices and vectors are considered in order to save the computation cost in the conjugate gradient, non-linear conjugate gradient, and Quasi-Newton methods (Rodi and Mackie, 2001; Avdeev, 2005; Miensopust et al., 2013). However, for time-domain EM, the EM responses and sensitivity matrices are calculated explicitly in the frequency domain and then transformed into the time domain. Two main challenges are the computation cost and interpretation non-uniqueness, which limit the interpretation of field data. For the computation cost, one of the methods is to introduce the adaptive cross approximation (ACA) technique to compress the Jacobian matrix at every frequency (Li, 2011), in which the Jacobian matrix is converted into the product of two rectangular matrices (for details see Bebendorf, 2000). Another way is to significantly decrease the number of unknowns by introducing the rational Krylov subspace reduction (RKSR) (Boerner et al., 2008; Druskin et al., 2009; Zaslavsky et al., 2013), in which the Maxwell electromagnetic system is projected onto the rational Krylov subspace. Regularization inversion and constrained inversion are first proposed by Tikhonov and Arsenin (1977), which may keep

the convergence of inversion to reduce the non-uniqueness of geophysical interpretation in a way.

At present times, there are five commercial software available for BHEM data interpretation (Table 1.1), which are:

➤ **1. EMIT Maxwell:** EMIT (ElectroMagnetic Imaging Technology Pty Ltd) made interfaces for 13 algorithms (Grendl, Beowulf, Aribeo, Leroi, LeroiAir, Macro, MacroAir, Loki, LokiAir, Samaya, SamAir, Arjuna, ArjunAir). All 13 algorithms were developed by the research group of Dr. Raiche at CSIRO with the support of the mining industry through AMIRA International program. However, only LOKI takes the complex geological situation into consideration; consequently, it takes a longer time to calculate the electromagnetic response.

➤ **2. MultiLoop:** a 3D forward modeling software, it can be used for computing multiple plate EM response and interpretation of plate fitting, developed by Lamontagne Geophysics Ltd (<https://www.lamontagnegeophysics.com/>). It uses four plates to fit a cubic target, or multiple plates to fit the ribbon plates regarded as conductors.

➤ **3. EMIGMA:** a PetRos Eikon's software for magnetic, gravity, IP and Resistivity, Time-domain and Frequency-domain electromagnetics, and magnetotelluric forward modeling (<http://www.petroseikon.com/>). For the 3D borehole EM forward modeling, EMIGMA provides the algorithm of the 3D integral equation in the layered host with prisms, plates, and polyhedral bodies as conductor models. In the part of TEM/FDEM interpretation,

EMIGMA provides 1D multi-component inversion allowing joint inversion of in-loop and out-of-loop data.

➤ **4. *EH3DInv***: it is developed by The University of British Columbia's Geophysical Inversion Facility in 2005 (Napier, 2007). The finite volume method on the staggered grid is used for the forward problem in the time domain. The time is discretized using the backward Euler method. It can model airborne, ground and borehole TEM data. The transmitter waveform is user-defined with no restriction on the length and shape of the waveform. The earth model is discretized using cuboidal cells (structured rectangular mesh) with constant conductivity in each cell. The Quasi-Newton method is implemented in the inversion.

➤ **5. *VPem3D***: a fast and approximate 3D modeling and inversion program for airborne, ground, and downhole time domain dB/dt or B-field data. It first converts dB/dt or B-field time decays to 1st order moments which define the resistive limit. The integral of the B-field decays over time is used to transform the multi-channel TEM inversion to a single channel magnetic inversion (Fullagar, 2016). The induced current only exists on the surface of the conductor to resist the normal component of the primary field, does not cross the interior of the conductor, also there is no interaction between conductors. The response is only related to the primary, time constant, and receiver parameters. The electromagnetic responses, therefore, become the superposition of dipole magnetic source responses. This is the reason why the calculation is fast. However, it does not consider the heterogeneity in the basement.

Table 1.1: List of available BHTEM inversion programs

<b>Software</b>	<b>Method</b>	<b>Explanation</b>	<b>Limits</b>
<b>EMIT Maxwell</b>	Current filaments FDM/FEM	1D/2D/3D forward modeling 1D/2D inversion	Layered-model inversion Plate fitting
<b>MutiLoop</b>	Current filaments	Plate forward modeling and inversion in free space	Plate used in the inversion
<b>EMIGMA</b>	Integral equation	3D forward modeling 3D inversion	Layered host with simple geometric body
<b>EH3DTDinv</b>	Finite volume method Quasi-Newton	3D forward modeling 3D inversion	Regular element
<b>VPem3D</b>	TEM moment (resistive limit) Steepest descent	3D forward modeling 3D inversion	Long vertical prisms between upper and lower surfaces Resistive limit response

Summarizing the previous studies, each method has certain advantages and disadvantages which inspired us to develop a new inversion algorithm for BHTEM data interpretation. Due to that the Gauss-Newton method has a quick slope by computing an approximate Hessian matrix, therefore, it is used for the development of my research project. First, we will review the Gauss-Newton method in detail, and then focus on the improvement of the computation

cost and the model resolution of 3D inversion. As mentioned before, Abitibi Geophysique and the Royal Melbourne Institute of Technology are developing the BHEM probe - ARMIT for deep mineral exploration. In order to assist this development, we would make a contribution to the data interpretation.

3D TEM forward modeling and inversion are fundamental for data interpretation. The former (forward modeling) starts from a physical model to calculate the geophysical response, while the inversion attempts to deduce physical models from geophysical data. Due to the large number of variables in physical models, the iteration method is often used in the inversion by minimizing the difference between observations and forward modeling responses based on the least-square principle; therefore, the forward modeling and the inversion are interrelated in geophysical data interpretation. The predicted model in terms of resistivity in the inversion is estimated by fitting the geophysical data within a tolerance. Both forward modeling and 3D inversion are time-consuming and computer-memory consuming, which causes 3D inversion to be unpractical. As the needs of data interpretation for the new measurement system (ARMIT), we aim to develop a practical data interpretation tool (3D inversion) for mapping the geology from the field data efficiently. Therefore, the main objectives of my Ph.D. study are described as follows.

## **1.2 Research objectives**

- Adapt the LOKI to the forward modeling of BHTEM response and using parallel computation to improve its efficiency.
- Develop an algorithm of 3D inversion of BHTEM to interpret the field data for producing geologically acceptable models.

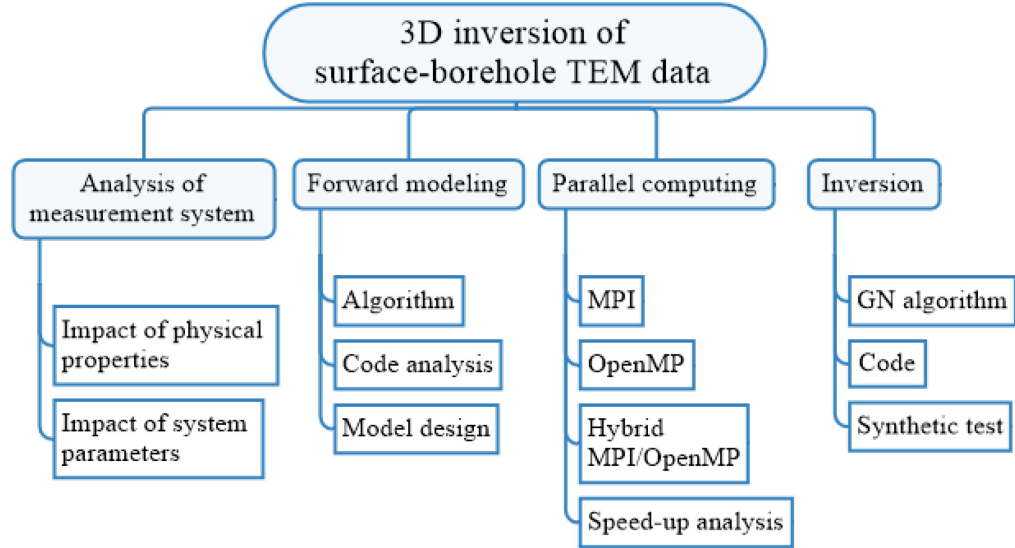


Figure 1.1: Workflow of the project

Figure 1.1 shows the workflow that outlines the main components of my developments. The whole project is broken down into four sub-projects, including the analysis of the measurement system, 3D forward modeling, parallel computation, and 3D inversion.

### 1.3 Methodology and Originality

Several new developments have been achieved that represent the originality of my Ph.D. research as described below.

- Improving a 3D BHTEM forward modeling using parallel computing with multiple meshes.
- Developing a novel 3D BHTEM inversion algorithm based on the Gauss-Newton method.
- Proposing an optimal measurement strategy for electromagnetic survey design.

- Building a new interface for 3D geological model construction to facilitate the 3D BHTEM forward modeling and inversion calculations.

#### **1.4 Outline of the thesis**

The first chapter is an introduction to forward modeling and BHTEM data inversion, in order to get an overview of what has been done in the past and what is needed for new development.

The objectives of my research were defined based on those literature reviews.

In chapter two, an interface for building 3D geological models is developed to help the pre-/post-processing of 3D forward modeling and 3D visualization of the forward modeling and inversion results.

The third chapter describes in detail the parallel TEM forward modeling method and the comparison of the results with the conventional method. It analyzes the strategy used for saving memory and computation time by introducing multiple meshes into different frequencies. This chapter is a published article.

Liu, C., Cheng, L. and Abbassi, B., 2020, 3D parallel surface-borehole TEM forward modeling with multiple meshes: *Journal of Applied Geophysics*, 172, 103916.

In chapter four, forward modeling helped for optimal BHTEM survey design. From basic theory, we described the principle of the electromagnetic field and the mathematical methods used in EM forward modeling of the simple wire loop model. A large number of TEM forward modeling calculations prove that the response (secondary field) is affected by the measurement time in surface-borehole, ground, and airborne TEM exploration. The new

relationship developed within this Ph.D. program allows us to evaluate optimal pulse widths for different off-times and to help BHTEM survey design. This chapter is a published article. Liu, C., Cheng, L., Dai, X., and Diallo, M.C., 2020. Improvement of the Efficiency of Time-Domain Electromagnetic Measurement. *Pure and Applied Geophysics*, p.1-12.

The fifth chapter introduced an inversion algorithm. The complexity in the inversion is reduced to deliver a more plausible geological model by integrating the isosurface, neighborhood anomalies search, 3D trace envelope and false targets elimination into the inversion process. The inversion code has been tested using synthetic models. It is submitted to a journal for publication.

Liu, Chong; Cheng, LiZhen; Chouteau, Michel; Erchiqui, Fouad. 3D Gauss-Newton inversion of surface-borehole TEM data.

Finally, an overall conclusion summarizes the main achievements within the framework of this doctoral study, and we recommend some avenues of research on future work to improve the BHTEM inversion.

## CHAPTER 2

### DESIGN OF A 3D MODEL CONSTRUCTOR

#### 2.1 Development of an interface for model design

A large number of geological models and various configurations of measurement systems will be involved in the tests of parallel BHTEM forward and inverse calculations, as well as in studies for the optimal choice of measurement system parameters (Figure 2.1). Therefore, an easy and fast data processing tool is essential for helping the entire development of the research project. This tool will enable geologists to construct the guessed geological models according to drilling logs or other geological interpretations inferred from geologists' experiences, and then to quickly establish an initial physical model for geophysical calculations (forward modeling and inversion). Maximizing the integration of known geological information in the interpretation of geophysical data allows a better understanding of the corresponding act of geological structure in the physical field in the exploration area.

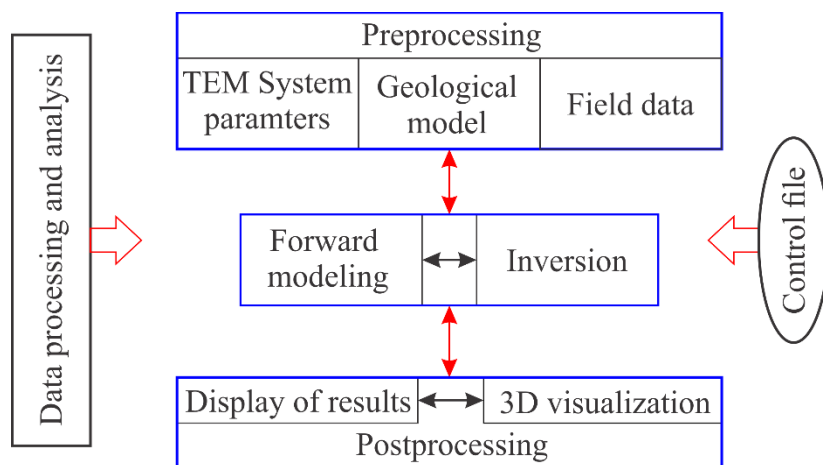


Figure 2.1: The general flow chart of data and the main modules for TEM exploration

Table 2.1: List of the modules and control files in the 3D model builder

<b>Modules</b>	<b>Input or output files</b>	<b>File names</b>
Tx&Rx configuration	System parameter files (out)	spf.txt (user-defined)
	Borehole information (out)	Bh.txt (user-defined)
Model maker and discretization	Resistivity model file (out)	rmf.cfl (user-defined)
Field data processing	Observed data (in and out)	Text file (user-defined)
3D parallel forward modeling and inversion	Control file (in)	Loki.cfl (fixed name defined by Loki)
	data (out)	Loki.out, Loki.mfl (fixed name defined by Loki)
Display of responses	Forward modeling data (in)	Loki.mfl (fixed name in Loki)
	field data (in)	tem.mfl (user-defined for field data)
3D visualization	Resistivity file from inversion (in)	rffi.res (user-defined)

The interface developed within the framework of this Ph.D. study is a window environment, which consists of six individual and interactive modules for three steps of processes (Table 2.1). The first step is the process of data preparation, including the input of measurement system parameters, Tx&Rx configuration, construction of the geological (initial) model, the discretization of the 3D initial model, and the field data processing. The second step is the process of calculations, including 3D BHEM forward modeling and inversion (data interpretation). The third step is the display of results, including profile, decay curves and 3D visualization of inversion result. The analysis on the integration of the geophysical modeling and the inversion results constrained with geological data will be performed in the data

postprocessing stage. The detail of those three steps of processing is described in the following sections.

## **2.2 Measurement system parameters**

The measurement system consists of the transmitter (Tx) and the receiver (Rx), therefore, the field configuration in BHTEM exploration involves mainly the location and the size of the Tx loop on the ground, the locations of Rx in boreholes (Figure 2.2) and the information about the borehole (Figure 2.3). With regard to parameters of the measuring system, they are the waveform of transmitted current (Figure 2.4-2.6) and the time window that defines the duration of power-on / power-off of the measurement. A detailed description about the input of the above information is addressed as follows.

The Tx can be an arbitrary polygon loop. Setting the locations (East, North, Depth) of the vertices forms the Tx loop, such as the red rectangular in Figure 2.2. The Tx loop is on the surface for BHTEM, therefore, depth = 0. The order for setting the vertices determines the direction of the primary field. If the loop vertices are set in the clockwise direction, the primary field is downward; if the loop vertices are set in the anti-clockwise direction, the primary field is upward. It mimics the direction of the circulating current.

The receivers (Rx) are set along the boreholes. The borehole can be vertical, but often it is inclined in the field measurement (colored dot line in Figure 2.2). Each borehole (or survey line along the borehole) has its collar, dip angle, azimuth. The first Rx location represents the locations of the borehole on the surface. The borehole azimuth ( $\gamma$ ) to the north is zero, and

positive clockwise. The inclination ( $\alpha$ ) is zero (degree) for the horizontal borehole and 90 degrees for the vertical borehole (Figure 2.3).

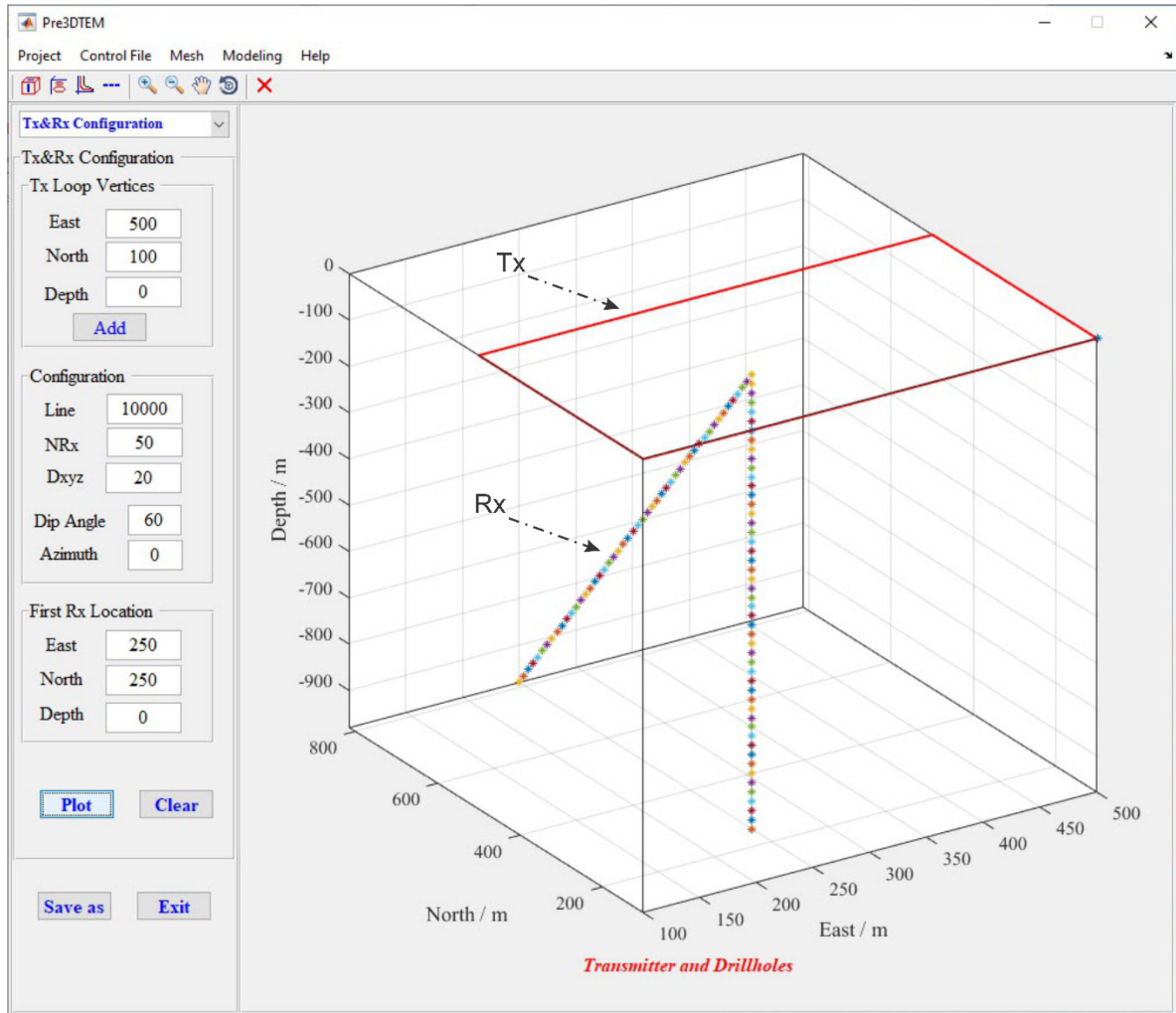


Figure 2.2: Setting Tx on the surface and Rx in the boreholes. The relative coordinate system is used for all the figures in this thesis. One also can use the geographic coordinate.

In a BHEM survey, the primary electromagnetic field is generated during power on-time, and the secondary electromagnetic field is recorded during power off-time. As illustrated in Figure 2.4 – Figure 2.6, there are three transmitter waveforms in this tool, including

trapezoidal waveform, half-sine, and triangular waveform. One can get various transmitter waveforms by adjusting the base frequency and duty cycle so that they can suit the requirements of different exploration targets.

Unlike the grounded/airborne TEM in the half-space model, BHTEM has complex coupling between Tx, Rx, and conductors in the full 3D space. Therefore, the distribution of the primary field related to a conductor, the location and the shape of the conductor and the relative position of Rx determines the quality of observed data (as shown in Figure 2.7). For unknown exploration targets, the optimal design of field measurement with multiple Tx loops and boreholes can help to obtain more geological information.

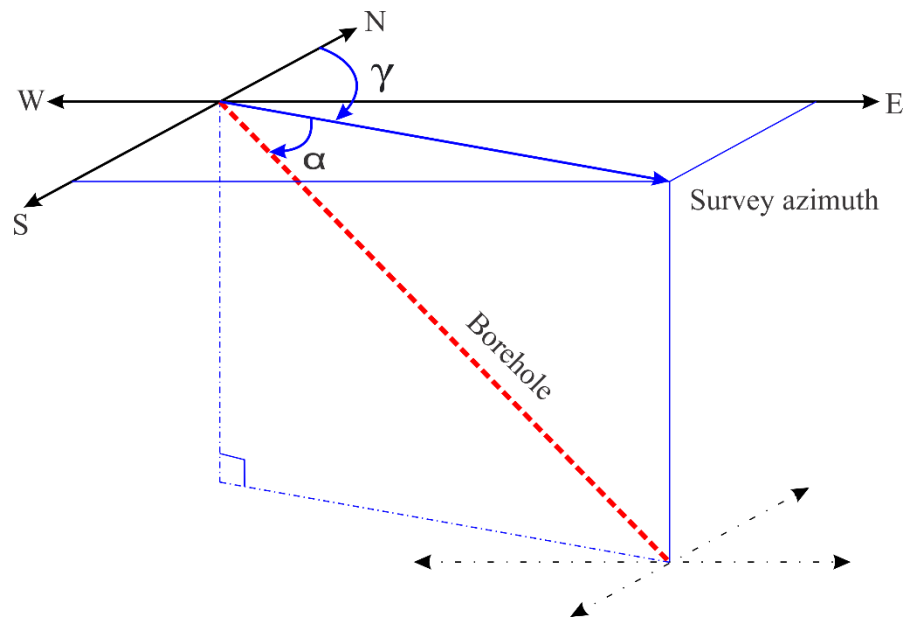


Figure 2.3: The definition of borehole parameters,  $\alpha$  is the dip angle between the borehole and horizontal plane,  $\gamma$  is the azimuth angle between the north and survey azimuth.

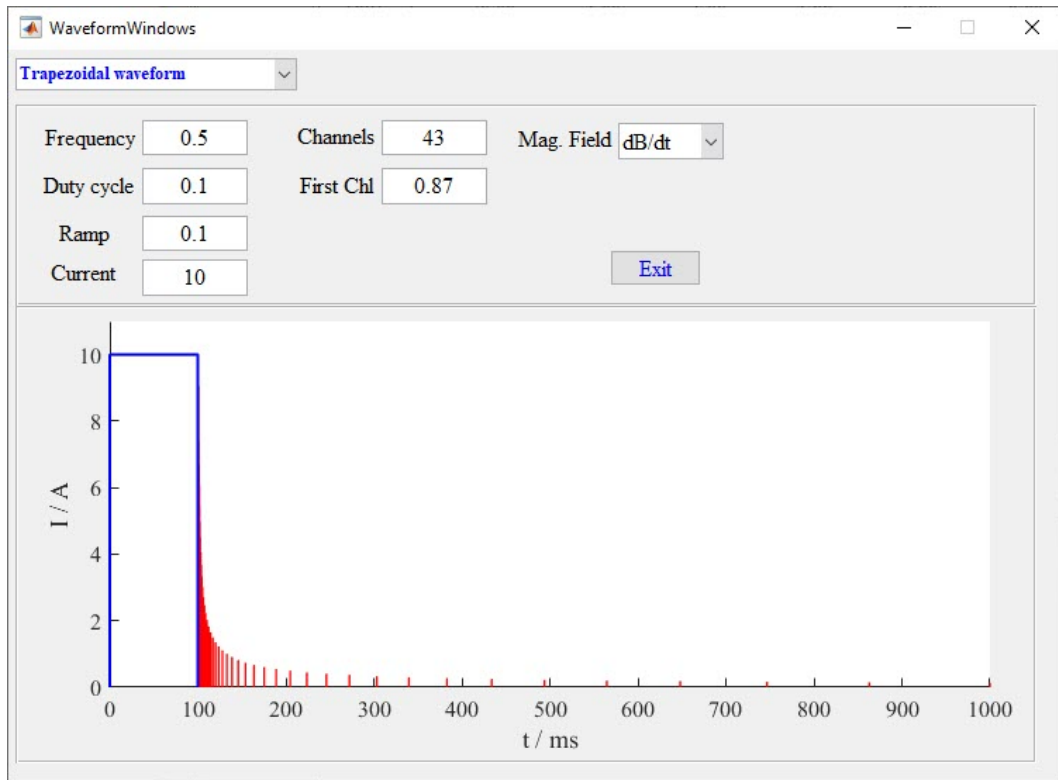


Figure 2.4: Trapezoidal waveform

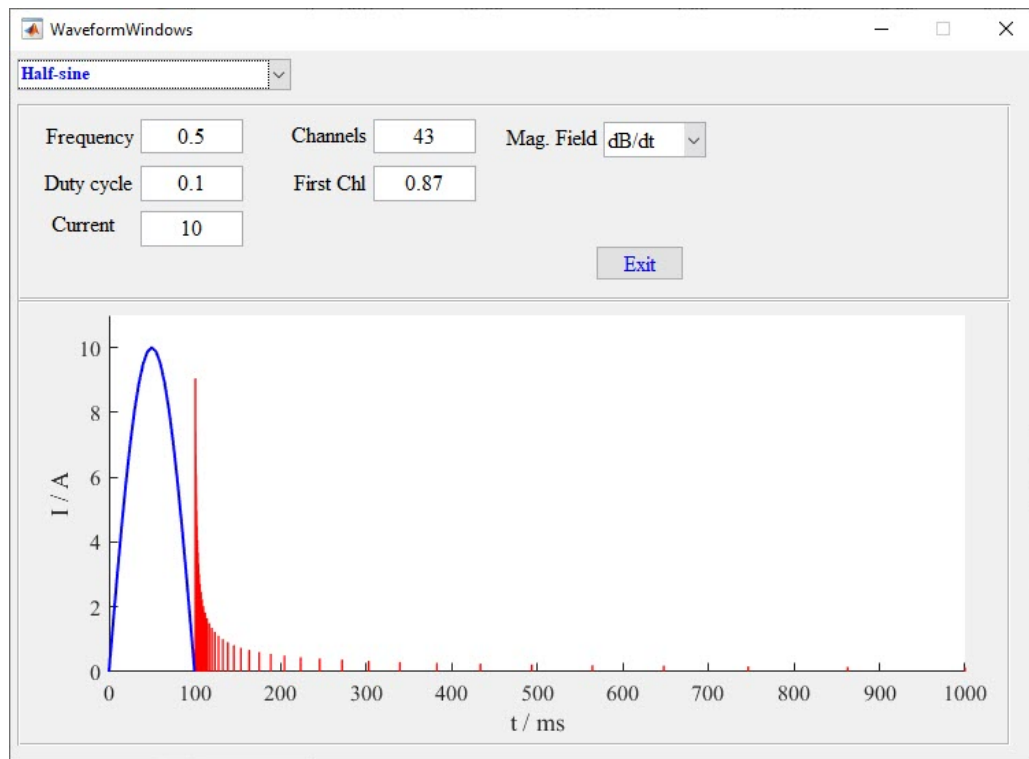


Figure 2.5: Half-sine waveform

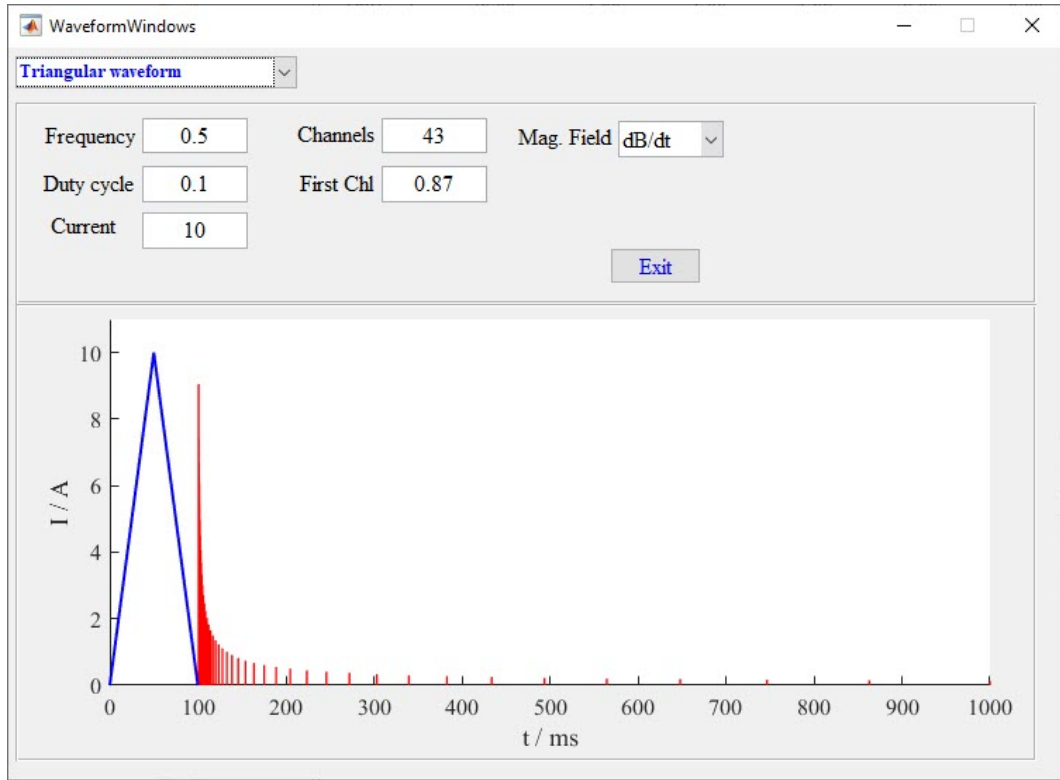


Figure 2.6: Triangular waveform

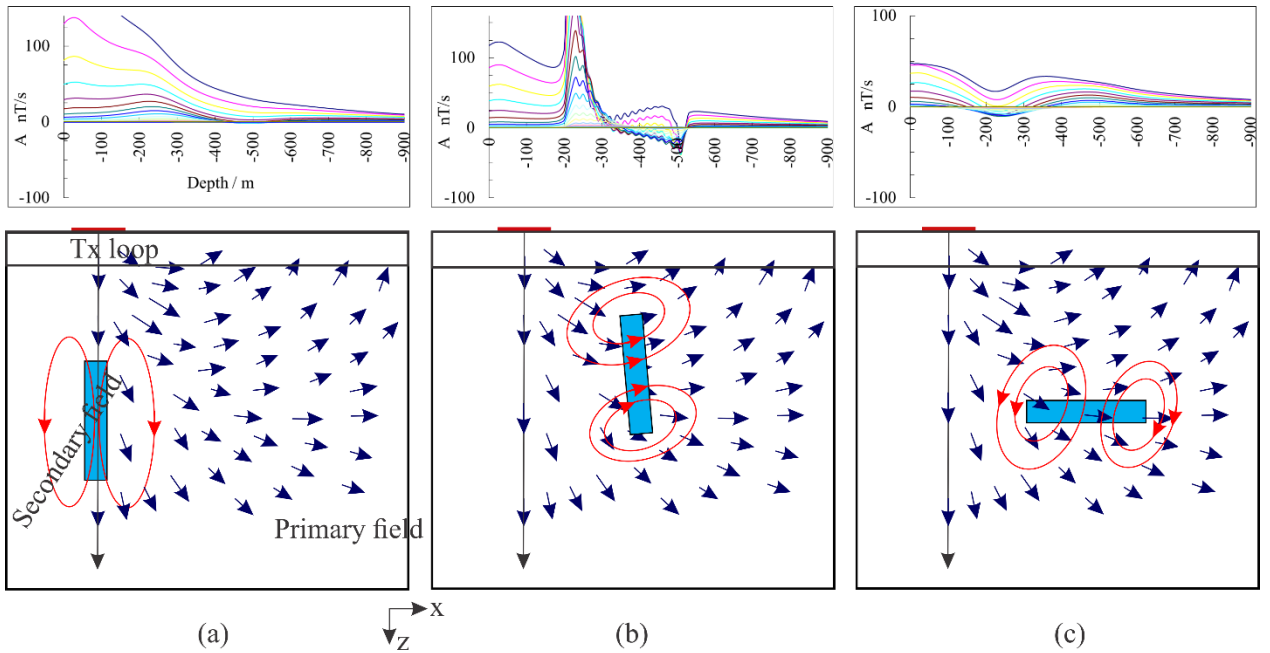


Figure 2.7: The distribution of primary field and the coupling between Tx, Rx, and conductor

## **2.3 Design of 3D model and discretization**

### **2.3.1 3D model design**

In the data preprocessing, the design of the 3D model and the discretization are fundamental for the forward modeling and the inversion, as well as for testing geological hypotheses. Therefore, we aim to create a tool for building an initial geological model easily and quickly. Figure 2.8 shows an example of its application.

The first is to create the geological slices along one direction (north, east, or depth) based on the drilling information or projected from geological maps, such as the slices s1 to s7 in Figure 2.8a. The slices can be equally spaced or not, but they should have the same dimensions. The different geological formations can be distinguished using different colors. More slices will allow building a more complex geological environment, and after the model discretization, it allows modeling TEM responses of complex models.

After importing the slices into the tool, the empty area between the slices will be interpolated based on the two adjacent slices. The recoloring of the geological units is based on the search order from top to bottom. One can build a 3D geological model with 7 slices as shown in Figure 2.8b, it took a few seconds on the general desktop.

After building up the initial geological model, the single physical parameter - resistivity is involved in the BHTM forward modeling or determined by the inversion. For the forward modeling, one can set the resistivity for each geological unit in the column RES of the Table 1 (lithologies for geo-model) in Figure 2.9 and keep other parameters as default.

### **2.3.2 Discretization**

The general meshing methods are the structured mesh and the unstructured mesh (Key and Weiss, 2006; Haber and Schwarzbach, 2014). The former often uses the rectangular prism or hexahedral cell, the latter uses hexahedral cell, tetrahedral cell, or the mixture of them. Currently, the rectangular prism (structured mesh) is used to discretize the model in the present tool. The hexahedral cell will be used to fit the complicated boundary of geological structures in future development.

As shown in Figure 2.9, the automatic discretization is done by setting the cell size in the east, north, and depth direction. On the model boundary, the cell size is generally 50m – 100m that depends on the model dimensions. In the Z direction, the cell size increases by a factor depending on the depth. To avoid the sharp cells that may cause the distortion of the TEM field, the aspect ratio of the cell must be restricted (less than 5:1).

For the automatic discretization of the model, the conductor much smaller than the size of the cell is ignored, and it is integrated into the background. Therefore, new resistivity values are reassigned in the column RES on the Table 2 (lithologies after meshing) in Figure 2.9.

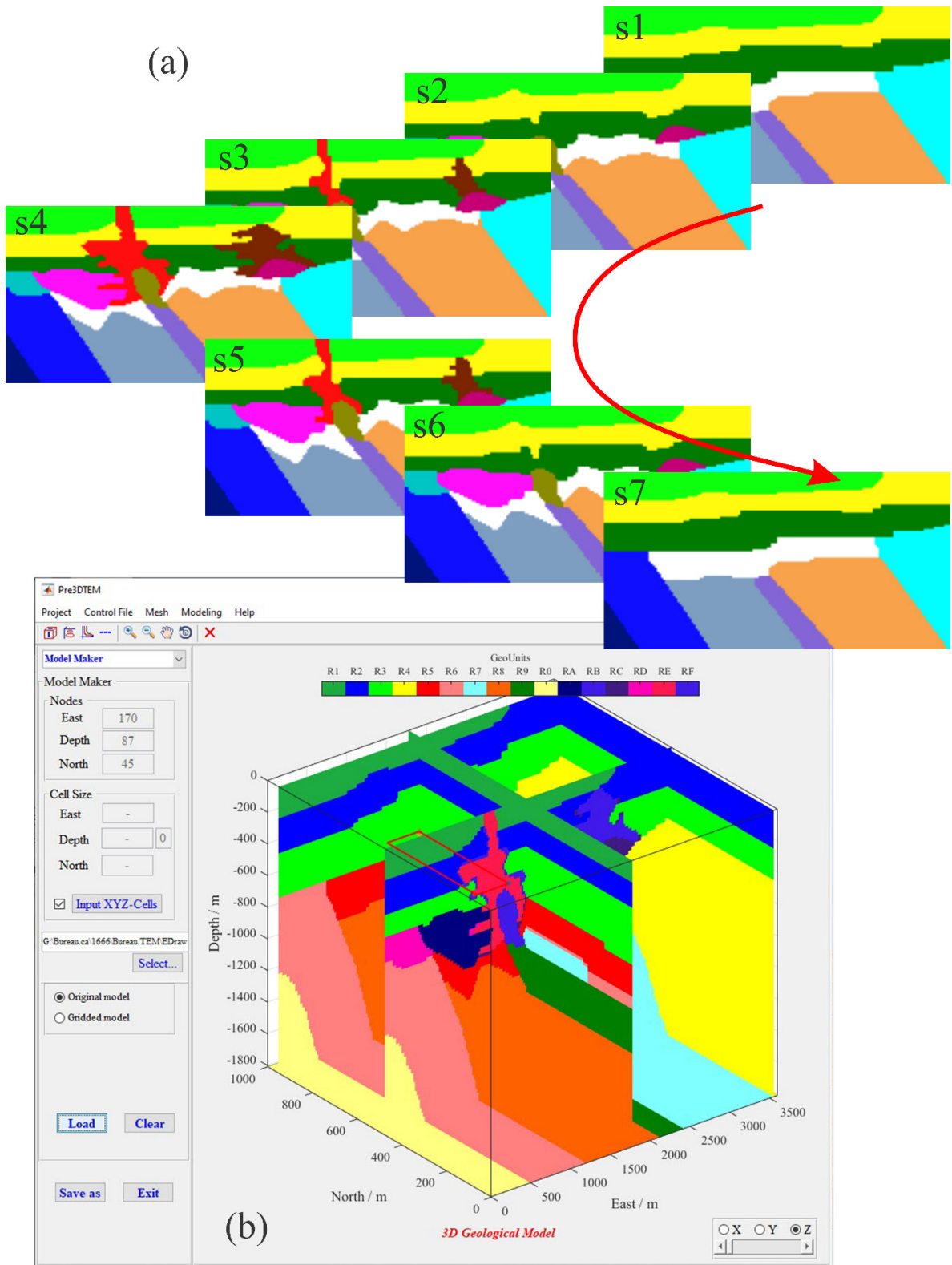


Figure 2.8: The geological model

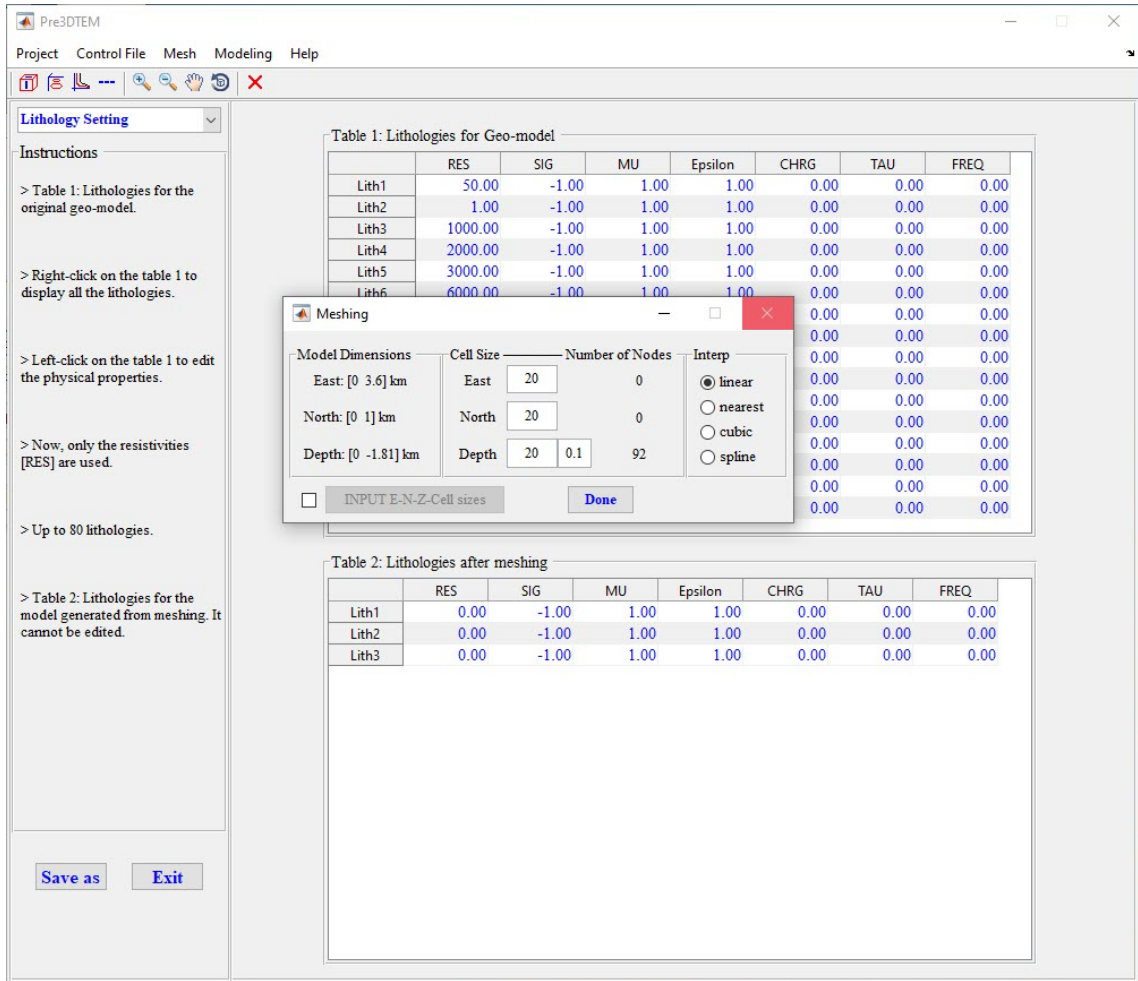


Figure 2.9: The Table 1 shows initial resistivity values in the geological model (Lithologies for Geo-model). The Table 2 shows the resistivity values after re-meshing the model (Lithologies after meshing).

## 2.4 Data for BHTEM forward modeling and inversion

All the data, including system parameters and mesh data, are stored in the control file - Loki.cfl (defined by the code of Loki) in the forward modeling. All simulation and field data are stored in the control file - tem.mfl; and for the inversion, the field data are converted and stored in the file - Loki.inv. Figure 2.10 illustrates the forward modeling window. Currently,

the inversion is done outside of the tool and will be integrated into this tool. In addition, we should clarify two implicit data as below.

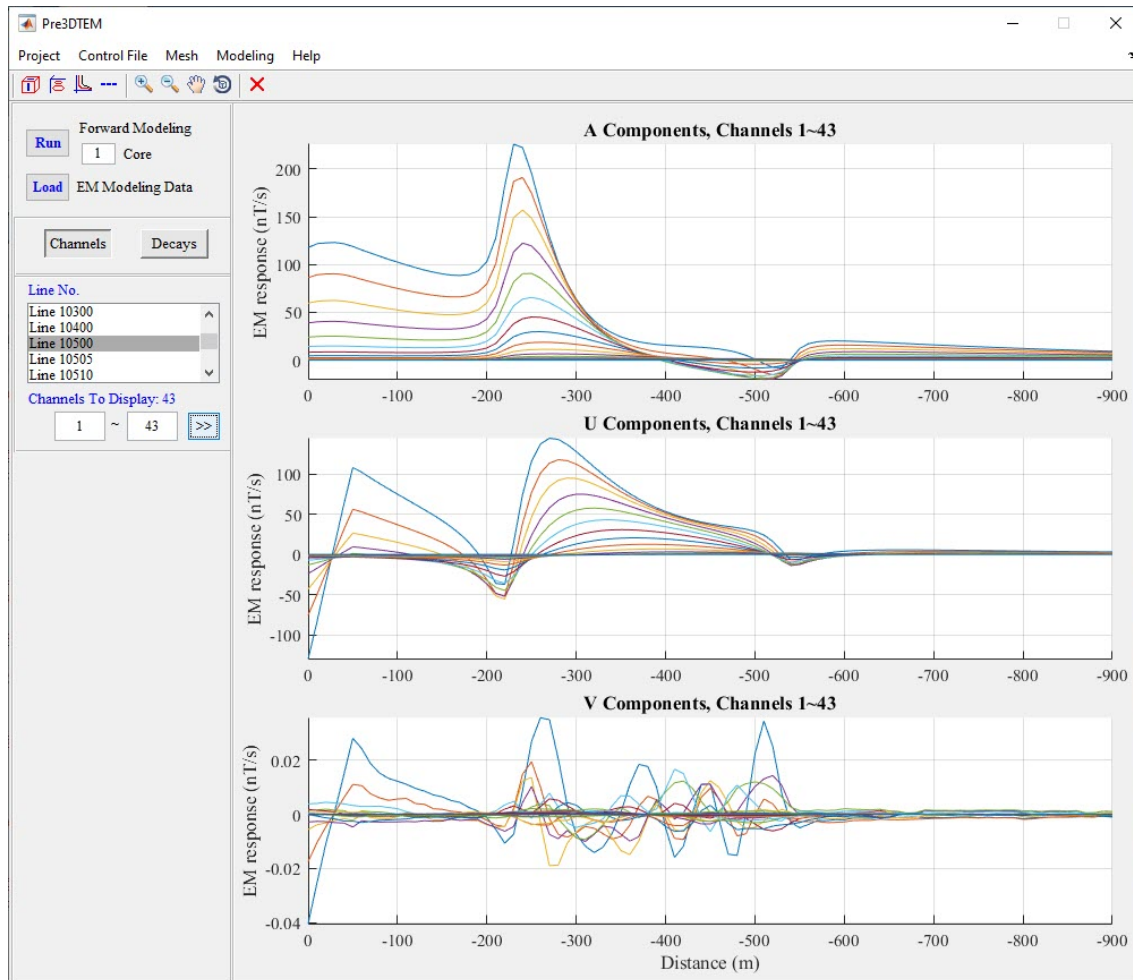


Figure 2.10: BHTEM Forward modeling and three-component responses (A, U, V)

### **Frequency range**

Since the calculations of BHTEM response are performed in the frequency domain, and then through the transformation to get the response in the time domain, we need to have enough frequencies to keep the accuracy of simulation results, but also the computation time. Six points per decade are chosen in our study for the frequency discretization to maintain the

accuracy of the result. In the forward modeling, the frequency range depends on the resistivity of the geological units; the low resistivity requires a wider frequency range than the high resistivity. In general, the range of the frequency for the induced electromagnetic method is within 1MHz, which is used in our study.

**BHTEM components**

Besides the above settings, the definition of the three components in BHTEM forward modeling is essential. Figure 2.11 shows the directions of three BHTEM components. A (Z) is axial to the borehole and is positive upwards. U (X) is in the vertical plane containing A (the tangent) and orthogonal to A. V (Y) is orthogonal to the UA (XZ) plane and forms a right-hand coordinates system such that  $U \times V = A$  (Bishop, 1996; Cull, 1996; Hughes, 1996).

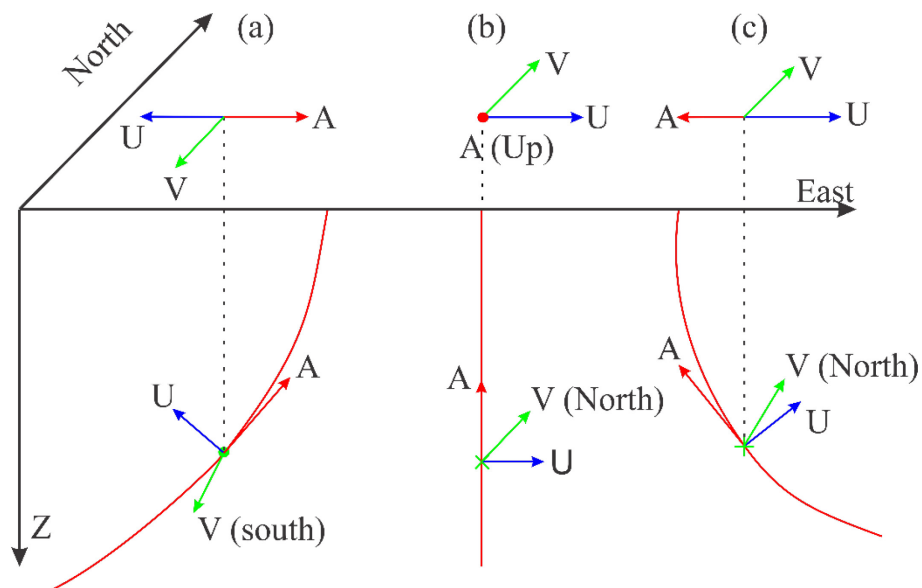


Figure 2.11: The definition of three components of the BHTEM field, in which the azimuth of the drillhole is regarded as a reference. A: parallel to drillhole trajectory. U: in the vertical plane containing A. V: perpendicular to A and U in a right-hand coordinate system (Bishop, 1996; Hughes, 1996)

## 2.5 Visualization

Two types of visualization are possible, which are profile and 3D model. The profile is useful for reviewing field survey results and for the analysis of decay curves. As shown in Figure 2.11, the three-component data can be displayed along the survey line (borehole). Figure 2.12 displays the decay in one profile and one can compare the decays at different survey stations.

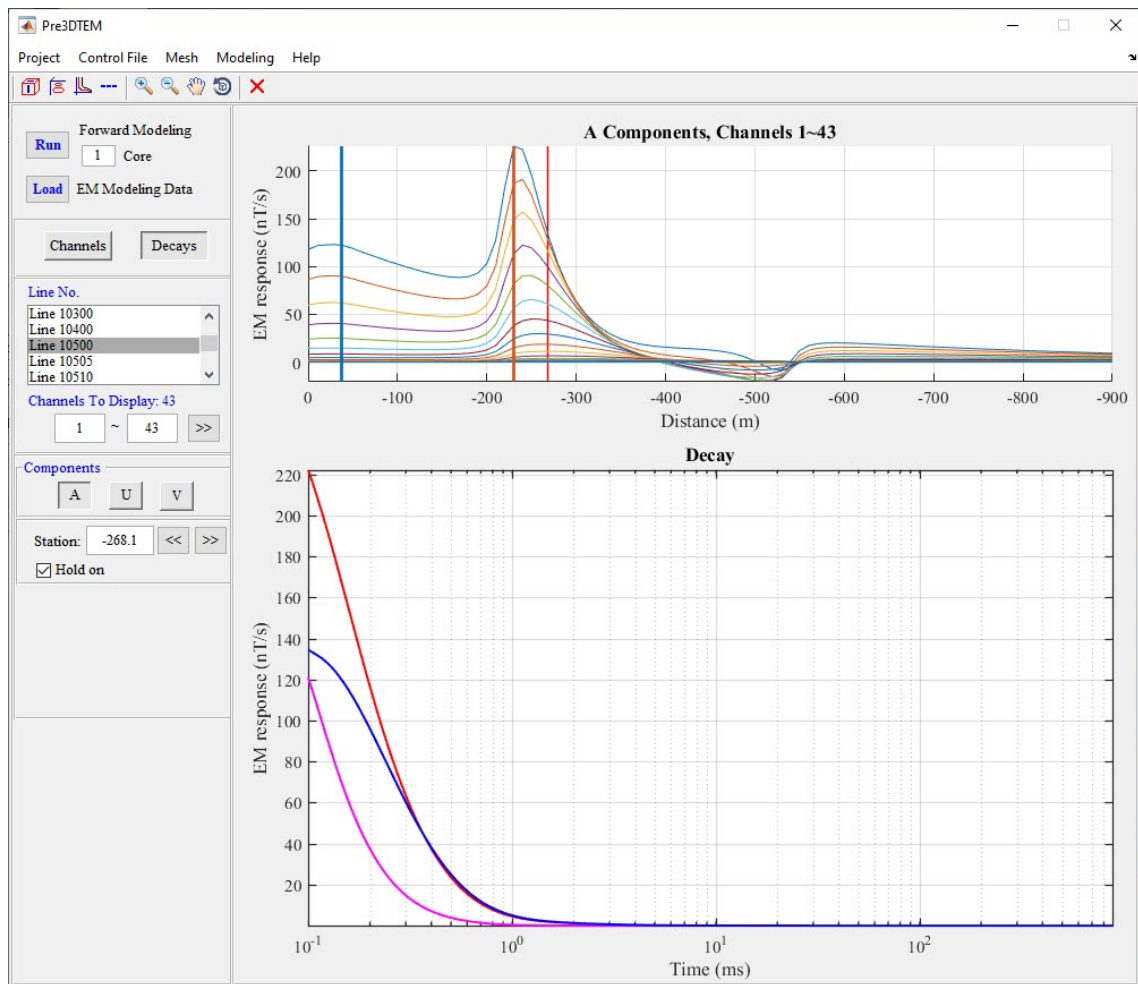


Figure 2.12: BHTEM response along a borehole (upper) and the decay curves at different survey stations (bottom)

Regarding 3D visualization, before the forward modeling it visualizes the initial model and the configuration of the measurement system. After the inversion, it visualizes the distribution of the resistivity (Figure 2.13). We can delineate the anomalous zone by using isosurface, trace envelope based on the information in Figure 2.13 and Figure 2.14 and run again the inversion using the updated initial model.

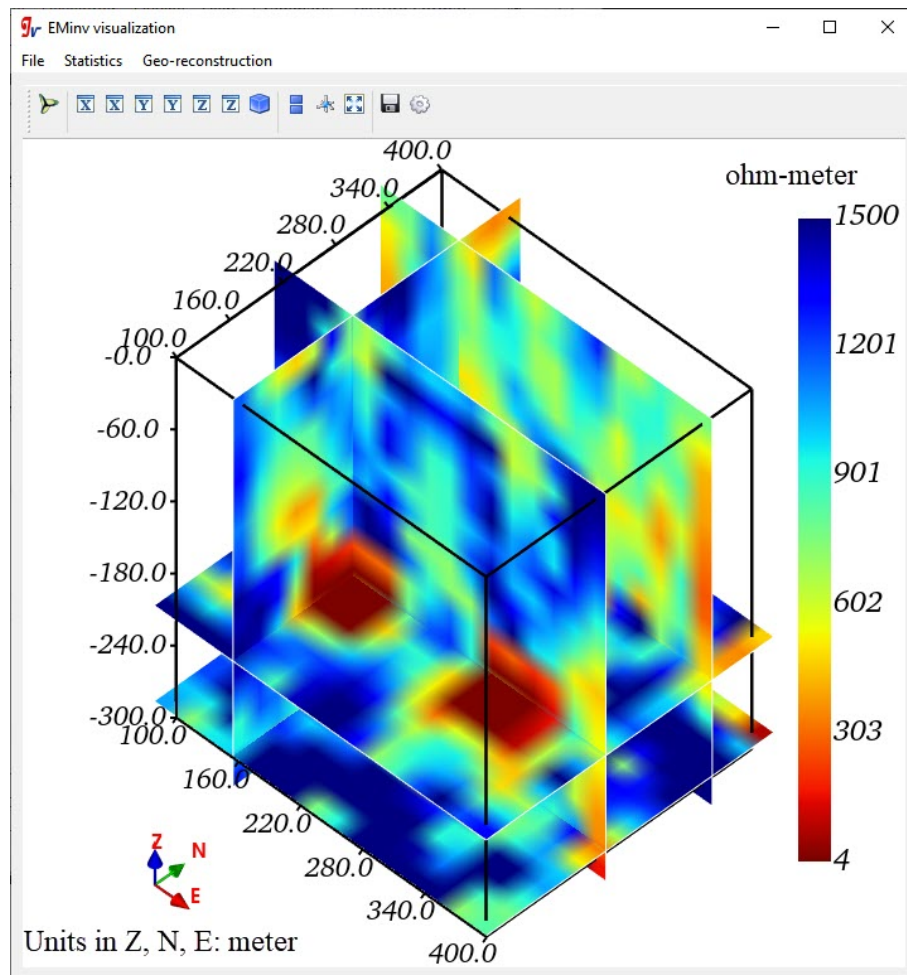


Figure 2.13: 3D visualization of inversion result

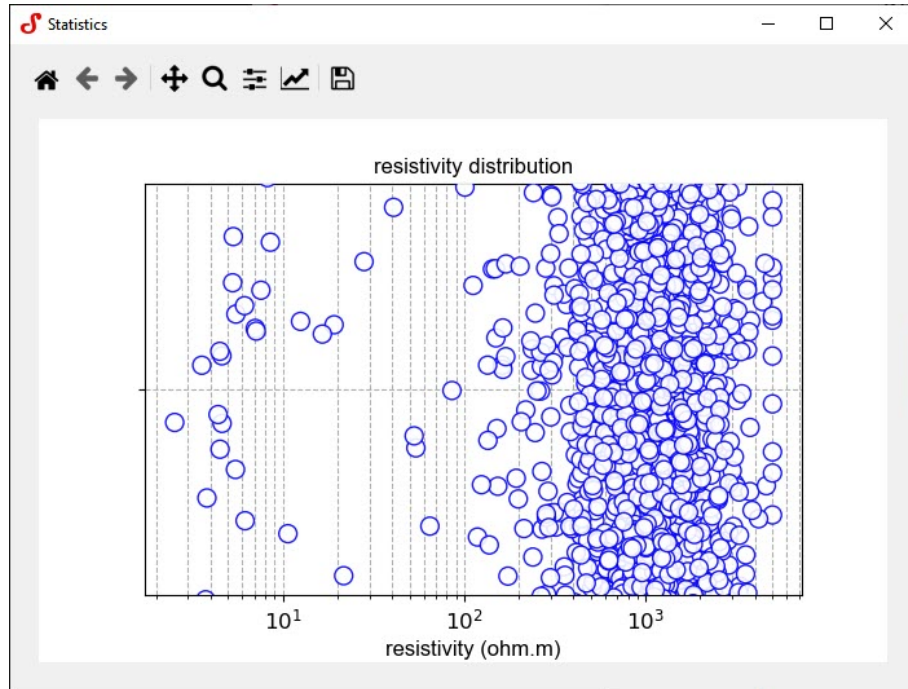


Figure 2.14: The scatterplot to show the distribution of resistivity from the inversion result, the vertical axis is used to separate the same values.

## 2.6 Conclusions

Both forward modeling and inversion share many data types, such as survey configuration, geological model, the display of data (3D visualization). Therefore, a 3D model constructor is developed to connect different parts and to help the pre-/post-processing in 3D forward modeling and inversion of surface-borehole TEM data, as well as the 3D visualization of the forward modeling and inversion results.

# CHAPTER 3

## 3D PARALLEL SURFACE-BOREHOLE TEM FORWARD MODELING WITH MULTIPLE MESHES

### 3.1 Introduction

In a TEM survey, a transmitter loop emits a primary EM field using a specific source waveform. The propagating primary field interacts with rocks and generates the secondary EM field around underground conductors. Three-dimensional (3D) numerical modeling of TEM data aims to simulate this induction phenomenon and reconstruct a physical property model in the form of 3D conductivity distributions. EM measurements at ground surface integrated with borehole data sets allow acquiring information about the 3D distribution of electrical conductivity of subsurface. The key question is how to extract useful geological information from those EM observations. This is a form of the inverse problem, in which one aims to recover subsurface physical properties (conductivities) from surface EM measurements. Conventionally, the data inversion is based on iterative forward modeling through least square methods to reduce the misfit between measured and simulated EM data. Therefore, a fast and accurate 3D forward modeling algorithm is needed to develop an efficient 3D inversion code.

For 3D forward modeling, finite element methods (FEM) can take into account the complex geological environment by discretizing the earth model into polyhedrons. Common node-based finite element methods (Jin 2002; Um, Harris and Alumbaugh, 2012) and edge-based finite element method (Nédélec, 1980; Graglia et al., 1997; Midtgård, 1997; Li, 2002; Ilic and Notaros, 2003; Sugeng and Raiche, 2004; Sun and Nie, 2008; Da Silva et al., 2012) are

popular numerical methods in EM forward modeling because of their more effective model discretization for complicated topography and irregular body shapes and their high accuracy. However, the more complex the underground environment, the more time consuming the FEM calculations are. This problem is due to several factors, including a large number of cells in FEM, multiple frequencies used in the forward modeling, forming the stiffness matrix for solving the secondary field, solving large matrix equations and computing secondary field with a large number of survey stations.

Computational cost (time and memory) can be efficiently reduced by reducing the number of mesh elements, but this strategy leads to lower resolutions in EM data simulation and consequently lower quality physical property models during the inverse modeling. Parallel computation is an alternative solution and has been successfully applied in 3D marine controlled-source EM data simulation (Puzyrev, et al., 2013; Cai, et al., 2015; Reyes, et al., 2015), 2D/3D magnetotelluric (MT) forward modeling and inversion (Tan, et al., 2006; Wang, et al., 2015), 3D long-offset transient electromagnetic field simulation (Commer and Newman, 2004), and 3D airborne TEM data inversion (Haber and Schwarzbach, 2014).

Two available platforms for parallel programming are the graphics processing unit (GPU) and the central processing unit (CPU) (Grama, et al., 2003; Wilkinson and Allen, 2004). GPU has more than hundreds of cores, which can be able to manage multiple parallel tasks simultaneously such as image and signal processing. CPU has limited cores and processes the tasks in series. Even though the individual core of CPU has high performance in the calculation, it is slower than GPU, due to its inherent serial processing with cache memory.

Due to the limit of the computer facility, the present study is based on a CPU platform with eight physical processors.

Our study is in surface-borehole TEM forward modeling. The 3D forward modeling code (Loki) used in this study is an edge-based finite element algorithm developed by a research group led by Art Raiche at CSIRO Australia (Raiche, et al., 2003). Although it can simulate the TEM responses from arbitrary geological models, it is not widely used due to its time-consuming forward calculations. The present work aims to improve the Loki code through CPU parallelization to reduce the computational cost while preserving the resolution of simulated EM data.

In this paper, we first briefly review the basic theory of the TEM measurements, together with FEM applied to forward modeling, and then we outline the parallelized TEM forward modeling principles. Two parallel computation algorithms are dedicated to speed up the 3D surface-borehole TEM forward modeling in this study. We also introduce a multiple meshes technique for the TEM forward modeling to further reduce the computational cost.

### **3.2 Edge-based finite element in TEM forward modeling**

The surface-borehole TEM method uses an EM transmitter source on the surface and a receiver down in boreholes (Figure 3.1). The transmitter source could be of closed-loop source or finite long wire source with impulse-voltage or AC power supply. First, let us review Maxwell's equations in the frequency domain and the edge-based finite element method used for TEM forward modeling (Nabighian, 1988; Jin, 2002).

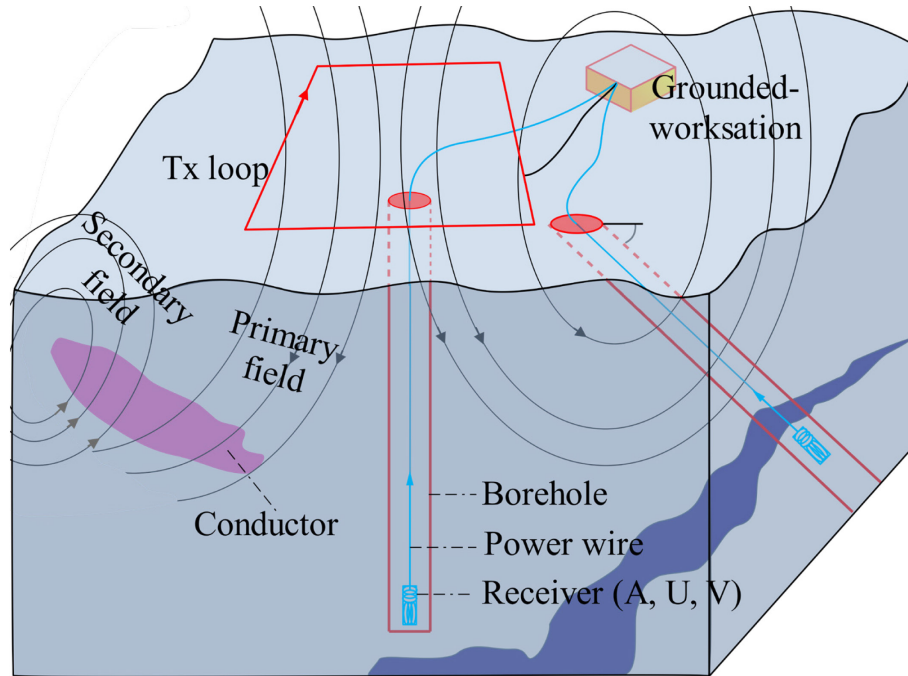


Figure 3.1: Sketch of the configuration of surface-borehole TEM, and the illustration of the primary field generated by the loop source and the secondary magnetic field induced in the conductor.

$$\nabla \times \mathbf{E} = -i\omega\mu_0\mathbf{H} \quad (3.1a)$$

$$\nabla \times \mathbf{H} = \sigma\mathbf{E} + \mathbf{J}_e \quad (3.1b)$$

$$\mu_0\nabla \cdot \mathbf{H} = 0 \quad (3.1c)$$

$$\nabla \cdot \mathbf{E} = \frac{\rho}{\varepsilon} \quad (3.1d)$$

Where  $i = \sqrt{-1}$ ,  $\mathbf{E}$ ,  $\mathbf{H}$ , and  $\mathbf{J}_e$  denote the electric field, the magnetic field, and the current density, respectively.  $\mu_0$  denotes the magnetic permeability,  $\sigma$  is the electric conductivity,  $\rho$  is the density of the charge in the medium, and  $\varepsilon$  represents the dielectric permittivity.

Using the Schelkunoff potentials, the magnetic vector potential  $\mathbf{A}$  is decomposed into a primary potential (background)  $\mathbf{A}^P$  and a secondary potential  $\mathbf{A}^S$  (Stalnaker et al., 2006). The electric source generates  $\mathbf{A}^P$  in the half-space and  $\sigma_p$  is background conductivity. The secondary potential  $\mathbf{A}^S$  is only caused by the area where the anomalous conductivity  $\sigma_S$  is non-zero.

$$\mathbf{A} \equiv \mathbf{A}^P + \mathbf{A}^S \quad (3.2)$$

Using the vector theory and Lorentz gauge, the relation between the primary and the secondary vector potential in the frequency domain is defined by the Helmholtz equation as below.

$$\nabla^2 \mathbf{A}^S - i\omega\mu_0\sigma\mathbf{A}^S = i\omega\mu_0\sigma_S\mathbf{A}^P \quad (3.3)$$

Where  $\sigma_S = \sigma - \sigma_p$  is the difference between the conductivity distribution ( $\sigma$ ) and the background distribution ( $\sigma_p$ ). Equation 3.2 is the governing equation for providing EM field modeling. The source is introduced in terms of primary EM potential that is known to the problem with background conductivity ( $\sigma_p$ ).

According to the vector theory, the divergence of the curl of one vector equals to zero, we get the magnetic field,

$$\mathbf{H} = \nabla \times \mathbf{A} \quad (3.4)$$

For the simulation of secondary potential  $\mathbf{A}^S$  in this algorithm, the edge-based finite element method is used to discretize Equation 3.3, the final equations system is expressed as,

$$\mathbf{KA}^S = \mathbf{b} \quad (3.5)$$

Where  $\mathbf{K}$  is a  $N_e \times N_e$  matrix,  $N_e$  denotes the number of cells. The matrix ( $\mathbf{K}$ ) is symmetric and complex in the frequency domain and can be solved using the conjugate gradient (CG) solver with pre-conditioner and scaling. Then substituting the result (the secondary magnetic potential) into Equation 3.4, one can get the magnetic and electric fields in the frequency domain. The approximation of the numerical differentiation in Equation 3.4 causes an inevitable loss of accuracy. To address this issue, Raiche et al. (2003) used Green's function operators and volume integral to reduce the error in 3D numerical modeling. Using time-frequency transformation yields the TEM responses, including Gaver-Stehefekt inverse Laplace transformation (Knight and Raich, 1982), Guptasarma transformation (Guptasarma, 1982), and sine and cosine transformation (Newman, et al., 1986). As the EM forward modeling is deployed in the frequency domain, the result is then converted from the frequency domain to the time domain.

### **3.3 Parallelization**

#### **3.3.1 Design of parallel algorithms**

Our parallel computing algorithm is developed on a desktop computer with eight physical processors running under Windows 10. Two parallel computing algorithms, MPI and OpenMP, are chosen because they easily access to the subroutines and modules. The library of MPI can be called from FORTRAN, C, and C++ platforms. MPI (Dongarra, et al., 1993; Pacheco and Ming, 1995) allows the individual processor to perform complicated message delivery to other processors on different cores. Parallel computations are implemented on distributed memory devices to let each processor has its own memory space. In the forward modeling, the computation of each frequency can be regarded as an independent task; no data is shared between the slave processors. In addition, each independent task includes a large

number of data computations, logical judgments, and many subroutines. Therefore, frequency-level tasks are very coarse-grained assignments that are suitable for MPI. MPI can get a good speedup, however, the data computations in the sub-tasks need more communication.

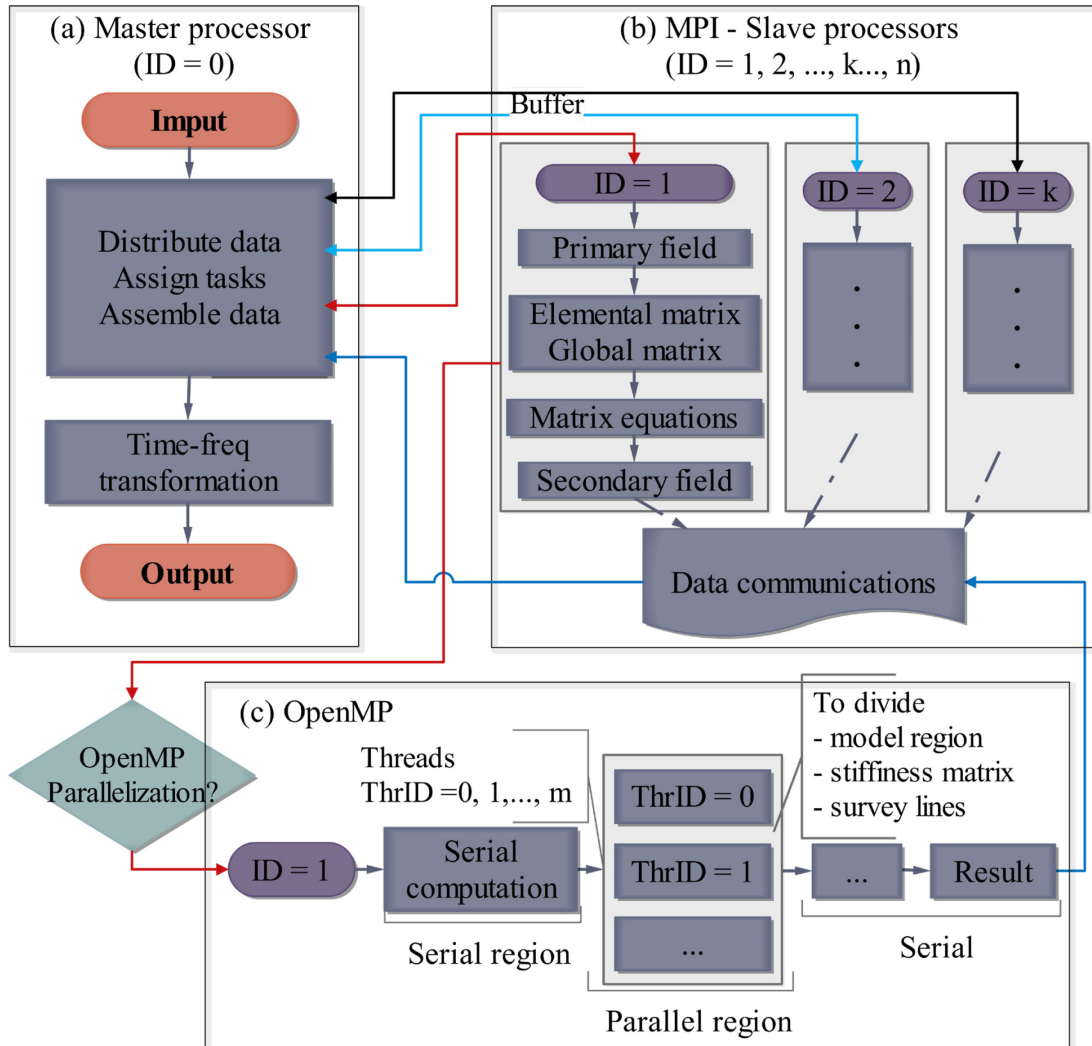


Figure 3.2: The procedure of parallel computation based on MPI, (a) master processor, (b) slave processors, and (c) further parallelization based on OpenMP

OpenMP (Chandra, et al., 2001; Chapman, et al., 2008) is a library designed for the shared memory device. OpenMP has the ability to parallelize small parts of a task, such as Do-loop, sections, IF, etc. In the sub-task process, whenever parallelism is demanded, OpenMP lets more threads join the computations. This strategy provides a way to avoid time-consuming communications between processors in MPI. Based on some synthetic models, we compared the two methods and analyzed their respective advantages and disadvantages.

Figure 3.2 illustrates the procedure of parallel computation based on MPI (Figure 3.2a and Figure 3.2b) and hybrid MPI/OpenMP (Figure 3.2c). MPI belongs to the distributed memory model and has no data replacement problem since MPI communications are employed by sending and receiving messages to exchange data. Though MPI is suitable for the coarse-grained parallelism, it has problems of memory and computational cost due to collective communications and load balancing. In contrast, OpenMP easily implements parallelism, with low latency/high bandwidth communications and dynamic load balancing. Moreover, implicit communications in OpenMP reduce communication time and memory consumption due to its shared memory architecture.

To benefit from both advantages, a hybrid MPI/OpenMP parallel programming is developed in this study, in which it reduces memory usage, loads imbalances and communication costs, and implements effective nested parallelism of MPI and OpenMP. It can save much memory when the same or better speedup is achieved. In order to make the calculation independent of the processor, a master-slave mode is implemented, in which the task is assigned to the slave-processor by the master-processor.

In the 3D TEM forward modeling, two parts of time-consuming computations are the frequency loop (outer loop) and the data calculations (inner loops).

(a) Frequency loop (outer loop):

The EM numerical modeling is calculated with tens of frequencies, and then the response is transformed from the frequency domain into the time domain. The forward modeling can be divided into many independent sub-tasks by frequencies. We controlled the data communication between the master processor and the slave processors, and no data is shared between the slave processors. The frequency-level tasks can be regarded as task-level parallelism (coarse-grained assignments), and they are data-independent, in which the MPI is used for controlling the whole calculations explicitly at the top level (Figure 3.2a and 2b).

(b) Data calculations (inner loops):

In the inner loops, a large number of data computations and logical judgments, and many subroutines are employed. The data computations consist of forming a stiffness matrix, solving large matrix equations, computing the secondary field with a large number of survey stations in the EM numerical modeling (Figure 3.2b). All these procedures are time-consuming and data-dependent. In parallel computing, they belong to the fine-grained task at the lower level. Both MPI and OpenMP can be used to implement the lower level parallelism. OpenMP is easy to implement and adapt to the codes (Figure 3.2c) since it provides an efficient way to exploit the lower level parallelism to keep the computational cost as lower as possible, in which the load balance problem is controlled by reducing the number of MPI processors in the outer loop.

### 3.3.2 Test of the parallel computation and the efficiency analysis

The tests have been carried out on the machine with Intel E5-1660 v4 (3.20GHz and 32GB memory), eight physical processors running under Windows 10. Each one has two logical processors. Let  $T_1$  be the sequential computation time of one processor and  $T_p$  be the computation time of the parallel computation executed on  $p$  processors ( $p$  denotes the number of processors). The speedup is given by  $S = T_1/T_p$ , and the speedup divided by the number of the processors is the efficiency ( $E = S/p$ ) (Chapman, et al., 2008).

#### ➤ MPI tests

Two even and uneven modes are used to distribute the assignments. In the even mode, the assignments are distributed evenly among the processors; each processor has the fixed assignments. In the uneven mode, the assignments are distributed unevenly; each processor computes the assignments competitively.

Two models are built for the evaluation of the MPI parallel computation, they have different grids to evaluate the impact of the number of nodes.

- Model 1 (M1): The numbers of nodes in the north, east and vertical directions are  $N_n = 37$ ,  $N_e = 39$ , and  $N_z = 37$ , respectively. The total number of nodes is 53391.
- Model 2 (M2): The numbers of nodes in the north, east and vertical directions are  $N_n = 45$ ,  $N_e = 47$ ,  $N_z = 46$ . The total number of nodes is 97290.

Table 3.1: The parallel efficiency ( $\epsilon$ ) for even/uneven mode MPI parallelizations.

Models	Modes	Number of processors							
		3	4	5	6	7	8	9	10
M1	Even	58%	63%	65%	65%	64%	63%	42%	37%
	Uneven	71%	78%	80%	81%	79%	78%	76%	65%
M2	Even	57%	62%	64%	66%	64%	65%	41%	37%
	Uneven	66%	71%	73%	77%	73%	74%	70%	63%

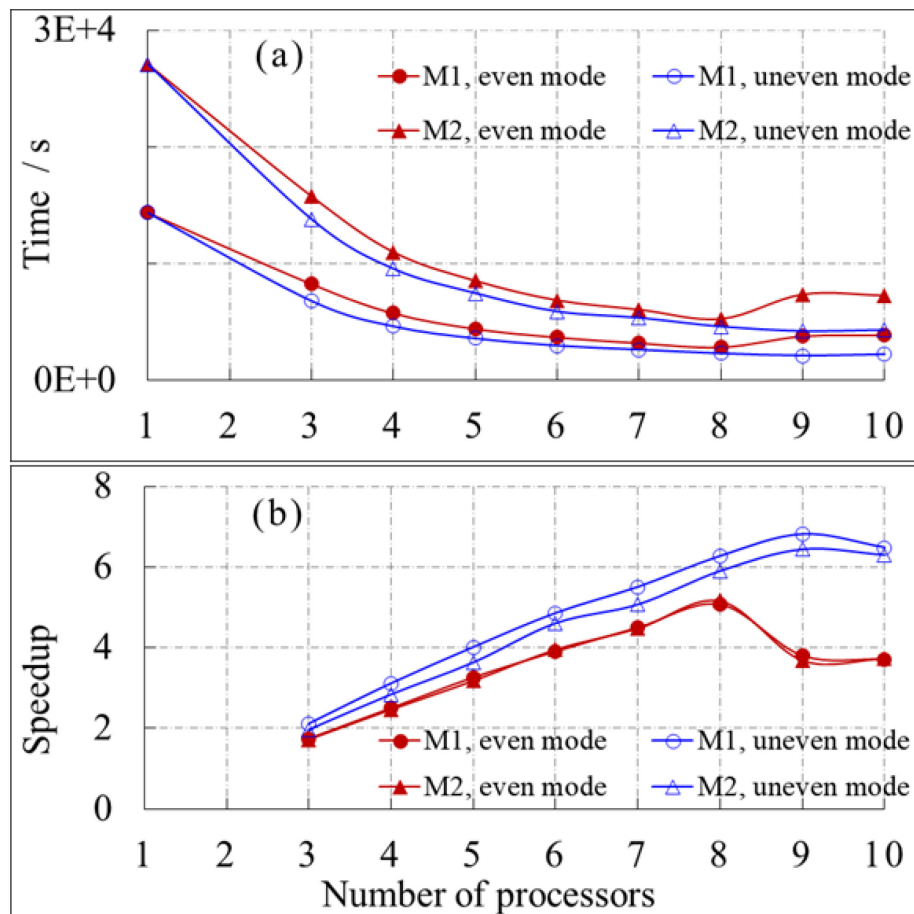


Figure 3.3: Results of MPI parallel computation on even/uneven mode: The computation time (a), the speedup (b).

Figure 3.3 illustrates how the computation time decreases by increasing the number of processors. However, there is a certain threshold where increasing the number of processors does not affect the computation time. The even mode achieves the maximum speedup (5.2) at eight processors in the MPI parallel computations, and then the speedup decreases quickly after eight processors. The uneven mode exhibits an improvement and gives the maximum speedup (6.8) around nine processors. As can be seen in Table 3.1, the efficiency first increases up to 81% for model 1 in the uneven mode, but it drops to 65% when ten processors are deployed. As increasing the number of processors, collective communications and load balancing are two main factors to limit the MPI parallel performance. Since the communication is controlled in our tests and it only happens between the slave processors and the master processor, the communication does not affect the speedup. Therefore, the load balancing is the major influencing factor on speedup.

The load balancing is also estimated by testing the time consumed in each frequency. Figure 3.4 illustrates the average of the accumulatively consumed time for all frequencies when the different number of processors are used. When the number of deployed processors is bigger than the number of physical processors, the load imbalance declines. Through the analysis of the average time, we can see that the average time changes slightly before eight processors, but more time is needed to finish the same task when the number of processors reaches to nine (Figure 3.4). This is in accordance with the results in Figure 3.3b where speedup increases from three to eight processors and then decreases after nine processors on the even mode. It indicates that two logical processors in one physical processor competitively use the computer resources (one processor must wait for the computer resources taken by another one). To reduce the load imbalance, an effective strategy is to distribute assignments

unevenly (Figure 3.3). An alternative way is to apply the fine-grained parallelization OpenMP as discussed in the section as follows.

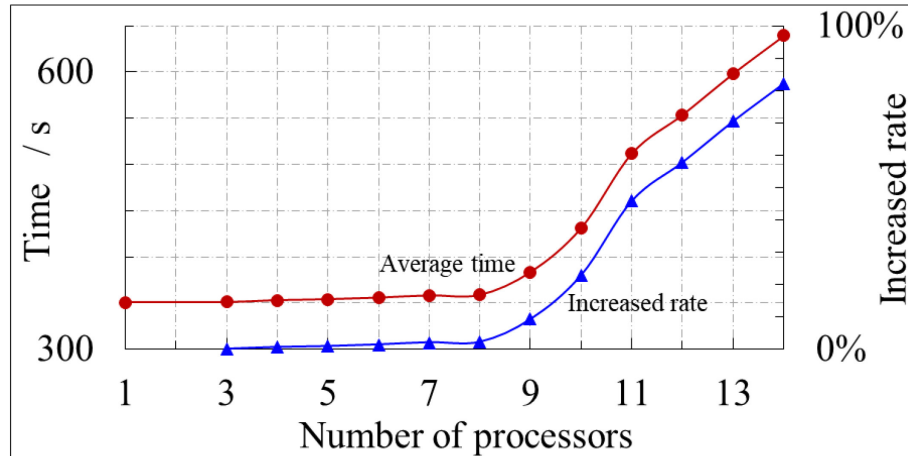


Figure 3.4: Average of accumulatively consumed time for all frequencies when a different number of processors is used, and the increased rate relative to the average time in the

sequential computation. On the y axis,  $time = \frac{1}{p} \sum_i^a t_i$ ,  $t_i$  is the computation time of  $i^{th}$

assignment in one processor,  $a$  is the number of assignments.

➤ OpenMP test

To analyze the performance of OpenMP parallel algorithm and to show the effect of threads on computation time, we perform the simulations on a single frequency (0.1Hz) while increasing the number of threads. The results are shown in Table 3.2 (OpenMP parallel algorithm in one sub-task). Although the computation time decreases by increasing the number of threads, the speedup changes slightly, and the parallel efficiency of OpenMP decreases quickly. The optimal speedup is 2.5 if one keeps the efficiency greater than 50%. The computation time increases up to 961s for the sequential code as increasing the number

of cells up to 97290 at the frequency 0.1Hz. However, in the same condition, it only takes 384s for the parallelized code with five threads. Compared to MPI, the high efficiency is obtained when a small number of threads is used, such as 87% in two threads, 74% in three threads for the model 2 (Table 3.2).

Table 3.2: Computation time for OpenMP parallelization in one frequency point (0.1Hz)

Models		T <sub>1</sub> (s)	T <sub>p</sub> – computation time (s) (frequency = 0.1Hz)						
			2	3	4	5	6	7	8
Model 1	Time	534	312	243	216	208	195	186	177
	Speedup	-	1.71	2.20	2.47	2.57	2.74	2.87	3.02
	Efficiency	-	86%	73%	62%	51%	46%	41%	38%
Model 2	Time	961	553	435	398	384	367	363	358
	Speedup	-	1.74	2.21	2.41	2.50	2.62	2.65	2.68
	Efficiency	-	87%	74%	60%	50%	44%	38%	34%

MPI is useful for coarse-grained assignments, such as frequency loop calculations in the TEM forward modeling. The main advantage of OpenMP is the high-efficiency fine-grained computation without communication, such as matrix operations in the finite element method. Therefore, we propose a hybrid algorithm to combine the advantages of both openMP and MPI methods in the section as follows.

- Hybrid MPI/OpenMP test

As indicated that tens of frequencies are used in the frequency-domain forward modeling, therefore, the calculation of each frequency is assigned to each processor of MPI parallelization on the basis of data independence. The matrix operations in the frequency are parallelized with OpenMP. Therefore, OpenMP forks a team of parallel threads, in which each thread calculates one part of the matrix in the matrix operations.

Table 3.3: Computation time for hybrid MPI/OpenMP with the uneven mode on the entire forward modeling.

Models		Time in sequential computing	Time in parallel computing	
			Case I	Case II
Model 1	Time (s)	14 357	3 184	2 662
	speedup	-	4.5	5.4
	Memory (GB)	-	2.2	2.8
Model 2	Time (s)	27 053	7 082	5 568
	speedup	-	3.8	4.9
	Memory (GB)	-	3.8	5.0

Table 3.3 illustrates the results of two cases for each model (Model 1 and Model 2), case I: three processors in MPI and two threads in OpenMP, case II: four processors in MPI and two threads in OpenMP. For the same number of processors used in MPI parallelization, the hybrid parallelization is much faster than MPI parallelization on both even and uneven modes. With the same number of processors and threads, the hybrid parallelization shows larger speedups compared to the even mode MPI parallelization, and smaller speedups

compared to the uneven mode MPI parallelization. However, the computer memory for MPI parallelization is almost two times of that hybrid parallelization. For Model 2, Hybrid parallelization takes 3.8GB when the case II is deployed and MPI parallelization takes 7.7GB when six processors are deployed. This is because in the MPI algorithm one sub-task is processed in one processor which cannot be shared like the OpenMP algorithm.

Though on the small number of mesh elements all the MPI, OpenMP and MPI/OpenMP algorithms represent satisfactory computational cost, however, the computational cost rapidly increases as the number of mesh elements increases in 3D space. One way to tackle this problem is to reduce the number of mesh elements involved in calculations. In Section 3.4, we deploy multiple meshes technology to further improve the efficiency of TEM forward modeling on large conductivity models.

### **3.4 Multiple meshes technology**

Besides the parallelization, another way to accelerate the EM forward modeling is to use multiple meshes to discretize the 3D subsurface volume. Whether using finite difference, finite volume, or finite element techniques, the main challenge in 3D EM forward modeling is the ever-growing computational costs, specifically for larger and more complex electrical conductivity structures. To avoid overload of mesh elements in the conductivity models, moving footprint method is used in the airborne electromagnetic modeling (Cox, et al., 2010, 2012; Yang, et al., 2013; Yin, et al., 2014). Each sounding has its own mesh structure that eventually reduces the computational cost of the EM forward modeling with sparser matrices. Commer and Newman (2006) developed the geometric multigrid concept. They used the finite difference method with the explicit time-stepping scheme, and a fine mesh is designed

in the early time and coarser mesh in the late time, the media on the coarse cells are calculated with the material averaging scheme. Moreover, Commer and Newman (2008) proposed a method in which simulation grids are decoupled from model grids. Simulation grids are adjusted according to the configuration of the measurement system and the spatial resolution of the physical model. Model grids represent the conductivity model of the survey area.

### 3.4.1 Multiple meshes design

Based on the fact of the change in the EM field and skin effect from low frequency to high frequency, we can define the effective region in 3D space for each frequency. The different model dimensions and mesh strategies can be deployed for different frequencies. However, deploying too many meshes in the forward modeling may increase the computational cost during the pre-processing procedures.

To reduce the computational cost, one strategy is the incorporation of coarse mesh in the lower frequencies, and fine mesh in the high frequencies. Figure 3.5 illustrates the geometry of fine and coarse cells in one slice. For the new cells, the averaging resistivity is used to calculate the resistivities of coarse cells. Here,  $n$  denotes the number of fine cells around or contained by the  $k^{\text{th}}$  coarse cell. The resistivities of the fine cells connected with the coarse cell are  $\rho'_i$  ( $i = 1, 2, \dots, n$ ), and the intersection of the volume between the coarse cell and each fine cell is  $V'_i$  ( $i = 1, 2, \dots, n$ ). Taking the average, we get the resistivity of the  $k^{\text{th}}$  coarse cell,

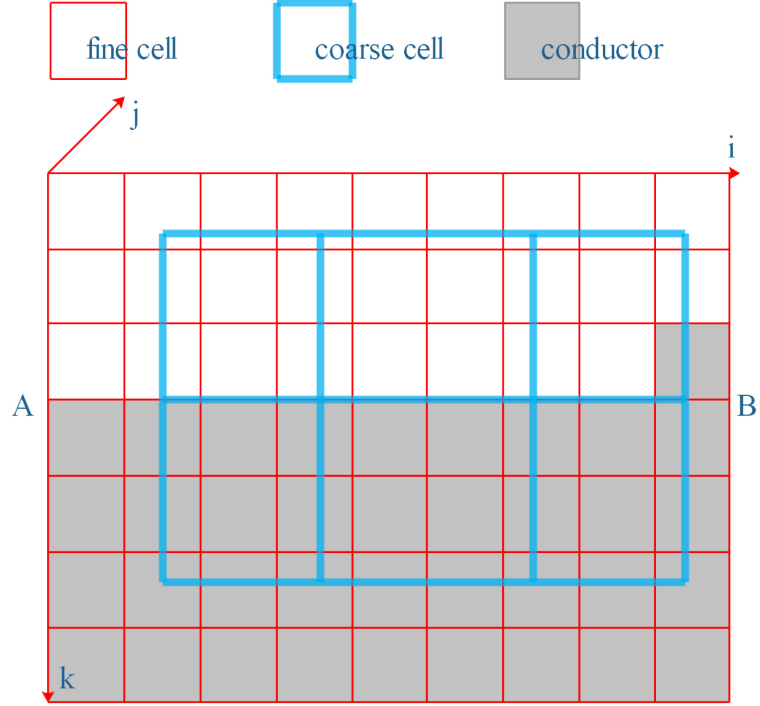


Figure 3.5: Geometry of the fine and coarse cells in one slice

$$\rho_k = \frac{1}{V_k} \sum_i^n \rho'_i \cdot V'_i \quad (3.6)$$

Where,  $\rho_k$  and  $V_k$  denote the resistivity and volume of the  $k^{\text{th}}$  coarse cell. A more simple approximate formula is,

$$\rho_k = \frac{1}{\sum_i^n d_{ki}} \sum_i^n \rho'_i \cdot d_{ki} \quad (3.7)$$

Where  $d_{ki}$  denotes the distance between the center points of the  $k^{\text{th}}$  coarse cell and  $i^{\text{th}}$  fine cell. In general, the fine cells and coarse cells share the same surface on the boundary of two media to keep that the fine mesh and coarse mesh present the same geological model, such as the sharing surface AB as shown in Figure 3.5.

The discretization of multiple meshes is an effective method for the computational cost of EM forward modeling while achieving the same responses. The reduction of cells in the low frequencies decreases the dimensions of the stiffness matrix, that makes the forward modeling memory-saving and time-saving. The multiple meshes technology can help to solve multiple conductive structures, but it is limited by sharp variations on boundaries. One needs to consider small cell sizes around the abrupt conductivity variations to ensure accurate EM field simulations. The cell sizes are dependent on the shapes and the dimensions of the conductors. The following criteria are used in this study:

(a) Incorporation of smaller cells near the surface (the top 10-20m) to effectively map the EM fields related to the rapid changes of overburden conductivities. The cell sizes are expanded by a ratio as the depth increases. According to the different frequency ranges in multiple meshes, different ratios are deployed.

(b) Incorporation of smaller cells near the TEM transmitter (10-20m around the loop). Cell sizes are set to increase far away from the transmitter (up to 100m). The ratio of increase is also modified when the frequency range changes in the multiple meshes design.

(c) Smaller cells near the interfaces of different conductivity zones. Using smaller mesh elements near the conductivity boundaries, it makes sure a smooth estimation of TEM fields through the forward modeling is achieved. The cell aspect ratio is restricted to avoid sharp cells.

Table 3.4: Specifications of grids

Grids		Parameters
Type a	Number of cells ( $N_n \times N_e \times N_z$ )	$37 \times 39 \times 28 = 40\ 404$
	Min/max cell size	25m, 50m
Type b	Number of cells ( $N_n \times N_e \times N_z$ )	$44 \times 42 \times 43 = 79\ 464$
	Min/max cell size	10m, 50m
Type c	Number of cells ( $N_n \times N_e \times N_z$ )	$45 \times 57 \times 52 = 133\ 380$
	Min/max cell size	10m, 50m

### 3.4.2 Analysis of multiple meshes

Three types of grids are used to analyze the time taken in different frequencies for the surface-borehole TEM forward modeling. Table 3.4 presents the parameters of the grids, and Figure 3.6 illustrates the computation time with respect to the frequency.

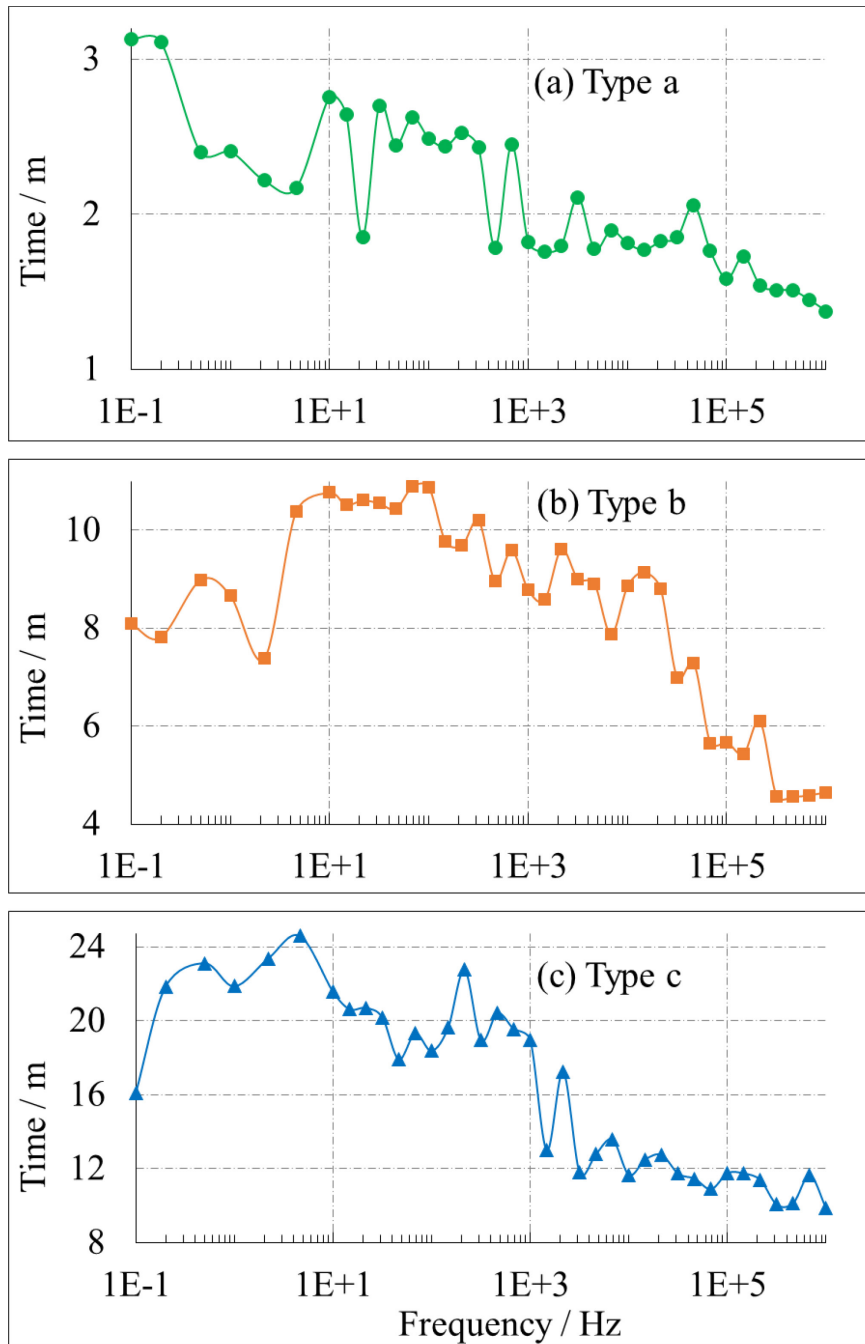


Figure 3.6: Time taken at different frequencies

As can be seen in Figure 3.6, as the frequency increases, the corresponding computation time gradually decreases. In Figures 3.6a and 3.6c, the time taken in the frequency range  $(0, 10^3]$  is more significant than the time taken in the frequency range  $[10^3, 10^6]$ . Based on this

discrepancy, two different mesh structures can be generated to cover the two distinct frequencies ranges: a coarse mesh structure can be used to process the frequencies from 0 to  $10^3$ Hz, and a fine mesh structure for the frequencies from  $10^3$  to  $10^6$ Hz. However, in Figure 3.6b (Type b), the frequencies in the range of  $[10^3, 5 \times 10^4]$  still consume too much time. Therefore, a medium mesh is further added for the frequency range of  $[10^3, 5 \times 10^4]$ , and then finer meshes are added for the frequencies of  $(5 \times 10^4, 10^6]$ .

Table 3.5: Specifications of grids and meshes.

Grids		Multiple meshes		
		Low frequencies (Coarse mesh)	Medium frequencies (Medium mesh)	High frequencies (Fine mesh)
Type a	Number of cells ( $N_n \times N_e \times N_z$ )	$32 \times 32 \times 28 = 28\ 672$	-	$37 \times 39 \times 28 = 40\ 404$
	Min/max cell size	25m, 70m	-	25m, 50m
Type b	Number of cells ( $N_n \times N_e \times N_z$ )	$37 \times 36 \times 38 = 50\ 616$	$41 \times 38 \times 40 = 62\ 320$	$44 \times 42 \times 43 = 79\ 464$
	Min/max cellsize	10m, 60m	10m, 60m	10m, 50m

The following tests are conducted to compare the designs of the single mesh and multiple meshes. Two types of grids (Type a and Type b) are used to test the multiple meshes technology. Type *a* only uses two meshes, fine mesh for high frequencies, and coarser mesh for low frequencies. Three meshes are used in type *b* (fine, medium and coarse meshes). The

details are shown in Table 3.5, and the time taken in each frequency range is represented in Figure 3.7.

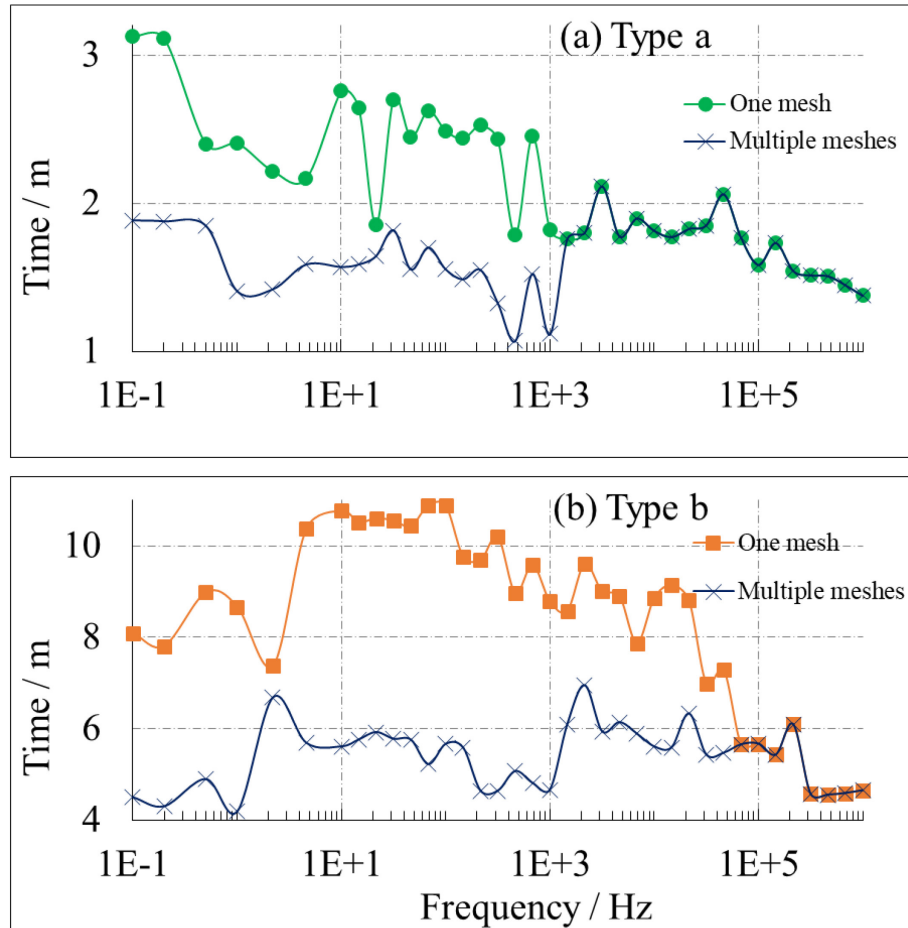


Figure 3.7: Comparisons of time between two types of meshes

As can be seen in Figure 3.7, compared to the single mesh design, in multiple meshes discretization, the computation time is reduced to half for low frequencies. For the high frequencies, they take the same time due to the same number of mesh elements in both types a and b. The significance of multiple meshes is that for the low frequencies the reduction of

the mesh elements is an effective method to reduce the computational cost in the TEM forward modeling (time-frequency transformation).

The choice of mesh is dependent on frequencies. In theory, we can design an individual mesh for each frequency, for example, 30 frequencies need 30 meshes in the forward modeling, however, too much time of preprocessing may be taken. Therefore, one effective strategy is to divide the frequency range  $(0 \sim 10^6]$  into several fragments. The cell size determines the precision of the result. Therefore, the maximum cell size is controlled. In addition, the cell size is dependent on the shapes, dimensions and resistivities of the conductors.

### **3.4.3 Parallel computing with multiple meshes**

The advantage of parallelization computation is the task partitioning; multiple meshes technology gives different frequency ranges independent mesh strategies. To combine their advantages, we integrated the multiple meshes into the parallelized surface-borehole TEM forward modeling. The same tests (types a and b) are used to analyze the performance of parallel EM forward modeling with multiple meshes.

Figure 3.8 illustrates that multiple meshes technology is a highly effective strategy to speed up the surface-borehole TEM forward modeling. Compared to the sequential run using one mesh, it can achieve 13 times speedup when nine processors are used. In comparison with one mesh case (Figure 3.3), the improvement is obvious for timesaving. Table 3.6 illustrates the impact of cells number. With increasing the number of cells (from type a to b), computation time increases exponentially. However, with multiple meshes in parallel EM forward modeling, the computation time is reduced from 18688s to 1371s when nine

processors run. Therefore, the role of multiple meshes is even more important to reduce computational cost in 3D TEM forward modeling.

Table 3.6: Speedup of Type a and Type b with multiple meshes (only three cases (1, 5, and 9 processors) are used in Type b)

Grids		One mesh with sequential computing	Parallelized multiple meshes				
			Number of processors				
			1	3	5	7	9
Type a	Time	4700s	3687s	1142s	622s	473s	372s
	Speedup	-	1.27	4.12	7.56	9.94	12.63
Type b	Time	18688s	12138s	-	2456s	-	1371s
	Speedup	-	1.54	-	7.61	-	13.63

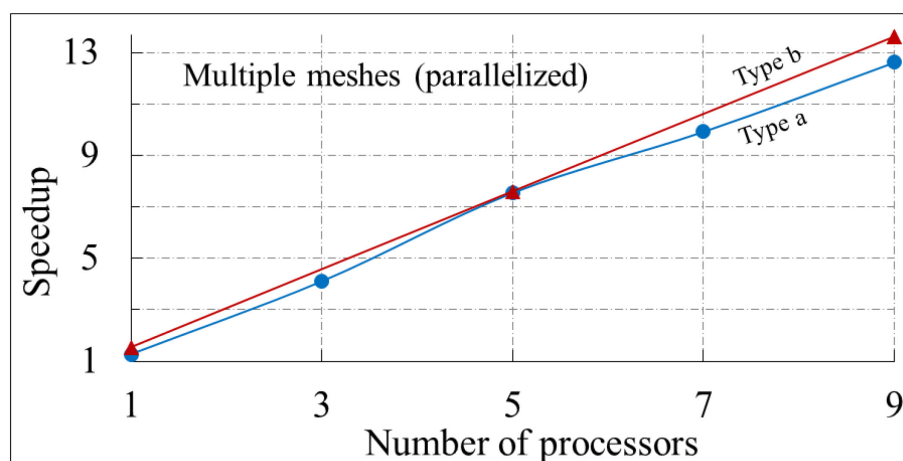


Figure 3.8: Speedup of the parallelized surface-borehole TEM with multiple meshes.

### **3.5 Conclusions**

In this study, we present two parallelization algorithms (MPI algorithm and hybrid MPI/OpenMP algorithm) for 3D surface-borehole TEM forward modeling. The OpenMP parallelization algorithm can archive three times speedup. MPI parallelization can get a better speedup as increasing the number of processors. Using MPI to split the task into many sub-tasks delivered into each processor, while using OpenMP to break large domain (model data, survey lines, stiffness matrix...) into smaller sub-domains shared within threads in order to reduce the computer memory and communication time caused by data exchange. With the same number of processors used in the MPI parallelization, the hybrid MPI/OpenMP algorithm shows a better performance than MPI.

The multiple meshes technology can further accelerate the 3D surface-borehole TEM forward modeling. It, moreover, reduces computer memory usage due to the reduction of the number of cells in low frequencies.

## CHAPTER 4

### IMPROVEMENT OF THE EFFICIENCY OF TIME-DOMAIN ELECTROMAGNETIC MEASUREMENT

#### 4.1 Introduction

Combining ground, airborne and borehole time-domain electromagnetic (TEM) measurements can help to investigate the structural geology in three dimensions. As an example, borehole EM systems interact with rocks around the probe, beside or beneath the boreholes with a detection limit of up to 500m. Therefore, it provides three-dimensional information around the borehole; particularly it is useful for targeting deeply buried ore bodies. How to maximize the efficiency of TEM surveys for deep mineral exploration is, therefore, the focus of the present study.

Over the past few decades, many researchers have studied the effects of the parameters of the TEM measurement system on detection efficiency. It includes the effects of different transmitter waveforms (Liu, 1998; Qin, 2013), the effect of ramp turn-off time (Raiche, 1984; Fitterman and Anderson, 1984 and 1987; Lu, 1999; Chen 2012), and the effect of pulse width (Becker et al., 1984; Liu, 1998; Smith, 1998).

Liu (1998) found that the amplitude of the EM signal is proportional to the area between the transmitter waveform and the time axis. Therefore, the square waveform enhances the target's signal (Liu, 1998; Qin, 2013). The ramp turn-off time represents the duration of vanishing the primary field after the transmitter turns off; it mainly affects the response in the early channels in off-time.

In order to have the pure inductive electromagnetic response as far as possible, the TEM systems record the signal after turning off the transmitter. However, due to the inductance of the transmitter loop, the turn-off takes a finite amount of time. If non-zero ramp turn-off does not take into account in the data processing, it can cause faulty interpretation (Fitterman and Anderson, 1984). Raiche (1984) mentioned that if the off-time origin were taken at the beginning of the ramp turn-off, the response due to the ramp function excitation would be greater than that due to step function excitation. According to the study of Fitterman and Anderson (1984 and 1987), as the duration of the ramp turn-off increases, the estimation of the apparent resistivity is less accurate for the early channels in off-time, especially for the resistive near-surface layers, but small effect on the later time channels. They noticed that if one takes the off-time zero at the end or start of the ramp turn-off, the apparent resistivity will be overestimated or underestimated respectively (Fitterman and Anderson, 1987). Chen (2012) remarked that the longer the ramp turn-off time, the smaller is the amplitude of the inductive EM response. To reduce the influence of varying ramp turn-off time, the castle waveform (e.g. UTEM) and rectangular waveform (e.g. SMARTem24 and DigiAtlantis systems) are used in modern system design.

With regard to the impact from the pulse width on the EM response, Becker et al. (1984) evaluated the effect of half-sine pulse width on a target of wire loop for airborne electromagnetic (AEM) survey. The pulse duration varies from 1ms to 2ms. They found that the signal of 2ms pulse decays 10-20% slower than that of 1ms pulse, and the pulse width has no effect on the target response while the target time constant is less than about 0.1ms. According to the study of Liu (1998), the bigger the pulse width, the greater the response is;

he also observed when the pulse width is twice the target time constant, it generates 85% of the response induced by an 'infinite width' pulse for the square pulse.

Besides the above influential parameters on the efficiency of a TEM system, the target time constant, pulse width and measured time collaboratively play a role in the shape and amplitude of inductive EM responses. With the 3D TEM simulation, we aim to define an optimal combination of multiple parameters for field survey design. Through the theoretical analysis, a general relationship between the pulse width, the measured time and the target time constant is proposed. However, such a theoretical relationship cannot be used for guiding TEM measurements in the field. Therefore, a specific functional relationship with some conditions is then created through this study. A series of numerical simulations have been done for generating the surface-borehole, ground and airborne TEM responses, and ultimately, looking for a consistent conclusion.

In this study, the numerical simulation uses the 3D EM forward modeling code – Loki, which was developed by the research group at CSIRO Australia (Raiche, et al., 2008). The numerical calculation is based on the edge-based finite element method. The TEM responses are first calculated in the frequency domain, and then they are transformed into the time domain. We did not evaluate the numerical accuracy of Loki because the present study is focused on its application. However, a study has demonstrated (Raiche et al., 2003) the accuracy of modeling with the Loki code by comparing the results with the results from physical scale modeling.

## 4.2 Pulse width study

### 4.2.1 Theoretical analysis of pulse width

Surface-Borehole EM, which is also called downhole EM or borehole EM, is one of the deep electromagnetic exploration methods (Dyck, 1991; Tweeton, Hanson, 1994). In general, its transmitter uses a bipolar on-off waveform with exponential turn-on and ramp turn-off as shown in Figure 4.1b. The long pulse width is beneficial to the response of the conductive body; however, many other factors can affect the inductive response, such as the intensity of the primary EM field, the transmitter waveforms, the target time constant, the coupling between the transmitter (Tx), conductor, and the receiver (Rx). With the help of computer tools, it is now possible to simulate the electromagnetic field in order to quantify the most significant factors to the EM induction.

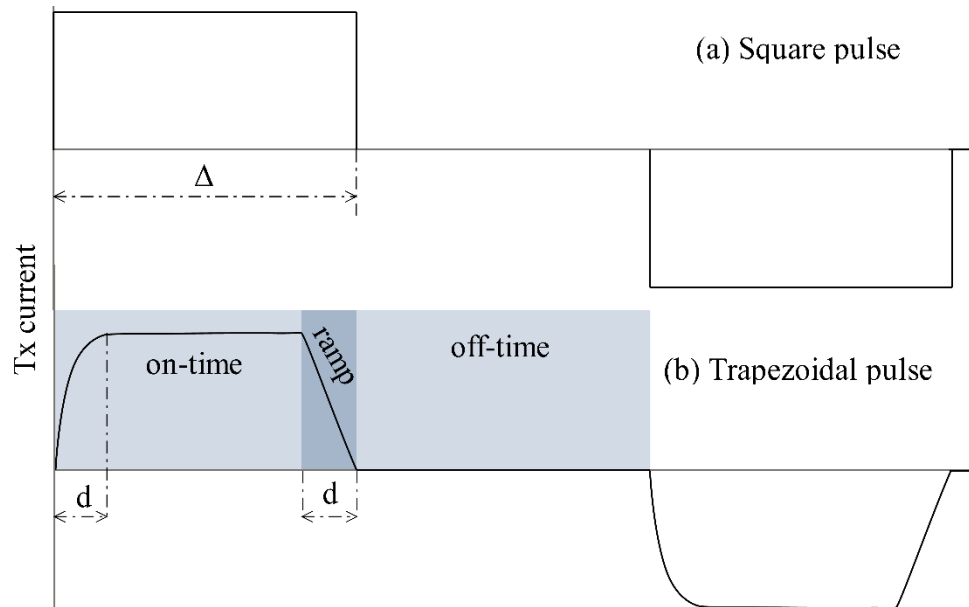


Figure 4.1: The transmitter waveforms used in this study, (a) square pulse, (b) trapezoidal pulse

Neglecting the effects of pulse repetition, Becker et al. (1984) and Liu (1998) used the simple wire loop model to study the effect of the pulse width within a homogeneous half-space. Liu (1998) formulated the induced voltages as functions of pulse widths for trapezoidal and square waveforms,

$$\begin{cases} V_S(t) = \frac{a}{\tau} e^{-t/\tau} (1 - e^{-\Delta/\tau}) \\ V_T(t) = \frac{a}{d} e^{-t/\tau} \left[ (1 - e^{-d/\tau}) + e^{-\Delta/\tau} (1 - e^{d/\tau}) \right] \end{cases} \quad (4.1)$$

Where  $V_T$  and  $V_S$  are the voltages induced by the trapezoidal waveform and square waveform respectively,  $d$  is the ramp turn-off time.  $a$  is a constant related to the geometry and current amplitude of the transmitter,  $t$  is the time of off-time measurements. The time origin is taken at the end of the ramp turn-off of the transmitter waveform.  $\Delta$  is the pulse width,  $\tau$  is the target time constant. The target time constant can be approximately estimated by its average thickness and dimension based on the formula  $\tau = K\sigma\mu A$  (Lamontagne, 1975; Nabighian and Macnae, 1991),  $K$  is a coefficient and  $A$  is proportional to the effective cross-section of the conductor,  $\sigma$  is the conductivity of the conductor,  $\mu$  is the magnetic permeability of the conductor.

To introduce the effects of periodic current pulses, using  $V'(t)$  denotes  $V_S(t)$  and  $V_T(t)$ , taking the superposition of induction fields from the former pulses, yields,

$$V(t) = V'(t) - V'(t+T/2) + V'(t+2T/2) - V'(t+3T/2) + \dots \quad (4.2)$$

Where  $T$  is the period. Setting the duty cycle as  $k$  ( $0 < k < 1$ ),  $T = \Delta/k$ , then Equation (4.2) is synthesized as follows:

$$V(t) = f(\Delta, \tau) \cdot e^{-t/\tau} \quad (4.3)$$

Where V is the voltage that involves the periodicity effect. The synthetic factor (f) is,

$$f(\Delta, \tau) = \begin{cases} \frac{a}{\tau} \cdot \frac{1 - e^{-\Delta/\tau}}{1 - e^{-\Delta/k\tau}}, & \text{square pulse} \\ \frac{a}{d} \cdot \frac{(1 - e^{-d/\tau}) + e^{-\Delta/\tau} (1 - e^{d/\tau})}{1 - e^{-\Delta/k\tau}}, & \text{trapezoidal pulse} \end{cases} \quad (4.4)$$

Equation (4.3) represents the target response to a pulse width  $\Delta$ . For the pulse with infinite width  $\Delta_\infty$ , its response to the same target is,

$$V_{\Delta_\infty}(t) = \begin{cases} \frac{a}{\tau} \cdot e^{-t/\tau}, & \text{square pulse} \\ \frac{a}{d} (1 - e^{-d/\tau}) \cdot e^{-t/\tau}, & \text{trapezoidal pulse} \end{cases} \quad (4.5)$$

Then, the ratio (R) of induced voltage by a finite-width pulse to that of the infinite-width pulse is defined as follows,

$$R = \frac{V(t)}{V_{\Delta_\infty}(t)} = \begin{cases} \frac{(1 - e^{-\Delta/\tau})}{1 - e^{-\Delta/k\tau}}, & \text{square pulse} \\ \frac{(1 - e^{-d/\tau}) + e^{-\Delta/\tau} (1 - e^{d/\tau})}{(1 - e^{-\Delta/k\tau})(1 - e^{-d/\tau})}, & \text{trapezoidal pulse} \end{cases} \quad (4.6)$$

From Equation (4.6), the ratio (R) is independent of the measurement time (t). If the ramp turn-off time (d) is very small (trapezoidal waveform), the ratio R is proportional to the pulse width and reverse to the target time constant for both trapezoidal and square waveforms,

$$R \propto (\Delta/\tau) \quad (4.7)$$

Based on Equation (4.6), Figure 4.2 illustrates that the ratio (R) approaches 100% when the pulse width is larger than five times of target time constant; R falls quickly to 50% or less when the target time constant is bigger than the pulse width. For the trapezoidal waveform

(Figure 4.2b), the effect of ramp turn-off time ( $d$ ) on large time constants (e.g.  $\tau = 100\text{ms}$ ) is much smaller than that on small time constants (e.g.  $\tau = 1\text{ms}$ ,  $10\text{ms}$ ), which is favorable for high conductive mineral exploration. Figure 4.2b confirmed also that the smaller ramp turn-off time has less impact on the TEM response.

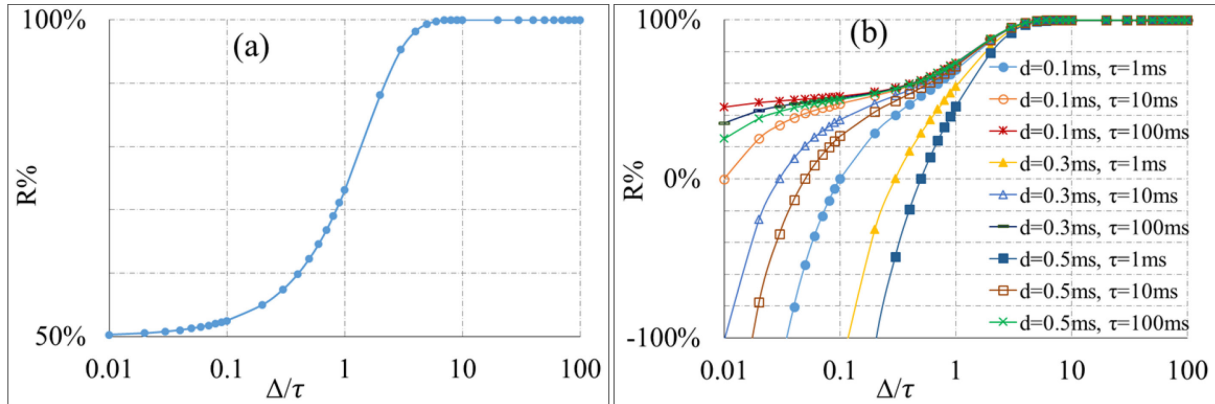


Figure 4.2: The ratio ( $R$ ) as a function of the ratio of the pulse width to the target time constant. (a) Square waveform, (b) trapezoidal waveform with a fixed ramp turn-off time ( $d=0.1, 0.3$  and  $0.5\text{ms}$ ). The duty cycles for both pulses are  $0.5$ .

#### 4.2.2 Effect of pulse width

A test has been carried out on a homogeneous half-space model (M1). M1 hosts a prismatic conductor with a dimension of  $200\text{m} \times 500\text{m} \times 100\text{m}$  that is buried at  $300\text{m}$  below the surface (Figure 4.3). In this study, all the dimensions are in terms of (EW x NS x thickness), and all the coordinates are in terms of (easting, northing, Z). A transmitter loop on the surface is the size of  $200\text{m} \times 500\text{m}$  and displayed directly over the prism. Two vertical boreholes are located at BH1 ( $400\text{m}, 500\text{m}, 0$ ) and BH2 ( $500\text{m}, 500\text{m}, 0$ ). In reality, we cannot numerically calculate the TEM response of the infinite-width pulse. The response induced by the infinite-width pulse is taken when there is no more change in the response as the pulse width

increases. In M1, the time constant of the prism is estimated as 2.3ms. Figure 4.4 illustrates the modeling results for the square and trapezoidal pulses respectively.

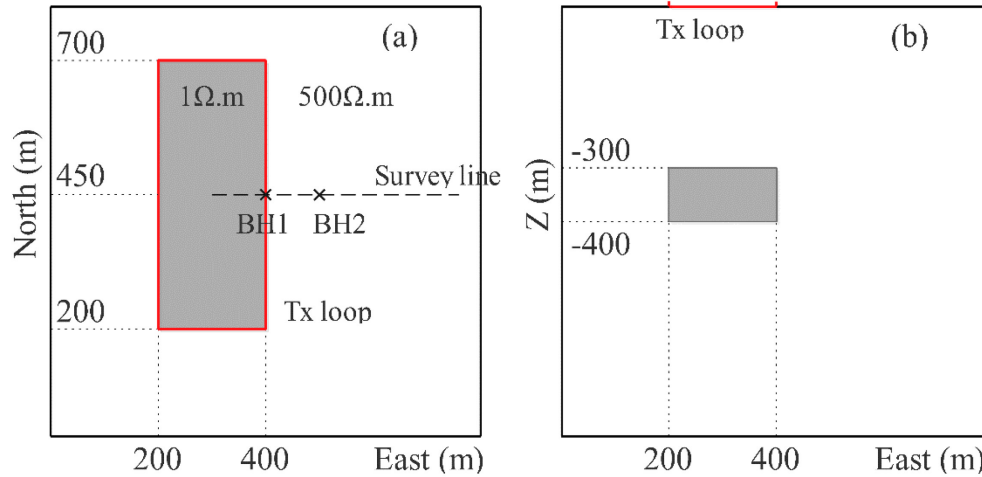


Figure 4.3: The model M1 consists of a prism with 1Ω·m resistivity in a 500Ω·m half-space, (a) top view, (b) section view.

From decay curves (Figure 4.4a, 4.4c, 4.4e, 4.4g), the larger pulse width corresponds to the slower decay in the late time. This might be the indication that longer transmitting time is beneficial to the full induction of the conductor. Figure 4.4b, 4.4d, 4.4f, 4.4h illustrate that the wider pulse is required to let R approach 100% for later time responses. According to those consistent results, the time effect on TEM signal quality is clear. Therefore, the equation (4.6) can be modified as,

$$R \propto (\Delta/\tau, t) \quad (4.8)$$

The target response is now dependent on the pulse width ( $\Delta$ ), the target time constant ( $\tau$ ), and the measurement time ( $t$ ) started from the end of the ramp turn-off.

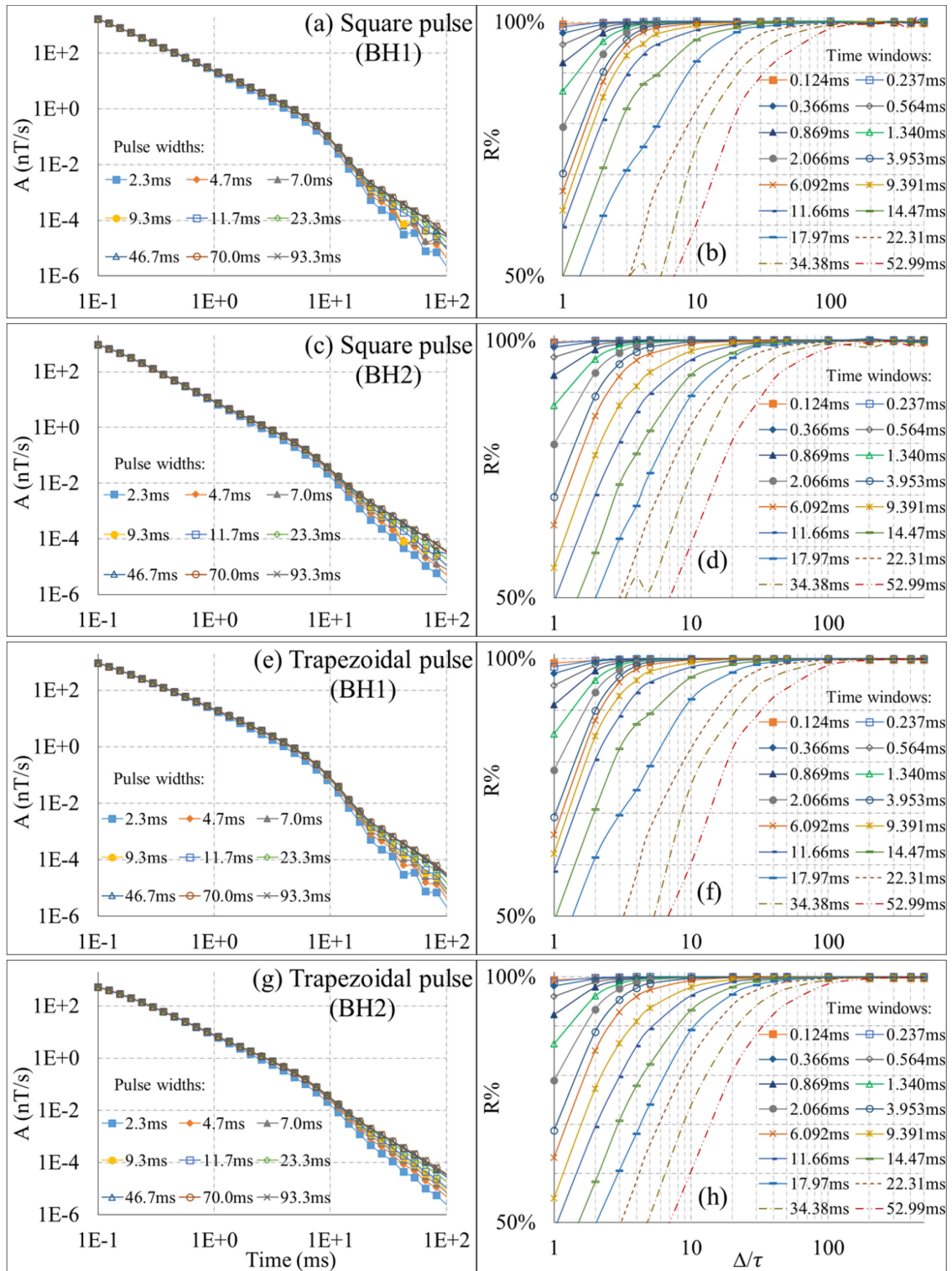


Figure 4.4: Surface-borehole TEM decays ( $A$  components) and the ratio  $R$  with different pulse widths for the model M1, (a, b) square pulse in BH1, (c, d) square pulse in BH2, (e, f) trapezoidal pulse in BH1, (g, h) trapezoidal pulse in BH2.

### 4.3 Simulations and verifications

To verify the above general rule, a series of 3D numerical simulations have realized for three typical surveys, which are surface-borehole TEM, ground TEM and airborne TEM measurements within a layered earth environment. Table 4.1 summarizes the parameters of some commercial TEM systems; however, the range of all possible variations (pulse widths and off-times) has been considered in the TEM modeling, rather than a specific system with its parameters

Table 4.1: Parameters of some common TEM systems with trapezoidal or square waveforms.

Systems (duty cycle)	Airborne TEM		Ground TEM and Borehole TEM			
	SKYTEM (25%, 50%)	NEWTEM VTEM (50%)	PROTEM& TEM 47 (50%)	SMARTem DigiAtlantis (25%, 50%, 100%)	UTEM (100%)	Crone PEM (50%)
Base frequency (Hz)	12.5, 25	25, 30	25, 62.5, 237.5 or 30, 75, 285	0.001 – 10k	~1 – 90	0.25 – 30
Pulse width (ms)	10	8.3 or 10	1 – 10	-	-	8.3 – 1000
Off-time (ms)	30 or 10	8.3 or 10	1 – 10	-	-	8.3 – 1000

### 4.3.1 Surface-borehole TEM

The model (M2) consists of three resistive layers and two conductive layers. The layer (L4) is the most conductive ( $3.5\Omega\cdot\text{m}$ ), and its time constant ( $\tau$ ) is estimated as 2.5ms. The dimension of M2 is 1000m x 1000m x 1000m (Figure 4.5). The transmitter loop (100m x 200m) is over the borehole BH, its central location is at (250m, 500m, 0m), and the receiver is placed in the borehole BH. Trapezoidal and square waveforms with different pulse widths are used in the simulations of TEM responses. The pulse widths are 2.5ms, 5.1ms, 7.6ms, 10.2ms, 12.7ms, 25.4ms, 50.8ms, 76.2ms, 101.6ms, 126.9ms, 253.9ms, 507.8ms. Figures 4.6a-d illustrate the TEM responses of coaxial component (A) and the ratio R of surface-borehole TEM.

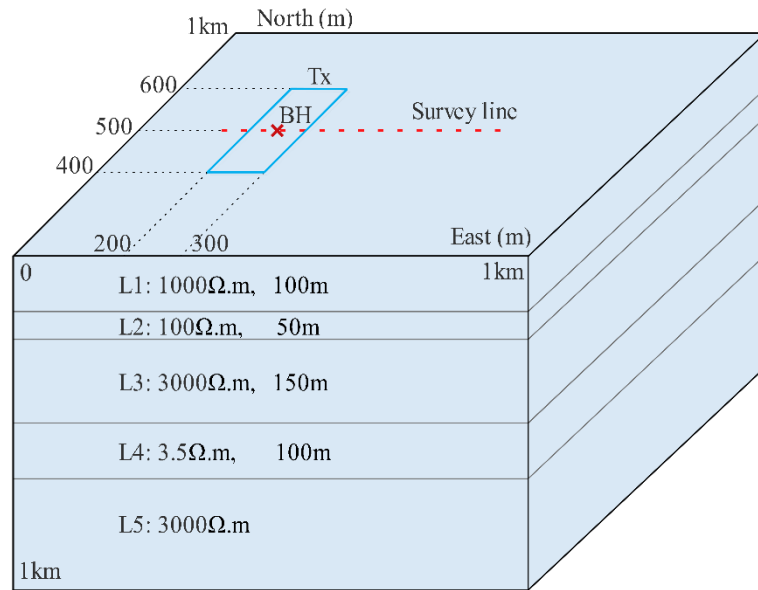


Figure 4.5: The layered model M2, and the configuration of the transmitter loop (Tx), the borehole BH, and the survey line.

Figures 4.6a-d prove that the effect of time on the ratio R is very significant for both square and trapezoidal waveforms. As increasing the pulse width, it enhances the deep conductive layer's response. The larger the pulse width is, the stronger the surface-borehole TEM response of the layer (L4) is in the late time channels.

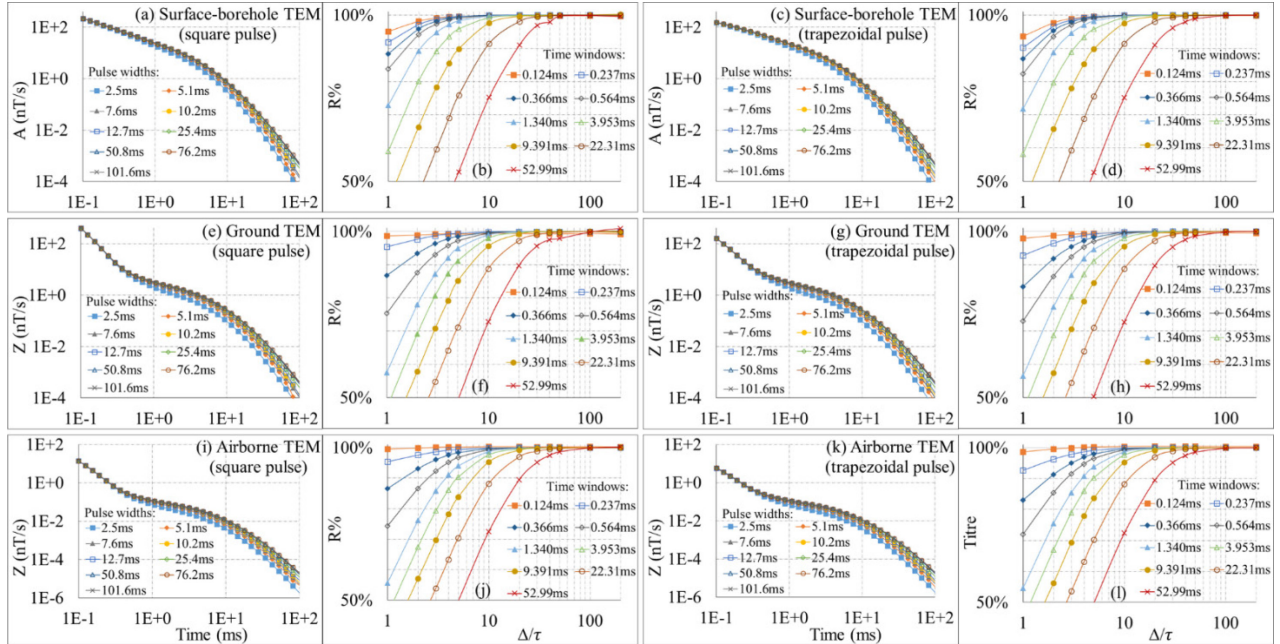


Figure 4.6: Decays of TEM responses generated by square and trapezoidal pulses, and the ratio R with varying pulse widths for the model M2. The simulations are implemented for surface-borehole TEM (a to d), ground TEM (e to h), and airborne TEM (i to l).

All TEM responses converge to 100% of R by increasing the pulse width through all time windows (Figure 4.6b, 4.6d). Therefore, the optimal pulse widths can be estimated from this diagram for different off-times. For example, for 10ms off-time, pulse width (12.7ms) of five times  $\tau$  can generate about 90% of the response of infinite-width pulse, and 50ms off-time needs 50ms pulse width (20 times  $\tau$ ). For deep exploration, if we know which type of

mineralization is going to be explored, estimating the range of the target time constant can help to choose an adequate pulse width. At least from the above results, if one searches for high conductive deposits (e.g. nickel) large pulse width is favorable.

### **4.3.2 Ground TEM**

For ground TEM, the transmitter and the receiver are both at the surface, and the component (Z) is simulated. The simulations use the same transmitter loop and waveforms as the surface-borehole TEM measurements, and the survey line is indicated in Figure 4.5. Figures 4.6e-h illustrate the similar effect of the pulse width and the measurement time on the responses as the surface-borehole TEM. In this case (52.99ms off-time), the pulse width with 20 times  $\tau$  is also required to get almost 90% of the target response of the infinite-width pulse.

### **4.3.3 Airborne TEM**

In the airborne TEM, the survey path is the same as the ground TEM (Figure 4.5), but the receiver is suspended at a height of 30 m above the surface. The pulse width and off-time are set individually without considering base frequency. Figures 4.6i-l illustrate the decays of TEM responses with time and the ratio R of M2, which are consistent with previous results. These results show that equation (4.8) satisfies all TEM systems that use square or trapezoidal waveforms. As indicated by Becker (1984) that a 2ms pulse width can result in a four-fold increase compared to a 1ms pulse width for the targets with the time constant larger than 2ms for the Input system. Based on the wire-loop model, Liu (1998) claimed that the pulse width of  $2\tau$  can make the ratio  $R = 85\%$ . According to this study, the optimal pulse width depends on off-time for the 3D body. In general, the pulse width of the airborne TEM survey must be short enough to be able to take a density of readings per unit of distance large enough to

ensure a low noise level (more stacking fold). For the base frequencies between 12.5 Hz and 30 Hz, the pulse widths of airborne TEM systems are usually less than 10ms (Table 4.1). Since there is more freedom in the choice of pulse width for ground and borehole TEM surveys, the present study could contribute to those surveys design.

#### 4.4 Formula of optimal pulse width and measurement time

##### 4.4.1 Optimal pulse width

We define a critical value  $R_0$ , which represents  $R = 80\%$  or higher (indicated by the dashed lines in Figure 4.7), then the Equation (4.8) can be rewritten as,

$$R(\Delta/\tau, t) = R_0 \quad (4.9)$$

Then we can build the functional relationship between  $\Delta$ ,  $\tau$ , and  $t$  for this specific value of  $R$ . As can be seen in Figure 4.8, the ratio  $(\Delta/\tau)$  changes linearly from 1ms to 100ms. The range of 1ms to 100ms is the general off-time for the TEM measurement, therefore, it is used to build the relationship between  $\Delta$ ,  $\tau$ , and  $t$ . Using linear fitting to the relationship between  $(\Delta/\tau)$  and  $t$  and defining  $c$  as the slope, yields,

$$\frac{\Delta}{\tau} = c \cdot t, \quad (1 < t < 100) \quad (4.10)$$

Then,  $c$  is a constant related to the ratio  $R$ ,  $c = 0.38$  for  $R = 80\%$ , and  $c = 0.62$  for  $R = 90\%$ . It must indicate that Equation 4.10 is not satisfied when  $t$  is very small ( $t < 1\text{ms}$ ) or very big ( $t > 100\text{ms}$ ) (Figure 4.8). Equation (4.10) can be used to evaluate the pulse widths for different off-times. As can be seen in Table 4.1, for the general TEM systems (25% or 50% duty cycle), pulse widths are less than or equal to off-times. According to Equation (4.10), when the value of  $(k \cdot \tau)$  is greater than one, pulse width should be greater than off-time to keep the signal quality. For example, to explore the conductor in the model M1, for Crone

PEM with 100ms off-time (Table 4.1), the reasonable pulse width is 87.4ms for  $R = 80\%$ , 142.6ms for  $R = 90\%$ . Traditionally, the base frequency determines the pulse width and off-time with the duty cycle. Instead, one can determine the base frequency by calculating a reasonable pulse width and off-time to ensure signal quality and improve the efficiency of TEM measurement.

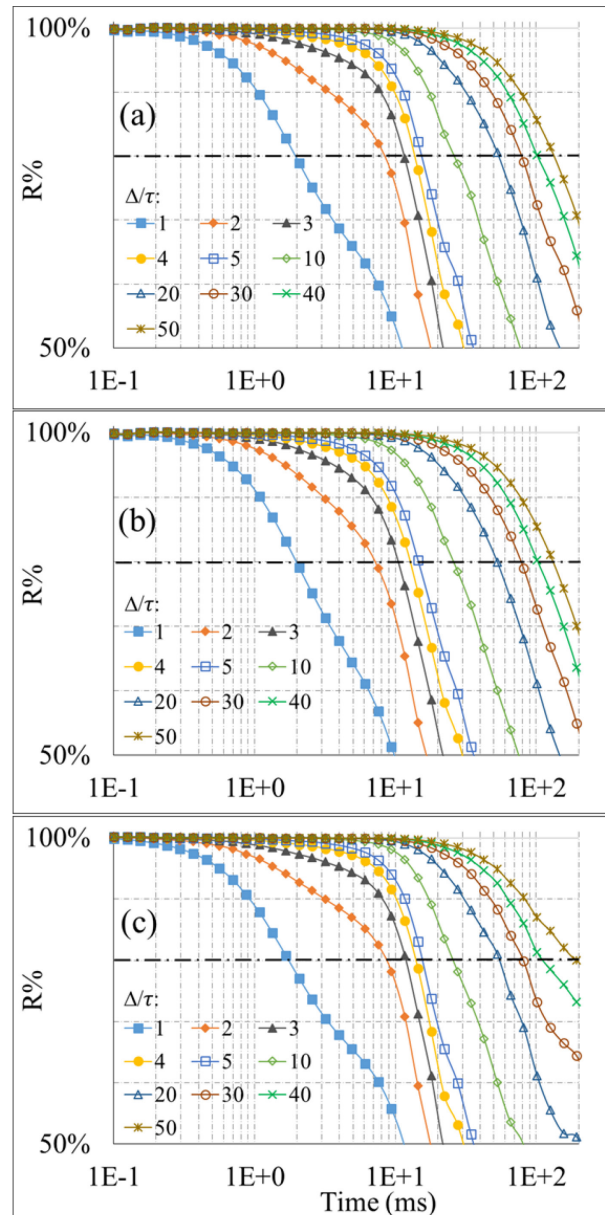


Figure 4.7: Ratio  $R$  as the function of time to different values of  $(\Delta/\tau)$  for the model M1 with surface-borehole TEM (a), ground TEM (b) and airborne TEM (c).

For the TEM measurement in the field, the data of the first survey station (or test point) can be used to approximately calculate the target time constant with the equation as follows (Nabighian and Macnae, 1991),

$$\tau = \frac{t_2 - t_1}{\ln(A(t_1) / A(t_2))} \quad (4.11)$$

Using the amplitudes  $A(t_1)$  and  $A(t_2)$  of two times  $t_1$  and  $t_2$ , one can approximately calculate the target time constant ( $\tau$ ). Then using Equation (4.10), the approximate pulse width can be designed for a specific off-time to keep  $R = 80\%$  or higher.

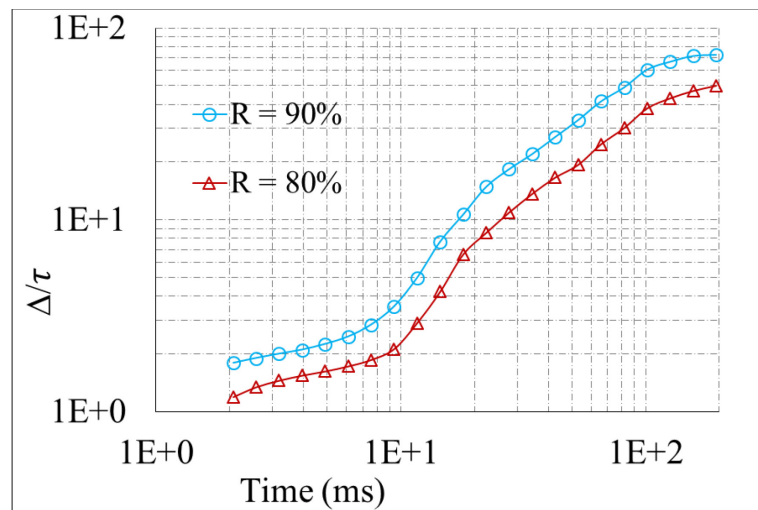


Figure 4.8: Parameter  $\Delta/\tau$  as function of time  $t$  for  $R = 80\%$  and  $90\%$ .

#### 4.4.2 Robustness of the method

The TEM methods are widely used in mineral exploration for targeting metal deposits. However, the response of economic bodies to a TEM system is often very weak compared to the noise of the measurement environment. To examine the applicability of the proposed

method to noisy data, one typical random background noise is added into the theoretical TEM data. We consider the random background noise and the instrumental noise through the whole measurement time. The noise levels are subject to the different instruments and measurement areas. In general, the realistic noise often is at the level of  $10^{0.1} - 10^1$  nT/s, the general dipole moment is greater than  $10^6 \text{Am}^2$  (Allard and Milkereit, 2007; Geotech, 2019). Figure 4.9a illustrates a Gaussian noise (random noise) that is added to the theoretical data generated with different pulse widths. Figures 4.9b to 4.9d and Figure 4.10 illustrate the noisy TEM signal and the signal-to-noise ratio (SNR), respectively.

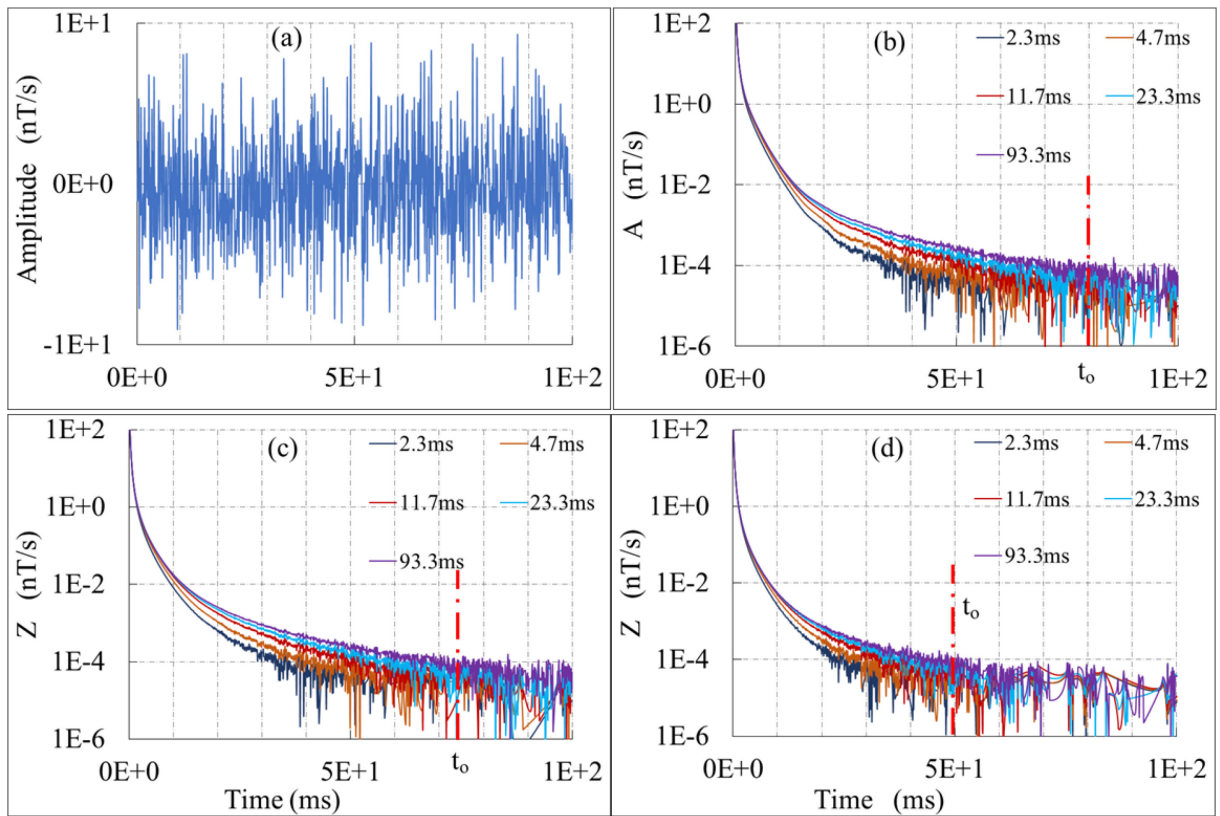


Figure 4.9: (a) Random background noise. (b) surface-borehole TEM noisy signal, (c) ground TEM noisy signal, (d) airborne TEM noisy signal for the model M1.  $t_0$  indicates when the noise is larger than the signal.

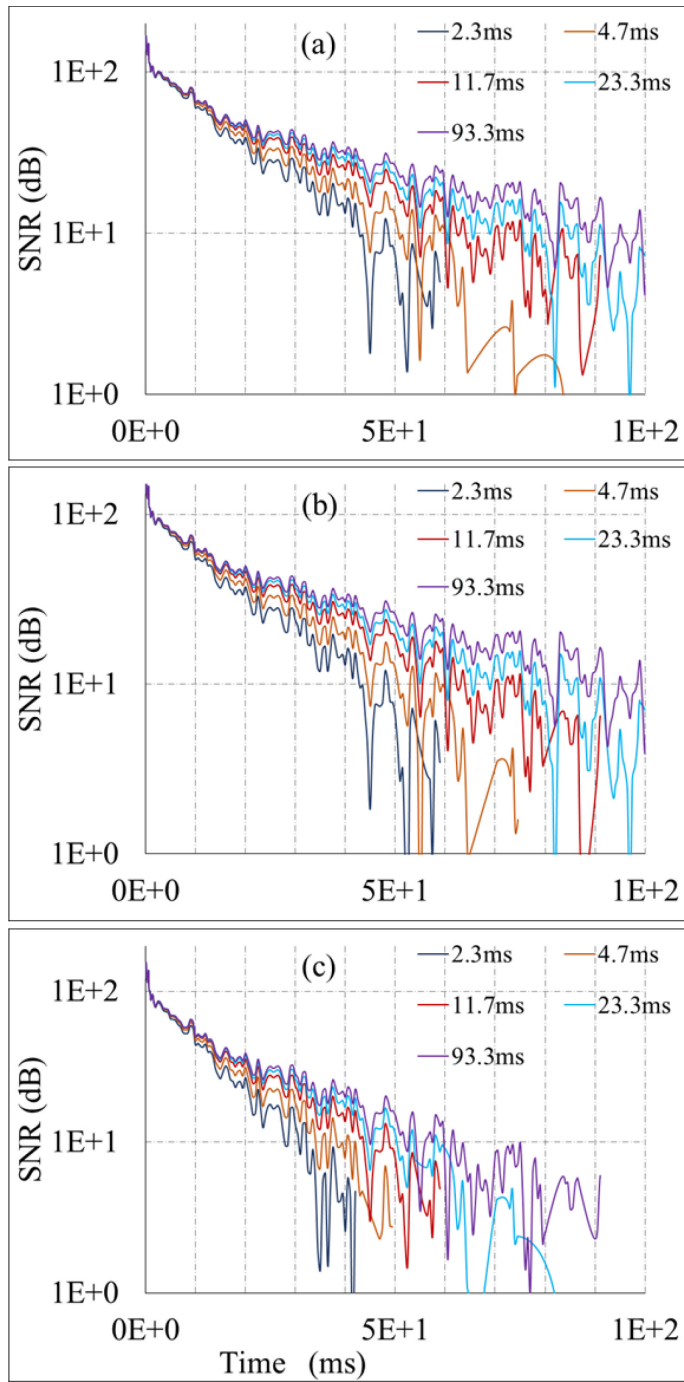


Figure 4.10: Signal-to-noise ratio (SNR) for each channel, surface-borehole TEM (a), ground TEM (b) and airborne TEM (c).

As can be seen in Figure 4.9 and Figure 4.10, as the pulse width increases, the improvements of signal quality and SNR are significant for surface-borehole TEM, ground TEM, and airborne TEM noisy data. Moreover, making a comparison of Figure 4.7 and Figure 4.11, we get consistent conclusions when the noise level is moderate. According to the equation (4.6), this can be simplified as follows,

$$\left\{ \begin{array}{l} R^{theory} = \frac{V(t)}{V_{\Delta_{\infty}}(t)} \\ R^{noisy} = \frac{V(t) + n_l}{V_{\Delta_{\infty}}(t) + n_l} \\ R^{theory} < R^{noisy} \quad (n_l > 0, V(t) < V_{\Delta_{\infty}}(t)) \end{array} \right. \quad (4.12)$$

Where  $R^{theory}$  denotes the optimal pulse width of theoretical data,  $R^{noisy}$  denotes the optimal pulse width of noisy data;  $n_l$  represents the noise level. When the noise level ( $n_l$ ) exceeds the optimal theoretical data ( $V_{\Delta_{\infty}}(t)$ ), the noise will dominate the computation of optimal pulse width, which means we cannot distinguish the target's responses from the noisy data.

Figure 4.11 shows the impact of noise on the estimation of optimal pulse width. The left column of the R-Time represents the signals with a relatively low noise level (1 nT, figures 11a, 11c, 11e) and the signals with a very high noisy level (10 nT) are on the right column (figures 11b, 11d, 11f). As can be seen, this method is valid until the noise exceeds the signal level; and the time  $t_0$  appears later for bigger pulse width. For the same noise level, it makes more impact on airborne signals than the ground and borehole TEM signals.

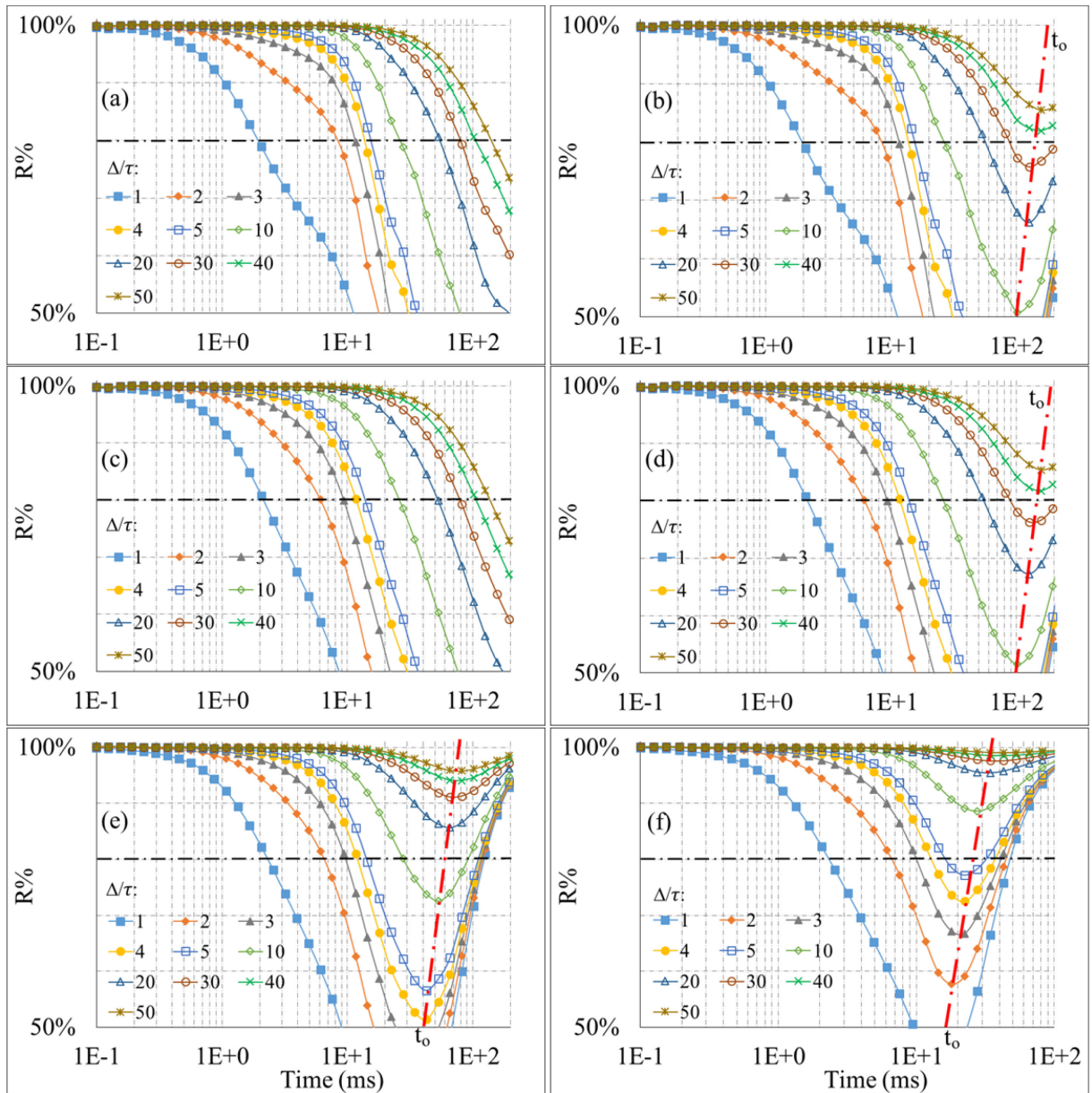


Figure 4.11: Ratio R as the function of time to different values of  $(\Delta/\tau)$  for the noisy data of surface-borehole TEM (a, b), ground TEM (c,d) and airborne TEM (e,f). 1nT/s noisy level in (a, c, e), 10nT/s noisy level in (b, d, f). Model M1 is used for generating theoretical data.

$t_0$  indicates when the noise level is larger than the signal.

## 4.5 Conclusions

The ratio (R) of the induced voltage by a finite-width pulse to that of the infinite-width pulse highly depends on the pulse width, the target time constant and the measurement time. For a specific time window, the value of R increases as increasing the ratio ( $\Delta/\tau$ ) of the pulse width to the target time constant, and the target signal is enhanced. For a specific pulse width, as the measurement time increases, the ratio R decreases as the exponential function, indicating the signal quality decreases. Therefore, it is important to estimate the optimal pulse width first, in order to maximize the efficiency of the TEM survey. For the measurement system design, since the pulse width and off-time are dependent on the base frequency and duty cycle, a large range of the pulse width and off-time would be favorable.

We found an approximate relationship between  $\Delta/\tau$  and the measurement time for  $R = 80\%$  or higher. The parameter  $\Delta/\tau$  changes approximately as the linear function of the time for a specific value of R. This makes that optimal pulse widths can be designed for different off-times to maximize the efficiency of TEM measurement in the field. However, if the TEM survey is conducted in a highly noisy environment (in urban environments, near powerlines, etc.), denoising is necessary before estimating the optimal pulse width.

As indicated the linear relationship between  $\Delta/\tau$  and t is not satisfied when the measurement time (t) is very small or very big. Therefore, a more general functional relationship between the pulse width, the target time constant and the measurement time is necessary for the future.

## CHAPTER 5

### 3D GAUSS-NEWTON INVERSION OF SURFACE-BOREHOLE TEM DATA

#### 5.1 Introduction

The surface-borehole transient electromagnetic (BHTEM in brief) system consists of a transmitter loop carrying a time-varying current on the surface, and an inductive receiver moving along the boreholes to measure the magnetic field  $\mathbf{B}$  and the time rate of change  $d\mathbf{B}/dt$  of the induced magnetic field. As a large transmitter loop is used at the ground surface, the surface-borehole TEM system has a higher source magnetic moment compared with the airborne EM. In addition, the receiver can reach targets at great depth through the drill hole, and lower noise level compared with the ground and airborne EM. That makes the surface-borehole TEM highly efficient in assessing deep mineral exploration.

In the past few decades, significant works improving TEM data interpretation have been done from 3D forward modeling using ribbon plates, sphere, prism models (Dyck, 1981; Dyck and West, 1984; Lamontagne, 2007); equivalent current filament model (Barnett, 1984; Duncan, 1987) within a homogeneously half space or layered structure. Ren et al. (2018) used the AEM volume of influence to reduce the cells, and also only the secondary field is considered (field-separation method), the forward modeling and Jacobian calculations are very fast. Mogilatov et al. (2019) developed the 3D tomographic inversion in which the forward problem is based on Born approximation.

Some software of 3D inversion in a complex geological environment has been developed. Some of them are for magnetotelluric (MT), frequency- and time-domain controlled source

(CSEM) data interpretation (ModEM3D: Egbert and Kelbert, 2012; GEM3D: Liu et al., 2019). For the time domain, VPem3D (Fullagar et al., 2016) uses magnetic dipole for each cell and converts dB/dt or B-field TEM decays to resistive limits; EH3DTD (Napier, 2007) and SimPEG (Oldenburg et al., 2018) decompose the electric field into electromagnetic potentials at each cell center. Our 3D inversion method also uses electromagnetic potential, but it is different from others by adding control techniques on the conductivity model through the inversion process. Recently, Luan et al. (2020) proposed the multinary inversion for ground-wire source TEM data, which better recovers the physical properties and the boundaries of the exploration targets. Yang et al. (2020) projected the time-domain data into the frequency domain using the transformation matrix of sine or cosine transform, and then, to do the frequency-domain EM inversion directly and effectively instead of time-domain EM inversion.

From the numerical calculation point of view, 3D inversion of TEM data is an optimization problem with substantial storage requirements and computation time due to the computation of the Jacobian matrix and (or) Hessian matrix. Usually, the main 3D EM inversions are the iterative search schemes based on the ordinary least squares ( $L^2$  norm) and regularization problems (Tikhonov and Arsenin, 1977; Oldenburg and Pratt, 2007). A very large amount of model parameters causes 3D inversion to be underdetermined and unstable, even ill-posed when the sensitivity matrix and its relevant matrix ( $\mathbf{J}, \mathbf{J}^T \mathbf{J}$ ) are singular in the ordinary least squares. Therefore, the constraint ( $\beta$ ) is introduced ( $\mathbf{J}^T \mathbf{J} + \beta \mathbf{I}$ ) to solve a stable search direction, e.g., the Marquardt-Levenberg inversion scheme (Commer, 2003). In order to find stable search directions and reliable model estimates a priori information and regularization are introduced. Many algorithms have been applied to solve the 3D EM regularization

inversion problem. Using the conjugate gradient (Newman and Alumbaugh, 1997; Newman and Boggs, 2004) and non-linear conjugate gradient (Newman, 2000; Commer, 2003; Kelbert, Egbert, and Schultz, 2008; Singh, 2017) algorithms, the inversion can be restarted once the angle of two adjacent gradients is very small. The quasi-linear approximation (Zhdanov and Tartaras, 2002) and localized quasi-linear inversion (Zhdanov and Chernyavskiy, 2004; Cox and Zhdanov, 2008; Cox, Wilson, and Zhdanov, 2010 and 2012) are based on the regularized conjugate gradient algorithms, which provide fast target imaging based on the assumption that the anomalous field within the inhomogeneous domain is linearly proportional to the background field. The Gauss-Newton method (Haber et al., 2004; Napier, 2007; Liu and Yin, 2016; Dehiya et al., 2017), in which only the first-order derivative in the Hessian matrix is considered can reduce the storage requirements. The Quasi-Newton method (Haber 2005; Haber and Oldenburg, 2007; Napier, 2007; Egbert and Kelbert, 2012; Kelbert et al., 2014), and limited-memory QN method (Avdeev and Avdeeva, 2009) only calculate the gradient of data misfit, and the correction vectors are introduced to avoid calculating the full Hessian matrix directly, thus reducing the storage requirements. The resistive limit inversion of steepest descent method based on TEM moment approximation (Fullagar et al., 2014, 2015, and 2016), introduced the TEM quasi-magnetic problem to generate resistive limit data rapidly. Moreover, in order to overcome the computation cost in 3D EM inversion, parallel computation has been introduced (Newman and Alumbaugh, 1997; Commer, 2004; Grayver et al., 2013; Kelbert et al., 2014; Yang et al., 2014; Cuma et al., 2016; Liu et al., 2016). All these different inversion algorithms share many common elements, e.g. data types, model parameterization, derivative calculation, etc., therefore, Egbert and Kelbert (2012) and Kelbert et al. (2014) developed a general mathematical framework for EM inverse problem to provide more efficient inversion algorithms.

For the 3D TEM inversion, an available and fast method is to avoid the explicit computation and storage of sensitivity matrix, only the products of (Jacobian) matrices and vectors are considered in order to save the computation cost in the conjugate gradient, non-linear conjugate gradient, and Quasi-Newton methods (Rodi and Mackie, 2001, Avdeev, 2005; Miensopust, 2013). However, for the time-domain EM data via time-frequency transformation from the frequency domain, the EM responses and sensitivity matrices are calculated explicitly in the frequency domain and transformed into the time domain. As we know, two challenges, computation cost and interpretation of non-uniqueness, limit the interpretation of field data. One of the methods is to introduce the adaptive cross approximation (ACA) technique to compress the Jacobian matrix at every frequency (Li, 2011), in which the Jacobian matrix is converted into the product of two rectangular matrices (for details see Bebendorf, 2000). Another way to significantly decrease the number of unknowns is the rational Krylov subspace reduction (RKSR) (Boerner et al., 2008; Druskin et al., 2009; Zaslavsky, 2013), in which the TEM Maxwell system is projected onto the rational Krylov subspace. Considering the computation cost we will introduce the Gauss-Newton method to EM inversion because of rapid convergence by computing an approximate Hessian matrix. However, the sensitivity matrix still has a large computation requirement as the field data and the number of unknowns increase. Therefore, in our study, we propose a strategy for modifying and improving the predicted model during the inversion process, in which using isosurface delineates anomalous areas based on the resistivity distribution, neighborhood search and 3D trace envelope are used to outline main anomalous areas and remove false targets. The forward solver is based on the edge-based finite element method

in the frequency domain, and the response is transformed into the time domain. Some synthetic and field case studies illustrate the performance of the new inversion method.

In this research, the framework is that first is to briefly introduce the basic theory of the TEM data inversion and Gauss-Newton optimization, and then we explain the strategy used to improve the model resolution of inversion. Finally, some synthetic and field case studies illustrate the performance of the new inversion method.

## **5.2 Basic theory and improvement**

### **5.2.1 Governing equations**

The surface-borehole TEM method uses an EM transmitter source on the surface and a receiver down in the borehole. The transmitter source could be a closed-loop source or a long wire source with an impulse voltage or AC power supply (Figure 5.1). Using the Schelkunoff potentials, the magnetic vector potential  $\mathbf{A}$  is decomposed into the primary potential (background)  $\mathbf{A}^P$  and the secondary potential  $\mathbf{A}^S$  (Nabighian, 1988; Stalnaker et al., 2006). The electric source generates  $\mathbf{A}^P$  which is calculated in the homogeneous half-space with a certain conductivity ( $\sigma_p$  background conductivity). The secondary potential  $\mathbf{A}^S$  exists only if there is a conductor responding to the induction of the primary electromagnetic field and  $\sigma_s$  is non-zero.

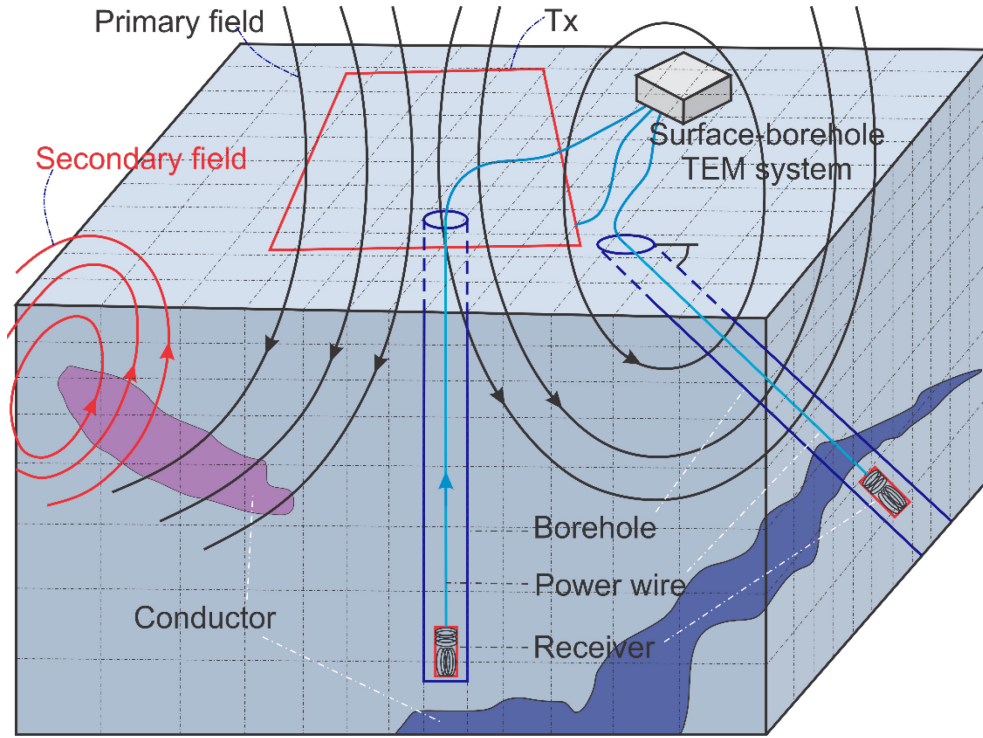


Figure 5.1: BHTEM system in a discretized 3D space

Using the vector theory and Lorentz gauge, the relation between the primary and the secondary vector potential in the frequency domain is defined by the following second-order partial differential equation:

$$\nabla^2 \mathbf{A}^S - i\omega\mu_0\sigma\mathbf{A}^S = i\omega\mu_0\sigma_s\mathbf{A}^P \quad (5.1)$$

Where  $i = \sqrt{-1}$ ,  $\sigma_s = \sigma - \sigma_p$  is the difference between the conductivity distribution ( $\sigma$ ) of anomalies and the background distribution ( $\sigma_p$ ). Equation 5.1 is the governing equation for EM field modeling. The source is introduced in terms of primary EM potential that is known to the problem with background conductivity.

For the simulation of secondary potential  $\mathbf{A}^S$  in this algorithm, the edge-based finite element method is used to discretize Equation 5.1, the final equations system is expressed as,

$$\mathbf{K}\mathbf{A}^S = \mathbf{b} \quad (5.2)$$

$$\mathbf{H}^S = \nabla \times \mathbf{A}^S \quad (5.3)$$

The matrix ( $\mathbf{K}$ ) can be solved using the conjugate gradient-like (CG-like) solver with pre-conditioning and scaling. Then, substituting the result (the secondary magnetic potential) into Equation 5.3, one can get the magnetic and electric fields in the frequency domain. The approximation of the numerical differentiation in Equation 5.3 causes an inevitable loss of accuracy. To address this issue, Raiche et al. (2003) used Green's function operators and volume integral to reduce the error in 3D numerical modeling. As the EM forward modeling is deployed in the frequency domain, the result is then converted from the frequency domain to the time domain by using time-frequency transformation. For the TEM forward modeling, the computer code Loki (Raiche et al., 2003) is used. This section is generalized as the basic EM theory from a previous paper Liu et al. (2020).

### 5.2.2 Regularized Gauss-Newton method

For an inversion in 3D space (Figure 5.1), the number of model cells usually is much larger than the measured data set or survey stations. Therefore, it is an ill-posed inverse problem, which means solving the underdetermined problem (variables are more than the number of equations). Besides, the noise contamination in data can cause the numerical instability of the inverse calculation, which also leads to false anomalies. To solve this problem, the general way is to improve the objective function by adding a constraining function, which is called regularization (Tikhonov and Arsenin, 1977; Aster et al., 2011; Oldenburg and Pratt,

2007). The Regularized Inversion Algorithm is therefore adapted in our Surface-Borehole EM inversion, which seeks to minimize the penalty function:

$$\Phi(\mathbf{m}) = \Phi_d(\mathbf{m}) + \lambda \Phi_m(\mathbf{m}) \rightarrow \min \quad (5.4)$$

Where,  $\Phi$  is the total objective function,  $\Phi_d(\mathbf{m})$  is the objective function of measured data or the misfit between the predicted and field data,  $\Phi_m(\mathbf{m})$  is the a priori constrained model objective function or stabilizing function,  $\mathbf{m}$  is the M-dimensional vector of the model parameters, and  $\lambda$  is the regularization parameter for controlling their contributions. Without the second term, the penalty function is a least-squares problem that is consistent with the inverse probability problem in which the data set can be modeled with the Gaussian distribution (Menke, 1989).

The data misfit  $\Phi_d(\mathbf{m})$  and stabilizing function  $\Phi_m(\mathbf{m})$  are defined as below:

$$\left\{ \begin{array}{l} \Phi_d(\mathbf{m}) = (\mathbf{W}_d \Delta \mathbf{d})^T (\mathbf{W}_d \Delta \mathbf{d}) = (\mathbf{W}_d (\mathbf{d}_{obs} - \mathbf{G}(\mathbf{m})))^T (\mathbf{W}_d (\mathbf{d}_{obs} - \mathbf{G}(\mathbf{m}))) \\ \quad = (\mathbf{d}_{obs} - \mathbf{G}(\mathbf{m}))^T \mathbf{C}_d^{-1} (\mathbf{d}_{obs} - \mathbf{G}(\mathbf{m})) \\ \mathbf{C}_d^{-1} = \mathbf{W}_d^T \mathbf{W}_d \end{array} \right. \quad (5.5)$$

$$\left\{ \begin{array}{l} \Phi_m(\mathbf{m}) = (\mathbf{W}_m (\mathbf{m} - \mathbf{m}_0))^T (\mathbf{W}_m (\mathbf{m} - \mathbf{m}_0)) \\ \quad = (\mathbf{m} - \mathbf{m}_0)^T \mathbf{C}_m^{-1} (\mathbf{m} - \mathbf{m}_0) \\ \mathbf{C}_m^{-1} = \mathbf{W}_m^T \mathbf{W}_m \end{array} \right. \quad (5.6)$$

Where  $\mathbf{G}(\mathbf{m})$  is the forward modeling operator,  $\mathbf{m}_0$  is the M-dimensional initial guess or the model of the previous iteration (M is the number of cells), it is a reference model in the stabilizing function,  $\mathbf{d}_{obs}$  is the N-dimensional field data (N is the number of observations).  $\mathbf{W}_d$  and  $\mathbf{W}_m$  are the data and model weighting matrices (diagonal matrices), respectively,

introduced to reduce (or highlight) the weight of each data and each model parameter, respectively.

To simplify the penalty function, the weight matrices  $\mathbf{C}_d^{-1}$  and  $\mathbf{C}_m^{-1}$  will be eliminated by a simple rescaling of the data and forward mapping ( $\mathbf{C}_d^{-1/2}\mathbf{d}_{obs}$ ,  $\mathbf{C}_d^{-1/2}\mathbf{G}(\mathbf{m})$ ) and the affine linear transformation of the model parameter (data and model parameter transformation), respectively (Egbert and Kelbert, 2012).

$$\begin{cases} \tilde{\mathbf{d}}_{obs} = \mathbf{C}_d^{-1/2}\mathbf{d}_{obs} \\ \tilde{\mathbf{G}}(\mathbf{m}) = \mathbf{C}_d^{-1/2}\mathbf{G}(\mathbf{m}) \end{cases} \quad (5.7)$$

$$\tilde{\mathbf{m}} = \mathbf{C}_m^{-1/2}(\mathbf{m} - \mathbf{m}_0) \quad (5.8)$$

Then, taking the simple scaling on the forward modeling data yields,

$$\tilde{\mathbf{G}}(\tilde{\mathbf{m}}) = \mathbf{C}_d^{-1/2}\mathbf{G}(\mathbf{C}_m^{1/2}\tilde{\mathbf{m}} + \mathbf{m}_0) \quad (5.9)$$

Then, the penalty function Equation 5.4 becomes,

$$\Phi(\tilde{\mathbf{m}}) = (\tilde{\mathbf{d}}_{obs} - \tilde{\mathbf{G}}(\tilde{\mathbf{m}}))^T (\tilde{\mathbf{d}}_{obs} - \tilde{\mathbf{G}}(\tilde{\mathbf{m}})) + \lambda \tilde{\mathbf{m}}^T \tilde{\mathbf{m}} \quad (5.10)$$

In the time domain, the amplitude of TEM responses varies several orders from early time to later time channels. In addition, there are noises that come from the powerline, sferics, and the electronic instrument; if we add the effect of conductive overburden and the attenuation of TEM signal with increasing depth, all channels and TEM field components ( $\mathbf{x}$ ,  $\mathbf{y}$ ,  $\mathbf{z}$ ) are affected. Therefore, weights must be associated for all channels and depths of observation and defined by the diagonal matrix  $\mathbf{C}_d^{-1}$ , in which its  $i^{th}$  element of the main diagonal is defined below (Wilson, Raiche, and Sugeng, 2006; Egbert and Kelbert, 2012):

$$C_{d,i}^{-1} = \frac{2h_i}{\frac{1}{2}(d_{obs,i}^2 + d_{pred,i}^2)} \quad (5.11)$$

Where  $d_{pred,i}$  is the predicted data at the depth of  $h_i$ .

For the model weighting matrix  $C_m^{-1}$ , the elements are the inverse of the square root of the sensitivity for each cell (Zhdanov, 2002). The matrix  $C_m^{-1}$  is constructed using the Frechet derivative (sensitivity) matrix  $F$  (Sunwall, Cox, and Zhdanov 2013):

$$C_m^{-1} = \text{diag}(\mathbf{F}^*\mathbf{F})^{1/2} \quad (5.12)$$

The asterisk (\*) denotes the conjugate transpose. Besides, the model-weighting matrix can be constructed with the first-order derivative. Also, the weight matrices  $C_d^{-1}$  and  $C_m^{-1}$  can be the a priori covariance matrices for the data and model respectively (Snieder and Trampert, 1999; Egbert and Kelbert, 2012).

In the 1D EM inversion case, the optimal regularization parameter  $\lambda$  can be determined by testing several values (Avdeeva and Avdeev, 2006). However, in 3D EM inversion, it is impossible because of the large computing time. Therefore, adaptive schemes were introduced (Haber et al. 2000; Abubakar et al. 2008) by assigning an initial value to the regularization parameter ( $\lambda$ ) and then reducing it gradually.

Several approaches were used to minimize the penalty function (Equation 5.10), such as the minimization of the roughness in resistivity inversion (Constable et al., 1987), searching for the steepest descent by gradient or searching for conjugated steepest direction in diverse

geophysical data inversions (Newton or quasi-Newton methods, classical or Gauss-Newton (GN) with the conjugate gradient methods, gradient-based nonlinear conjugate gradient (NLCG)) (Siripunvaraporn, 2012; Liu and Yin, 2016). The Gauss-Newton method is used in the present study for saving computation memory because in the Hessian matrix second-order derivatives of the penalty function are neglected and only first-order derivatives of the penalty function, the product of two Jacobian matrices, are preserved.

Let  $\mathbf{m}_k$  be the model parameter at the  $k^{\text{th}}$  iteration and the vector  $\tilde{\mathbf{r}}_k = \tilde{\mathbf{d}}_{obs} - \tilde{\mathbf{G}}(\tilde{\mathbf{m}})$ , and neglecting the second-order derivatives in the Hessian matrix, for the penalty function (Equation 5.10), its Taylor series have the form (Madsen, 2004; Egbert and Kelbert, 2012),

$$\begin{aligned} \Phi(\tilde{\mathbf{m}}_{k+1}) &= \Phi(\tilde{\mathbf{m}}_k) + \Delta\tilde{\mathbf{m}}^T \tilde{\mathbf{g}} + \Delta\tilde{\mathbf{m}}^T \tilde{\mathbf{H}} \Delta\tilde{\mathbf{m}} + O(\|\Delta\tilde{\mathbf{m}}\|^3) \\ \left\{ \begin{aligned} \tilde{\mathbf{g}}|_{\tilde{\mathbf{m}}=\tilde{\mathbf{m}}_k} &= -\frac{\partial\tilde{\mathbf{G}}(\tilde{\mathbf{m}})^T}{\partial\tilde{\mathbf{m}}} \tilde{\mathbf{r}}_k + \lambda\tilde{\mathbf{m}}_k \\ \tilde{\mathbf{H}}|_{\tilde{\mathbf{m}}=\tilde{\mathbf{m}}_k} &= -\frac{\partial}{\partial\tilde{\mathbf{m}}} \left( \frac{\partial\tilde{\mathbf{G}}(\tilde{\mathbf{m}})^T}{\partial\tilde{\mathbf{m}}} \right) \tilde{\mathbf{r}}_k + \frac{\partial\tilde{\mathbf{G}}(\tilde{\mathbf{m}})^T}{\partial\tilde{\mathbf{m}}} \frac{\partial\tilde{\mathbf{G}}(\tilde{\mathbf{m}})}{\partial\tilde{\mathbf{m}}} + \lambda\mathbf{I} \end{aligned} \right. \end{aligned} \quad (5.13)$$

In which  $\mathbf{I}$  is the identity matrix,  $\tilde{\mathbf{g}}$  and  $\tilde{\mathbf{H}}$  are the gradient vector and the Hessian matrix of the penalty function respectively, at the  $k^{\text{th}}$  iteration  $\tilde{\mathbf{m}}_k$ ,  $\tilde{\mathbf{J}}$  is the  $N \times M$  dimensional sensitivity matrix in the time domain. Let  $\tilde{\mathbf{J}} = \partial\tilde{\mathbf{G}}(\tilde{\mathbf{m}})/\partial\tilde{\mathbf{m}}$ , and omitting the second-order derivatives in Hessian matrix, yields,

$$\left\{ \begin{aligned} \tilde{\mathbf{g}}|_{\tilde{\mathbf{m}}=\tilde{\mathbf{m}}_k} &= -\tilde{\mathbf{J}}^T \tilde{\mathbf{r}}_k + \lambda\tilde{\mathbf{m}}_k \\ \tilde{\mathbf{H}}|_{\tilde{\mathbf{m}}=\tilde{\mathbf{m}}_k} &= \tilde{\mathbf{J}}^T \tilde{\mathbf{J}} + \lambda\mathbf{I} \end{aligned} \right. \quad (5.14)$$

Let the residual  $r_\Phi = \Phi(\tilde{\mathbf{m}}_{k+1}) - \Phi(\tilde{\mathbf{m}}_k)$  equal to zero, and substituting the form, Equation 5.14, of the gradient vector and Hessian matrix into it, yields,

$$(\tilde{\mathbf{J}}^T \tilde{\mathbf{J}} + \lambda \mathbf{I}) \Delta \tilde{\mathbf{m}} = \tilde{\mathbf{J}}^T \tilde{\mathbf{r}}_k - \lambda \tilde{\mathbf{m}}_k \quad (5.15)$$

Taking the differentiation on both sides of equation 5.9, we have,

$$\tilde{\mathbf{J}} = \mathbf{C}_d^{-1/2} \mathbf{J} \mathbf{C}_m^{1/2} \quad (5.16)$$

Here,  $\mathbf{J}$  is the  $N \times M$  dimensional sensitivity matrix in the time domain.

Then, at  $(k+1)^{\text{th}}$  iteration the model parameter is,

$$\tilde{\mathbf{m}}_{k+1} = \tilde{\mathbf{m}}_k + s \Delta \tilde{\mathbf{m}}_k \quad (5.17)$$

Here,  $\Delta \tilde{\mathbf{m}}_k$ , which is estimated by solving equation 5.15 with the Hessian approximation equation 5.14, is updated at the position  $\tilde{\mathbf{m}}_k$  of the  $k^{\text{th}}$  iteration.  $s$  is a damping parameter for stability, ranging from 0 to 1 that can be calculated by linear search (Frandsen et al. 2004; Madsen, 2004; Haber, 2014).

### 5.2.3 Jacobian matrix

A main difficulty in the inverse problem is to compute the sensitivity (or Jacobian) matrix with respect to model parameters. There are three main methods to calculate the sensitivities for the EM inverse problem, including the brute-force or perturbation method, the sensitivity equation, and the adjoint-equation method (McGillivray and Oldenburg, 1990; McGillivray et al., 1994; Farquharson; 1995; Siripunvaraporn, 2012; Sasaki, 2001).

If the number of cells is small enough to solve the forward problem quite quickly, the brute-force or perturbation method is a simple way to create the sensitivity matrix by changing the initial model parameters to solve the forward problem. It is unreasonable for a large number of cells, and inaccurate for small perturbation. For the sensitivity equation method, first

taking differentiation of Maxwell's equation yields the sensitivity problem (McGillivray and Oldenburg, 1990). To calculate the sensitivities using the adjoint-equation method by taking the differentiation of the frequency-domain Maxwell's equations, the adjoint field must be calculated due to the appropriate dipole source, in which a large computation time is needed. In our inversion, based on the Gauss-Newton method, the sensitivity matrix is constructed from the partial derivatives of the vector potential with respect to the model parameters. To derive the sensitivity matrix, let  $\mathbf{A}$  be the predicted total potential field,

$$\mathbf{A} = \mathbf{A}^P + \mathbf{A}^S \quad (5.18)$$

Because the background  $\mathbf{A}^P$  is fixed, its derivative with respect to the model parameters is zero. To simplify the equations, the symbol to present the secondary vector potential is omitted in the following ( $\partial\mathbf{A}/\partial\mathbf{m} = \partial\mathbf{A}^S/\partial\mathbf{m}$ ).

Differentiating both sides of the stiffness matrix equation with respect to the conductivity ( $\mathbf{m}_k$ ) of a cell (Oldenburg, 1990; Sasaki, 1994, 2001; Newman and Alumbaugh, 1997; Newman and Boggs, 2004; Liu and Yin, 2016) yields,

$$\frac{\partial}{\partial m_k}(\mathbf{K}\mathbf{A}) = \frac{\partial \mathbf{b}}{\partial m_k} \quad (5.19)$$

Using the above equation to express  $\partial\mathbf{A}/\partial m_k$  yields,

$$\frac{\partial \mathbf{K}}{\partial m_k} \mathbf{A} + \mathbf{K} \frac{\partial \mathbf{A}}{\partial m_k} = \frac{\partial \mathbf{b}}{\partial m_k} \quad (5.20)$$

Then we have,

$$\frac{\partial \mathbf{A}}{\partial m_k} = \mathbf{K}^{-1} \left( \frac{\partial \mathbf{b}}{\partial m_k} - \frac{\partial \mathbf{K}}{\partial m_k} \mathbf{A} \right) \quad (5.21)$$

Assuming a  $N \times M$  matrix, in the stiffness matrix, only a few elements depend on  $\mathbf{m}_k$ ,

$$\mathbf{G} = \left\{ \frac{\partial \mathbf{b}}{\partial m_1} - \frac{\partial \mathbf{K}}{\partial m_1} \mathbf{A}, \frac{\partial \mathbf{b}}{\partial m_2} - \frac{\partial \mathbf{K}}{\partial m_2} \mathbf{A}, \dots, \frac{\partial \mathbf{b}}{\partial m_M} - \frac{\partial \mathbf{K}}{\partial m_M} \mathbf{A} \right\} \quad (5.22)$$

Then, the sensitivity matrix of vector magnetic potential is as,

$$\mathbf{J}_A = \left\{ \frac{\partial \mathbf{A}}{\partial m_k} \right\} = \mathbf{K}^{-1} \mathbf{G} \quad (5.23)$$

The final equations system is expressed as,

$$\mathbf{K} \mathbf{J}_A = \mathbf{G} \quad (5.24)$$

Equation 5.24 is similar to the stiffness matrix equations in the forward problem. The matrix  $\mathbf{K}$  and the vector  $\mathbf{b}$  are known. Moreover,  $\mathbf{K}$  is a sparse matrix in which only a part of the elements depends upon  $m_k$ , therefore, we can easily calculate  $\partial \mathbf{K} / \partial m_k$ .  $\mathbf{A}$  is known from the forward modeling. The conjugate gradient method is used to solve equation 5.24 to compute  $\mathbf{J}_A$ . Using reciprocity, only  $N_s \times N_f \times N_r \times 2$  times computations of the large complex matrix equations are executed to get the sensitivity matrix in the frequency domain. Here,  $N_s$  is the number of transmitter loops,  $N_f$  is the number of frequencies,  $N_r$  is the number of receivers. After taking Green's function operators to get the sensitivities of the magnetic field ( $\partial \mathbf{H} / \partial m_k$  in the frequency domain) at the receiver locations, we estimate the sensitivity matrix in the time domain using frequency-time transformation. Although, this method can save much time compared with the perturbation method or difference method, however, the computations of sensitivity matrix always dominate the computer cost and computation time in the present inversion.

## 5.2.4 Improvement in TEM data inversion

Figure 5.2a shows a schematic overview of the present electromagnetic inversion procedure. In general, 3D TEM inversion is time-consuming and leads to non-unique solutions. To address those two challenges, one effective strategy is to set a good initial model, or modifying and updating the predicted model during the inversion process that we proposed in Figure 5.2b and described as follows.

### > Improvement of initial model $\mathbf{m}_0$

Starting from a quick 3D inversion of TEM data with a homogenous half-space initial model. The first inversion yields an initial guess model ( $\mathbf{m}^{\text{pre}}$ ), which contains some anomalous zones. We take the averaging resistivity of the whole guess model as the resistivity of background, denoted as  $\mathbf{m}^b$ , and then using isosurface delineates the anomalous zones of the initial guess model by keeping the anomalous resistivity value of the inversion. Combining with the geological information, using neighborhood search (NS) to define the adjacent anomalous bodies with the same resistivity and form a 3D trace envelope who unites all of them into one anomalous body  $\mathbf{m}^j$  ( $j = 1, 2, \dots, n$ ). The void areas between the adjacent anomalous bodies are filled with their resistivity. Therefore, the updated initial model contains two parts – background and united anomalous areas.

$$\mathbf{m}_0 = \mathbf{m}^b + \sum_{j=1}^n \mathbf{m}^j \quad (5.25)$$

Here,  $n$  denotes the number of united anomalous bodies.

For TEM exploration, the response at one survey station is the comprehensive benefits of the entire medium in the volume of EM influence. Consequently, the model space may contain

many different resistivity areas. The purpose of inversion is to delineate favorable physical models targeting the representative anomalous areas of good conductors. We proposed the following strategies and criteria:

- First, we classify the resistivities and determine the average value for each family based on the scatter plot of resistivity distribution from the preliminary inversion result. For example, as shown in Figure 5.3, there are two classes of resistivities, one has average resistivity of  $3.5 \Omega \cdot \text{m}$  (conductor), and another is high resistive as the background ( $1000 \Omega \cdot \text{m}$ ).
- Using isosurface, the approximate anomalous areas can be defined, as  $C_1$ ,  $C_2$ ,  $F_1$ , and  $F_2$  in Figure 5.4a. The dimensions of the approximate anomalous areas are impacted by resistivity.
- Searching other anomalous areas around one within a certain distance. For example, we define the area around  $C_1$  with the constant distance  $r$ . Any other anomalous area partly or fully included in this area is considered as part of  $C_1$  if they have the same resistivity. Then, they are combined as one main anomalous area.
- Finally, using 3D trace envelope, one can outline the main anomalous areas (Figure 5.4c and 5.4d) as a new initial model for the next iteration of the

inversion. If drilling logs are available, they will be considered and integrated into 3D trace envelope design.

Repeating the operations described above reduces the complexity in the inversion process to guide the inversion toward a plausible geological model.

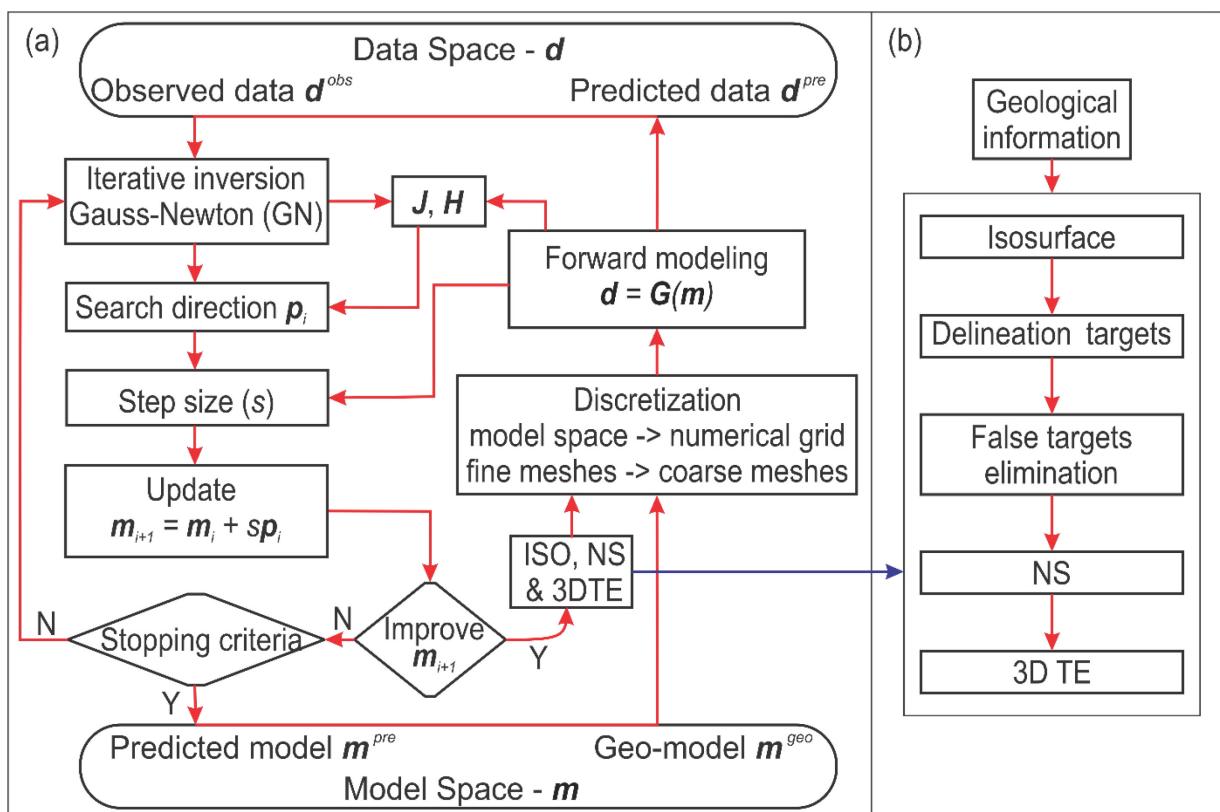


Figure 5.2: (a) Schematic overview of the BHTEM inversion, (b) modification and improvement of the predicted model in the inversion process

➤ Modification of predicted model  $m_k$

In the inversion process, we can modify the predicted model at any iteration. The predicted model  $\mathbf{m}_k$  at  $k^{\text{th}}$  iteration contains the united anomalous bodies  $\mathbf{m}_k^j$  and the background  $\mathbf{m}_k^b$ , then the updated predicted model  $\mathbf{m}_k$  is expressed as below,

$$\mathbf{m}_k = \mathbf{m}_k^b + \sum_{j=1}^n \mathbf{m}_k^j \quad (5.26)$$

As shown in Figure 5.4a and 5.4b, there are four anomalous resistivity zones (C1, C2, F1, F2). Since the distance between C1 and C2 is smaller than their size, they are united together; then, using the 3D trace envelope the whole anomaly area D is delineated (Figure 5.4c and 5.4d).

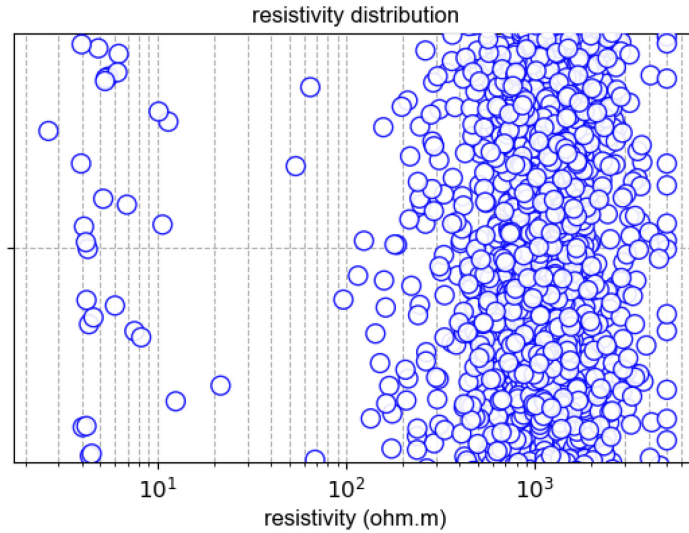


Figure 5.3: Scatter plot of resistivity distribution

➤ False targets elimination

The inversion is non-unique, which means for most cases there are some false anomalous zones. Due to the limits of the inversion space domain and the receivers (field data), some

areas almost do not contribute to the BHTEM responses, which is even more serious for the areas near the edges of the inversion space domain. That may be caused by very small sensitivities and the bad update of model parameters in the inversion, consequently the predicted resistivities are misinterpreted.

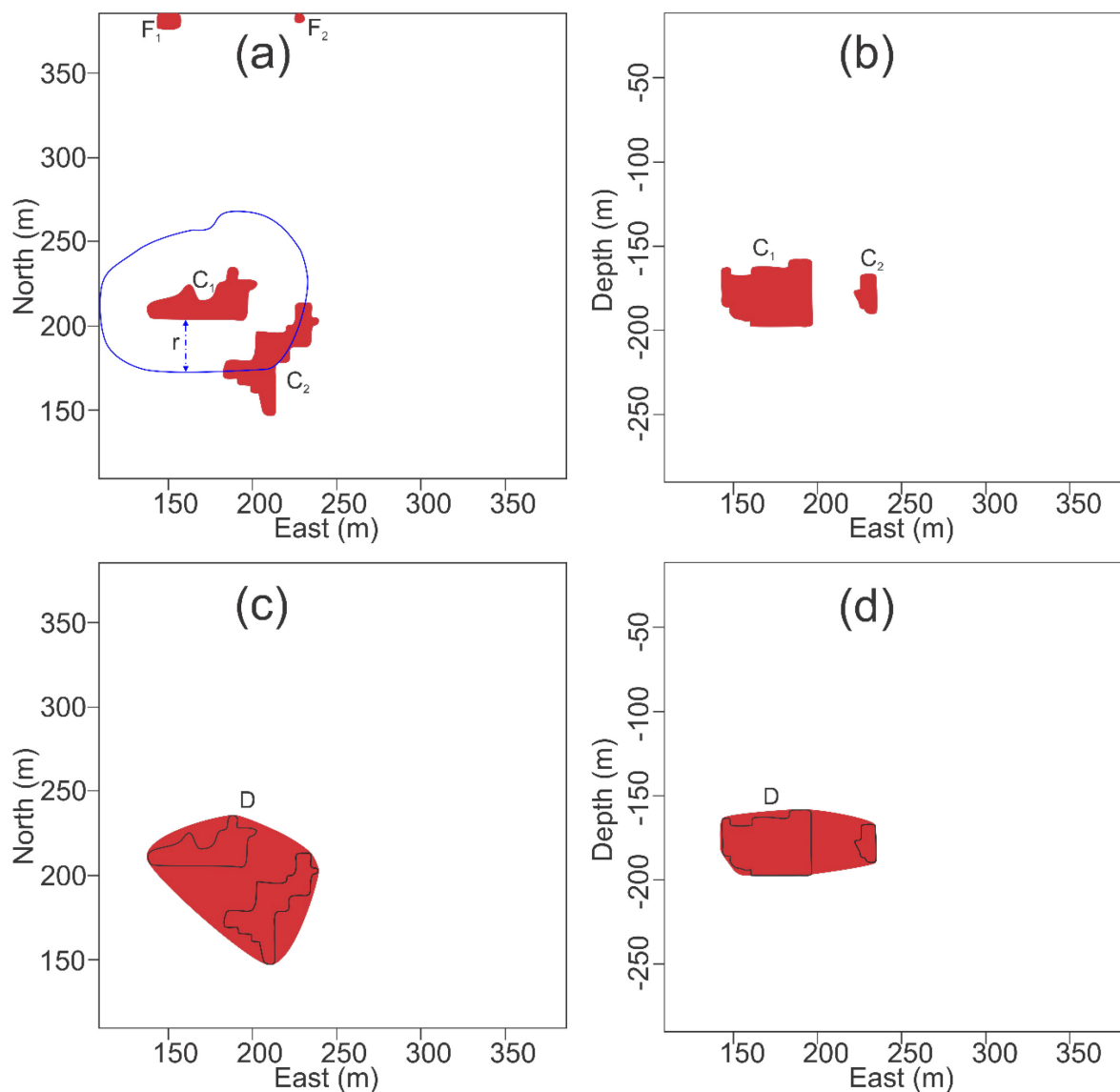


Figure 5.4: General outline map of inversion results, (a) top view, (b) section view. (c) Top view and (d) section view after inversion results are improved with NS, 3D trace envelope, and false targets elimination.  $r$  is the distance to the boundary of  $C_1$ .

In order to eliminate the false targets and ensure that the inversion focus on the interesting ones, we establish the following criteria: 1) Focus on the zones potentially favorable for the mineral exploration, for example, the area of intersecting faults or multiphase intrusions, 2) only considering the high conductivity contrasts and 3) anomalies away from the edges of the inversion space domain. Therefore, small anomalous areas that are far away from the main anomalous area are considered as fake targets. As shown in Figure 5.4a, the areas of low resistivity ( $C_1$  and  $C_2$ ) are considered as good targets; while the small conductive anomalies near the edge ( $F_1$  and  $F_2$ ) are regarded as false targets which may be caused by the boundary effect or low intensity of illumination of surface-borehole TEM data measurement. Based on the above criteria, by defining a moving region with a certain radius, the areas of abnormal resistivity are either combined together or eliminated from updated models (Figure 5.4c, 5.4d).

### **5.3. Applications of Gauss-Newton inversion to modeled data**

#### **5.3.1 Case 1: one conductive prism**

A synthetic model is designed to test the inversion. All the coordinates within the model space are defined by (East, North, Depth), and the size of objects is in meters along three axes ( $x, y, z$ ). The background is a half-space with a uniform resistivity of  $1000 \Omega \cdot m$ . It hosts a conductive prism of  $5 \Omega \cdot m$  (Figure 5.5). The dimension of the prism is  $80m \times 80m \times 40m$ , and its central location at  $(200m, 200m, -160m)$ . Two boreholes start from the surface at  $(200m, 200m)$ ,  $(300m, 200m)$ , respectively. A transmitter loop (Tx) of  $200m \times 200m$ , centered at  $(200m, 200m, 0)$ , generates the primary TEM field with a trapezoidal waveform. The receiver records TEM response every 20m through two boreholes. The on-time and off-time

of the transmitted pulse are 100ms and 1000ms, respectively, and the turn-on and ramp turn-off are 1.5ms and 0.2ms respectively. Figure 5.6 illustrates the forward modeling data for case 1. The TEM response in BH1 is well to define the anomaly, but the response decays quickly even the borehole (BH2) is only 60m away from the conductor.

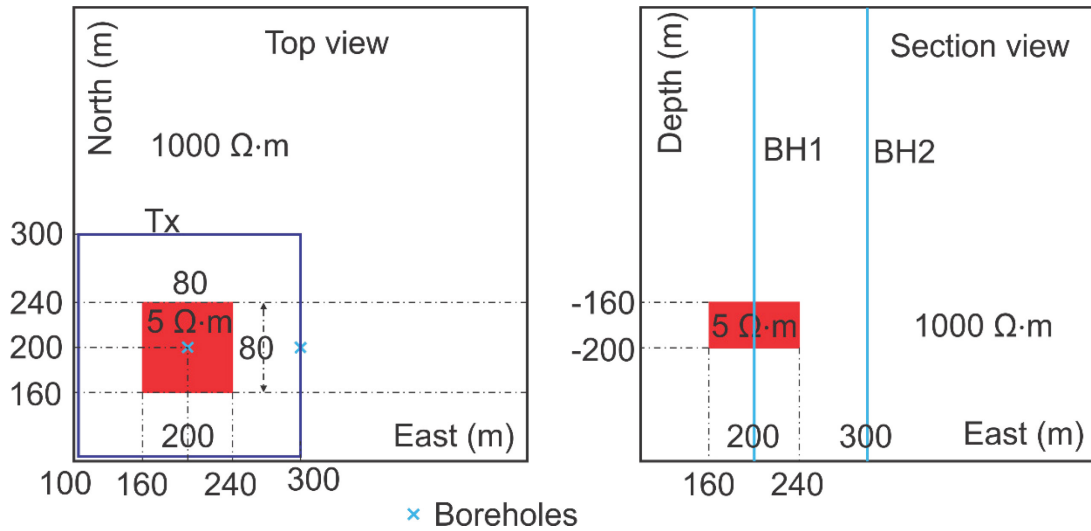


Figure 5.5: Case 1 – a  $5 \Omega \cdot \text{m}$  conductive prism buried in a uniform  $1,000 \Omega \cdot \text{m}$  half-space, two boreholes (BH1 and BH2) are used.

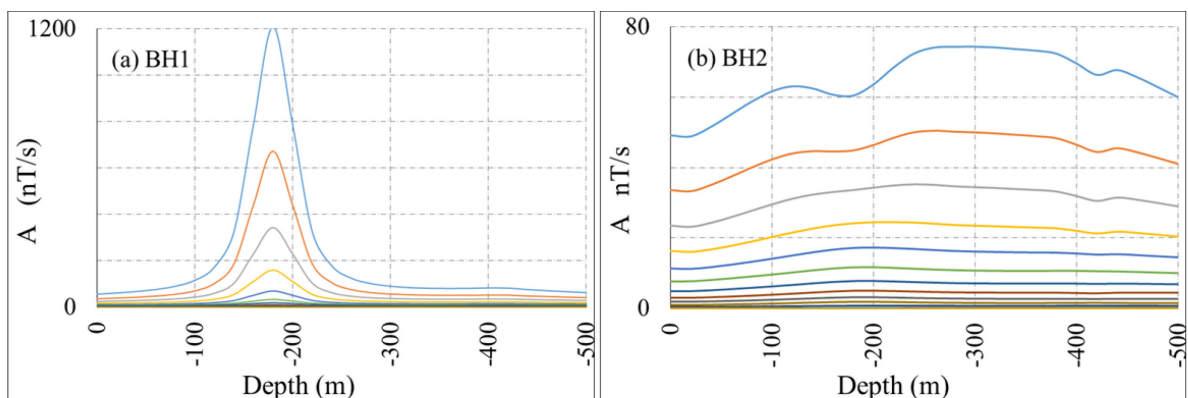


Figure 5.6: Forward modeling data along the boreholes (BH1 and BH2) on case 1

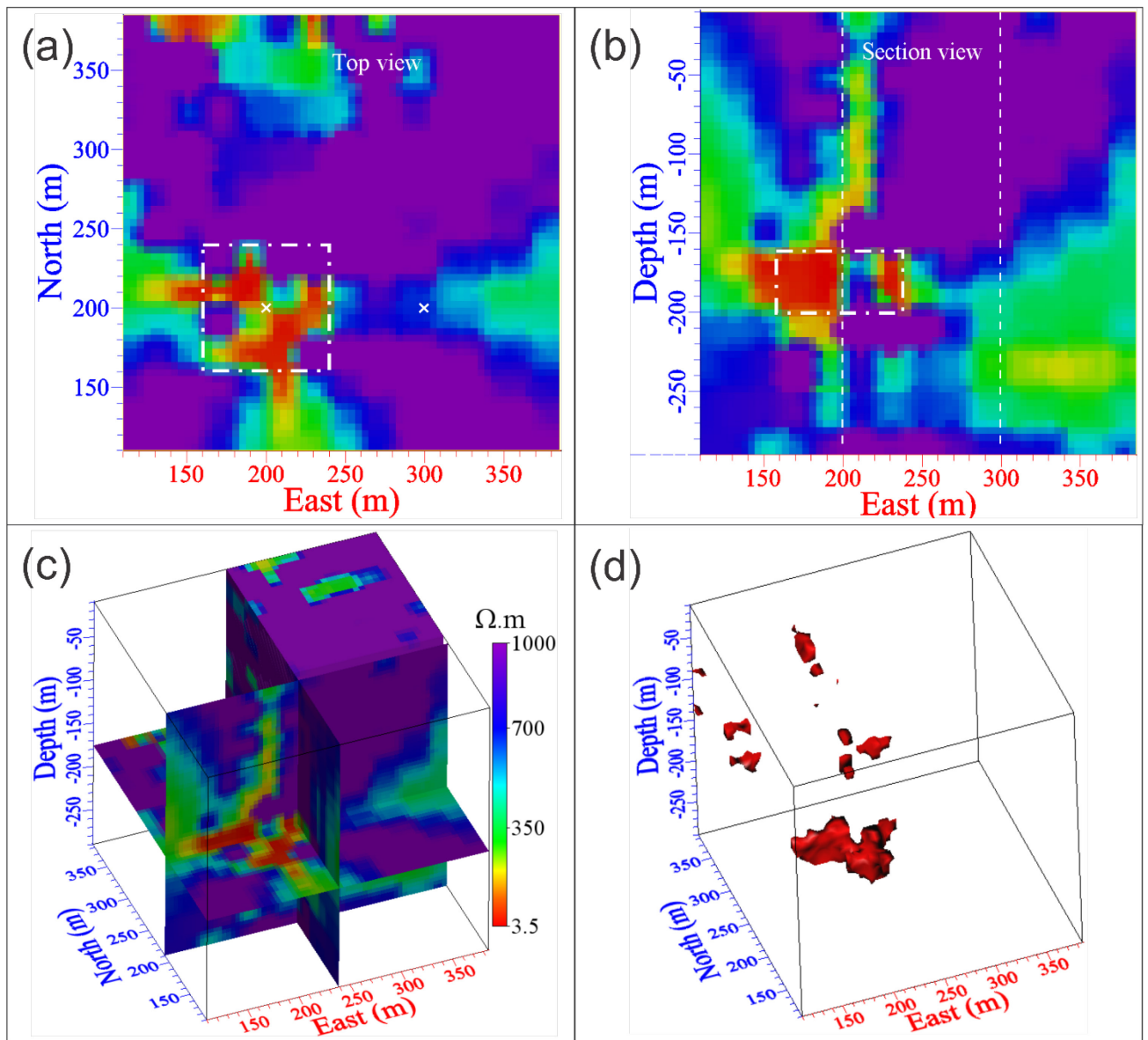


Figure 5.7: Inversion results of case 1 with a uniform  $1000 \Omega \cdot m$  initial model. (a) Top view at  $z = -180$ m, (b) section view at  $y = 210$ m, (c) cross-sections view of the predicted model (a, b and c share the same color bar), and (d) bodies defined by isosurfaces of  $5 \Omega \cdot m$

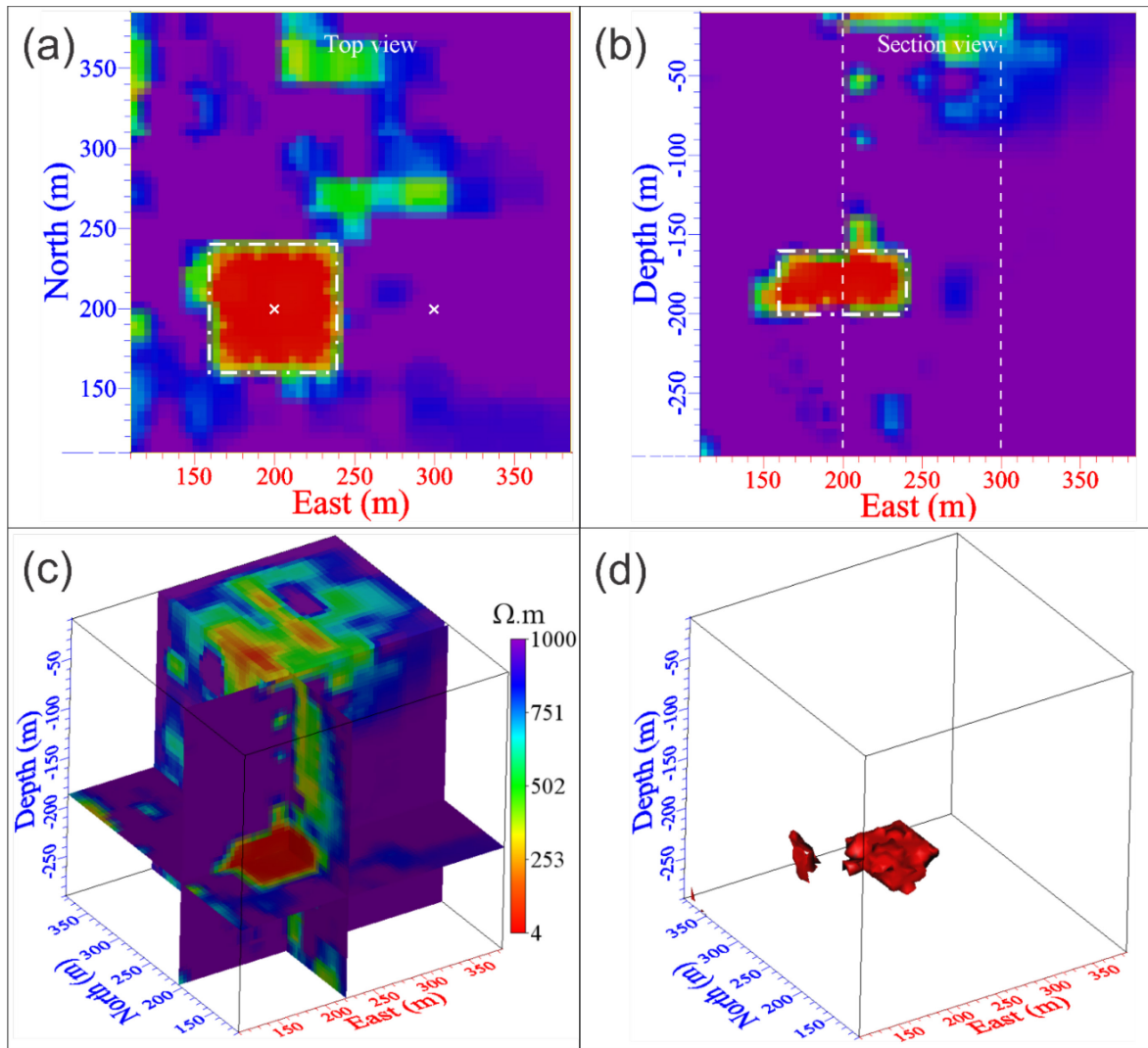


Figure 5.8: Inversion results of case 1 with isosurface, NS, 3D trace envelope and false target elimination. (a) Top view at  $z = -180\text{m}$ , (b) section view at  $y = 210\text{m}$ , (c) cross-sections view of the predicted model (a, b and c share the same color bar), and (d) bodies defined by isosurfaces of  $5 \Omega \cdot \text{m}$

Figure 5.7 shows the inversion results obtained using a uniform half-space of  $1000 \Omega \cdot \text{m}$  as initial and reference models. We note that the recovered low resistivity body is coincident with the model conductive prism; however, its limits are not recovered clearly (Figure 5.7a-5.7b). The prism shows up like two conductive bodies, that could lead to some

misinterpretation of the actual conductive prism. Also, some small false targets are close to the boundary of the model. After the application of isosurface, neighborhood search and 3D trace envelope, the false targets are removed close to the boundary. Not only the conductive prism is very well defined, its geometry and physical properties are well determined (Figure 5.8). Therefore, by modifying and improving the predicted model during the inversion process, we can get good model resolution.

The root-mean-square (RMS) misfits for the inversion are shown in Figure 5.9a. the RMS error decreases very quickly at the beginning of the first inversion start from the uniform half-space. After 20 times iterations, the RMS error has a good decrease and reduces to a low level. Therefore, Figure 5.9b-like inversion process is deployed by reducing the model complexity.

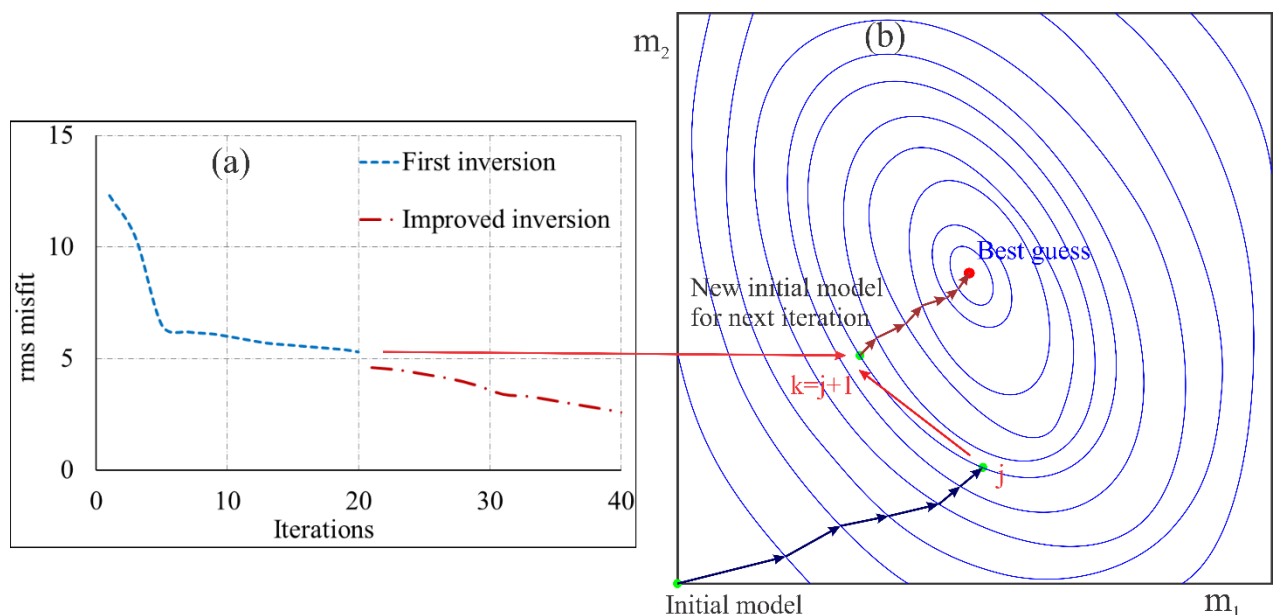


Figure 5.9: (a) Data misfit of 3D inversion for case 1, (b) sketch of imitated inversion process with our strategy

### 5.3.2 Case 2: two conductive prisms

Referring to Figure 5.10, two conductive prisms, having the same dimensions  $80\text{m} \times 80\text{m} \times 40\text{m}$  and the same resistivity of  $5 \Omega \cdot \text{m}$ , are located at  $(180\text{m}, 200\text{m}, -180\text{m})$  and  $(320\text{m}, 200\text{m}, -180\text{m})$ , respectively (central locations) in a uniform half-space with  $1000 \Omega \cdot \text{m}$  resistivity. The central location of the  $200\text{m} \times 200\text{m}$  transmitter loop (Tx) is at  $(250\text{m}, 250\text{m}, 0)$ . Three boreholes are located at  $(180\text{m}, 200\text{m}, 0)$ ,  $(250\text{m}, 200\text{m}, 0)$ , and  $(320\text{m}, 200\text{m}, 0)$ , respectively. The receiver records the A-component of fields at an interval of  $20\text{m}$  through the vertical boreholes.

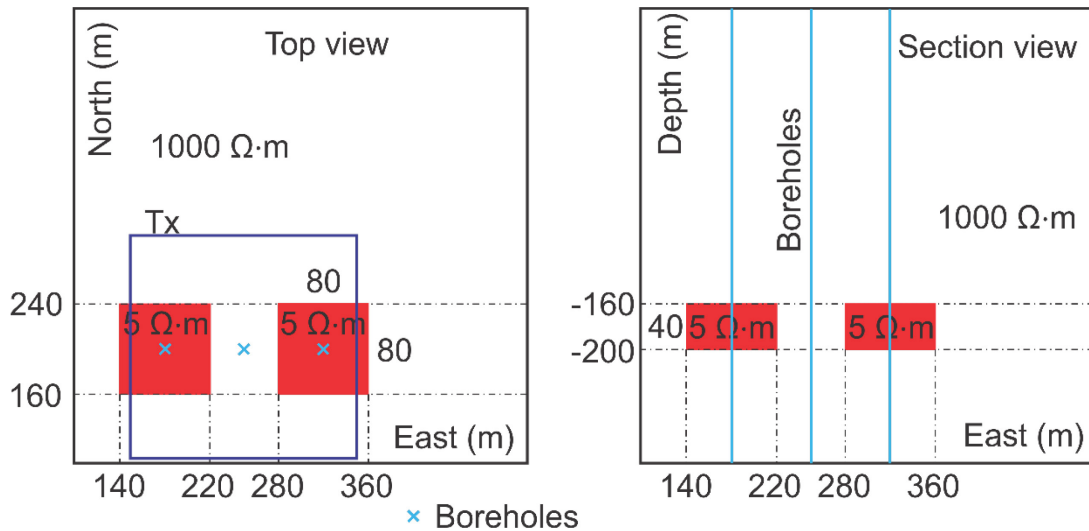


Figure 5.10: Case 2 – two  $5 \Omega \cdot \text{m}$  conductive prisms buried in a uniform  $1000 \Omega \cdot \text{m}$  half-space, three boreholes are used.

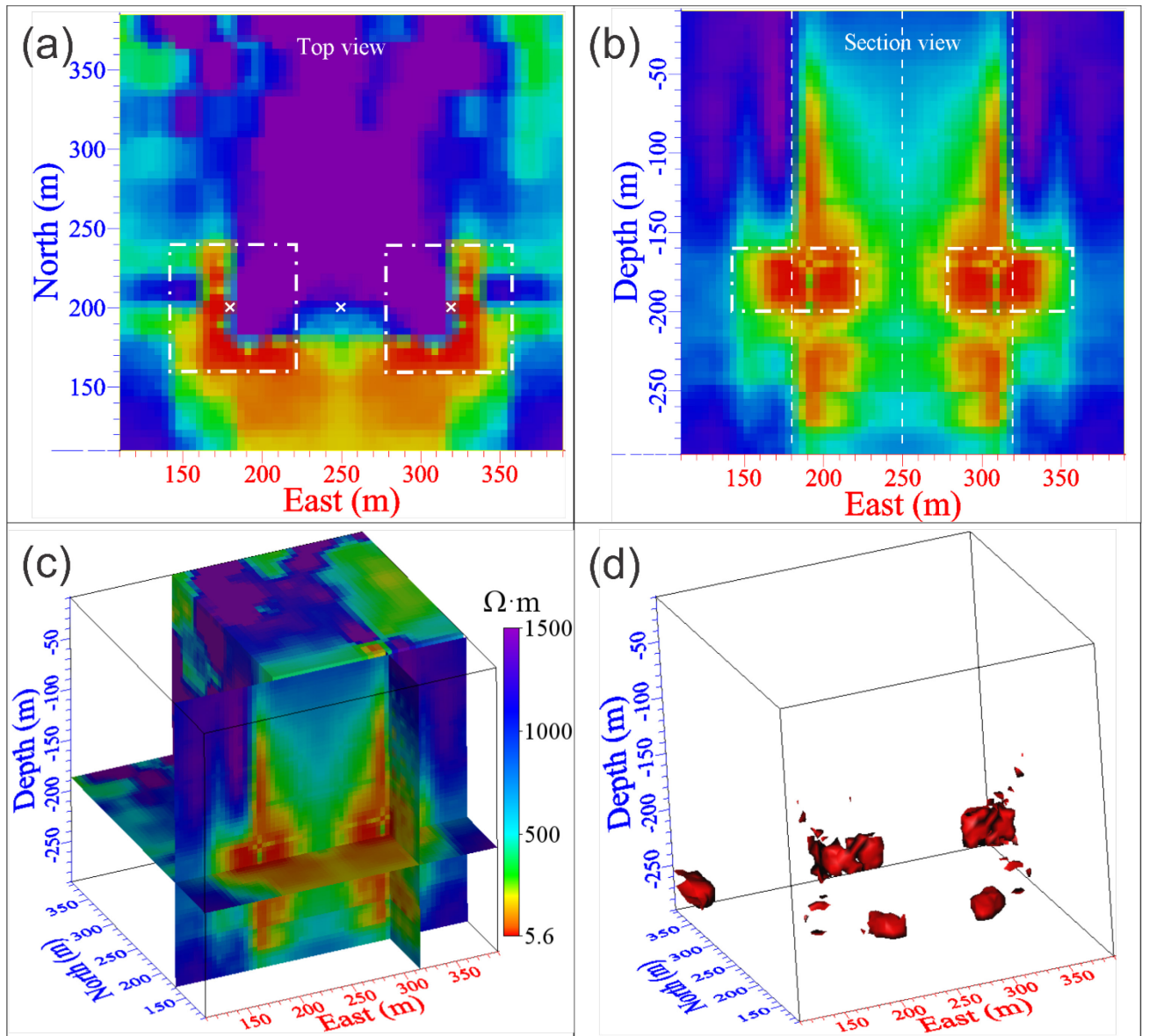


Figure 5.11: Inversion results of case 2 with a uniform  $1000 \Omega \cdot \text{m}$  host rock model. (a) Top view at  $z = -170\text{m}$ , (b) section view at  $y = 180\text{m}$ , (c) cut-away view of the predicted model (a, b and c share the same color bar), and (d) bodies defined by isosurfaces of  $10 \Omega \cdot \text{m}$ .

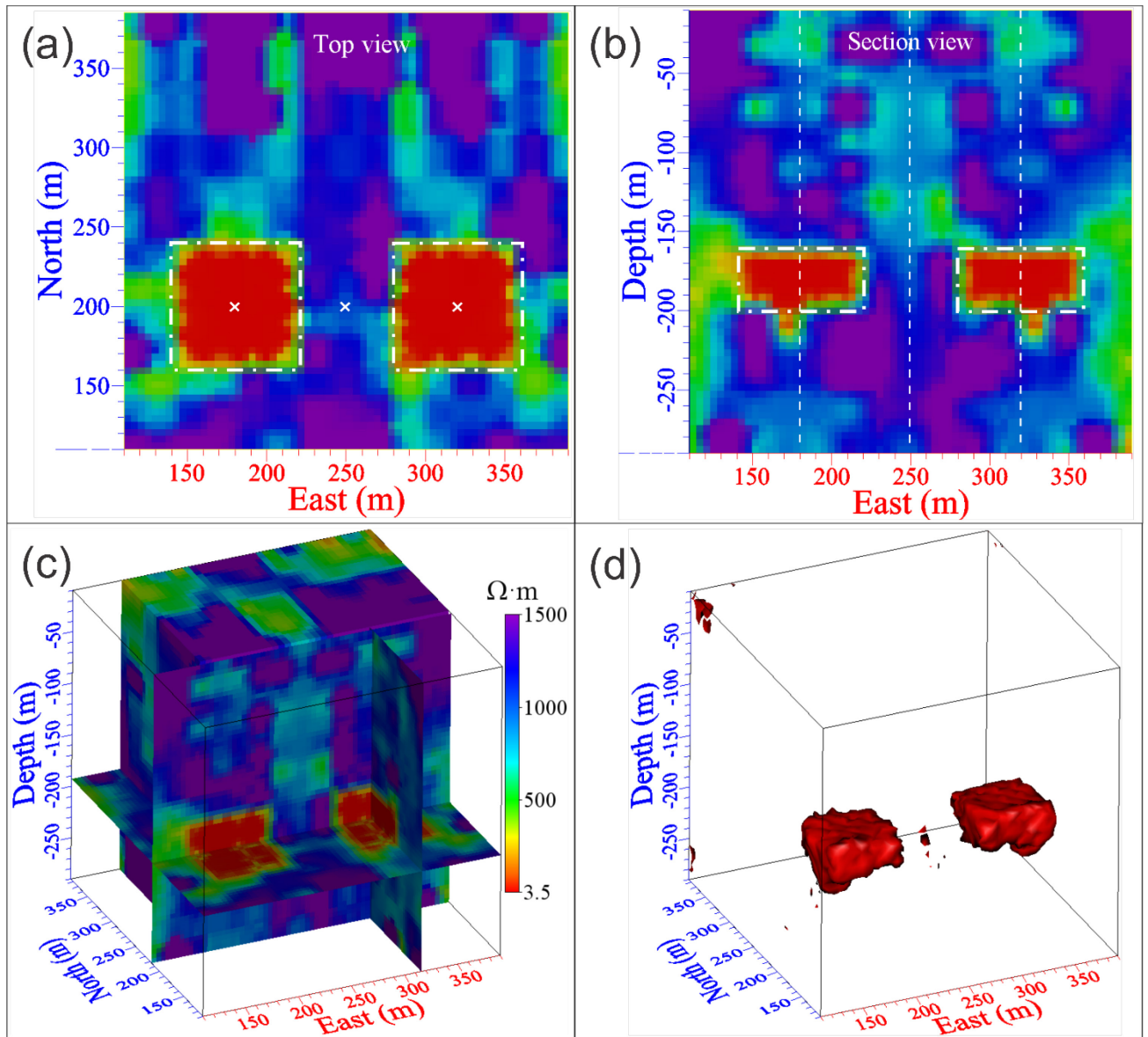


Figure 5.12: Inversion results of case 2 with isosurface, neighborhood search, 3D trace envelope, and false target elimination. (a) Top view at  $z = -170\text{m}$ , (b) section view at  $y = 180\text{m}$ , (c) cut-away view of the predicted model (a, b and c share the same color bar), and (d) interpretation based on the inversion results.

Figure 5.11 shows the inversion results starting from a uniform 1000  $\Omega\cdot\text{m}$  half-space as the initial model. Though the positions of two conductive prisms are well defined, the rapid variations of resistivity near model edges and between the prisms are much higher than in the first case. Figure 5.12 shows the results obtained when the isosurface, neighborhood search, 3D trace envelope, and false target elimination are involved during the inversion process. The improved inversion satisfactorily recovers the positions, sizes, and resistivity distribution of two prisms. The lowest inverted resistivities are 3.5  $\Omega\cdot\text{m}$ , and the average is 5  $\Omega\cdot\text{m}$  in the anomalous areas.

The inversion results of two synthetic data (Case 1 and case 2) have confirmed that if we can trim the anomalies and fill the void areas between the anomalies and upgrade the predicted model during the inversion process, it is possible to estimate the main features of the model.

### **5.3.3 Case study**

The Iso deposit is a volcanogenic massive sulfide (VMS) body in the area of Rouyn-Noranda City, Quebec, Canada (Figure 5.13). Numerous geophysical surveys have been carried out to define its deep extension, including ground and airborne EM, IP, borehole EM, magnetic, and gravity (Fraser, 1974; Telford and Becker, 1979; Cheng et. al., 2006). The Iso VMS deposit is located in a favorable horizon between diorite, rhyolite, andesite/basalt along an east-west direction. Its low resistivity (less than 2  $\Omega\cdot\text{m}$ ) is in contrast with that of volcanic rocks whose resistivities are more than 1,000's of ohm-meter. This is why it was well discovered by airborne EM surveys (INPUT and DIGHEM), followed by ground and borehole EM surveys in 1974.

Table 5.1: Location and geometry for the 14 boreholes in which receiver data were collected

Boreholes	(East, North)	Depth (m)	Dip angle (degree) varied from	Azimuth (degree)
M1	(546, 600)	-100	47.6	0
M7	(367, 500)	-150	44.4 – 56.7	0
M8	(739, 470)	-150	51.0 – 55.5	0
M9	(435, 410)	-200	42.7 – 57.2	0
M11	(555, 490)	-200	65.9 – 73.0	0
M30	(795, 440)	-200	63.0 – 73.0	0
M32	(556, 130)	-450	47.6 – 90.0	0
M45	(435, 290)	-300	32.4 – 61.8	0
M47	(459, 510)	-200	67.3	0
M53	(308, 470)	-120	42.5	0
M71	(646, 330)	-300	49.0 – 62.3	0
M77	(495, 290)	-330	51.5 – 90.0	0
M91-11	(384, 0)	-660	49.6 – 77.0	0
M91-12	(435, 60)	-660	71.0 – 90.0	0

In our inversion, the relative coordinate system is used; the origin is taken at (619,742E; 5,366,000N). A 500m×550m transmitter (Tx) loop and 14 boreholes (Figure 5.13 and Table 5.1) were used to collect the surface-borehole TEM data. The center of the Tx loop is located at (400m, 425m, 0), nine boreholes are located inside the transmitter loop, two boreholes are to the south and three boreholes are to the east side of the Tx loop. The data were collected

at 20m intervals in the borehole for a total of 215 receiver positions; the survey measured the magnetic field time derivative ( $dB/dt$ ) along the axis of the borehole from 0.087ms to 10.564ms (21 channels per receiver position). The inversion results are illustrated in Figure 5.14.

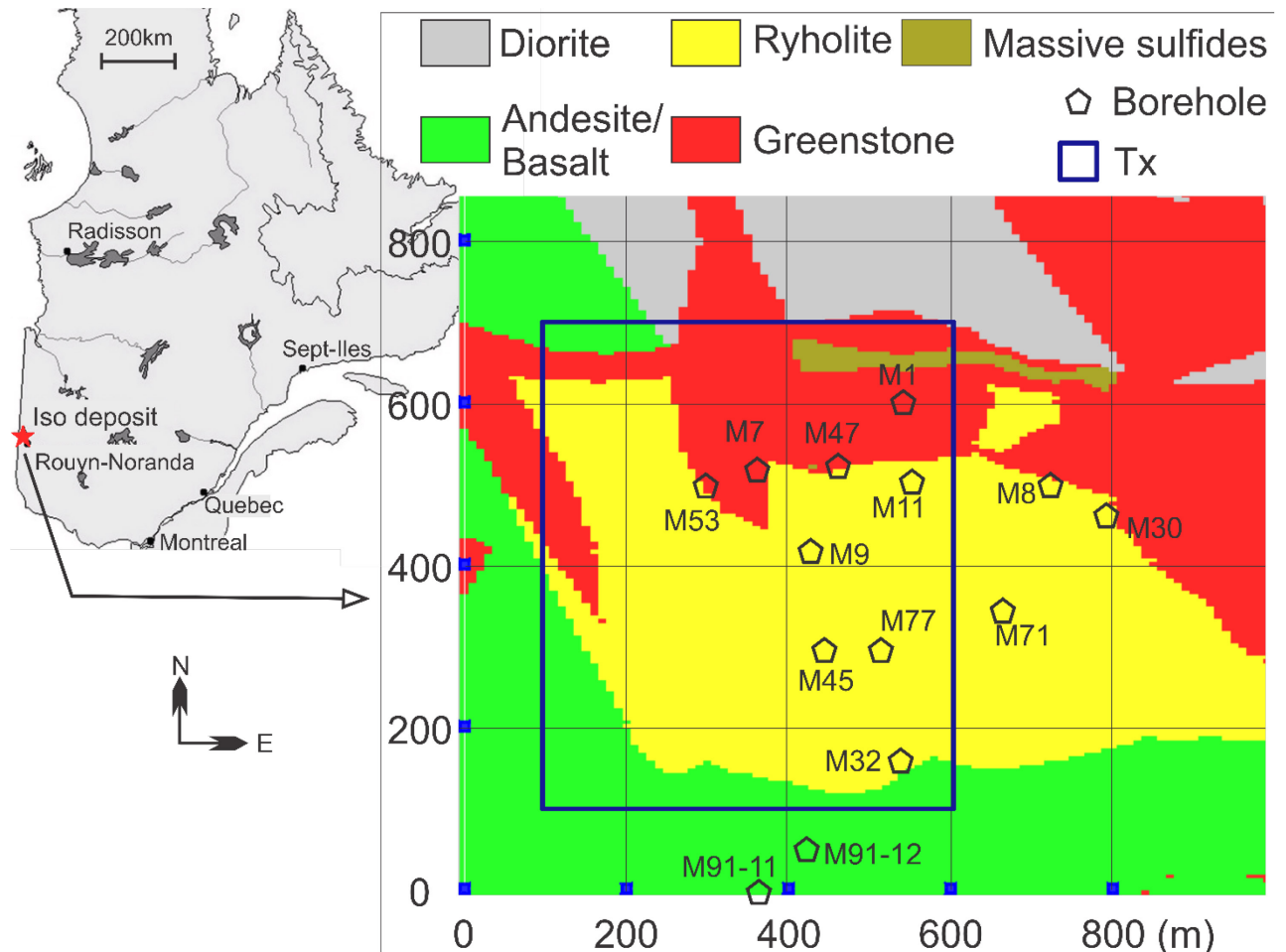


Figure 5.13: Location of the survey area and geology of the Iso area (modified from Cheng et. al., 2006); the configuration of the measurement system is shown. A relative coordinate system in meters is used. One transmitter loop (Tx) is located at (350m, 400m, 0) at the surface, 14 boreholes are around Tx.

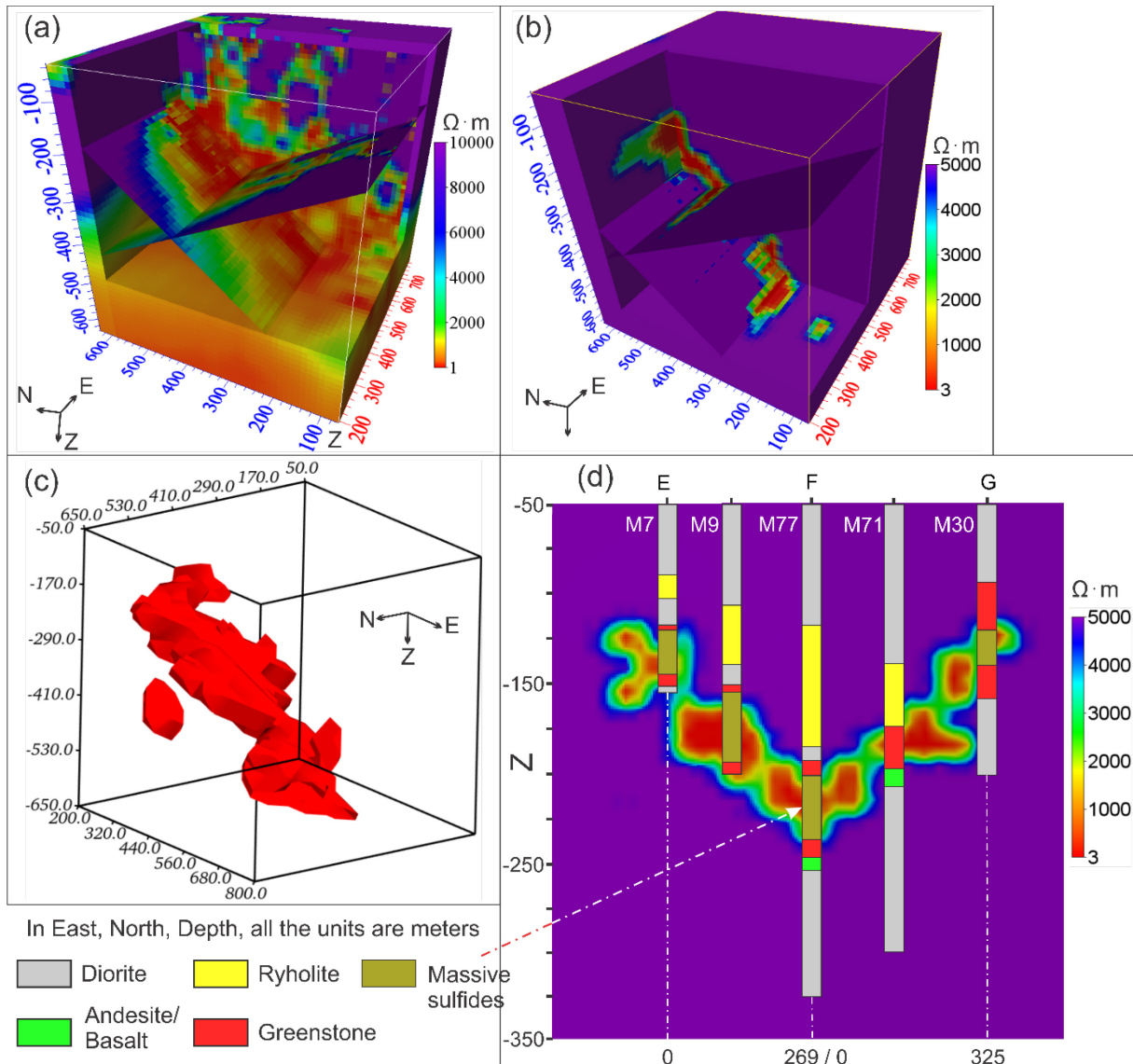


Figure 5.14: Inversion results for the Iso VMS deposit with (a) a 1000  $\Omega \cdot m$  uniform half-space initial model, (b) improvement with isosurface, neighborhood search, 3D trace envelope, and false targets elimination. (c) Interpretation based on the inversion results. (d) The profile E-F (about 269m) through boreholes M7, M9, and M77, and the profile F-G (about 325m) from boreholes M77 to M30.

The inversion result based on a 1,000  $\Omega \cdot m$  uniform half-space initial model recovers the location of the Iso VMS deposit and its downdip extension from north to south, but there are

several false anomalies below the known ore-body and around the boundaries (Figure 5.14a). Combination with geological information and borehole logs, involving the isosurface, neighborhood search, 3D trace envelope, and false targets elimination improves the predicted model during the inversion process, allowing a better delineation of the ore body (Figure 5.14b). The final 3D model (Figure 5.14c) of the Iso VMS deposit delineated by the  $5 \Omega \cdot \text{m}$  isosurface is very close to the true ore-body geometry as its occurrence. (Figure 14d). The inversion model shows a tabular-like conductor (30m to 50m in thickness), dipping to the south about 60 degrees. Compare with the previous study (Cheng et al., 2006), the new inversion result gives better volume estimation.

#### **5.4. Conclusions**

Based on the Gauss-Newton method, we developed a 3D inversion of BHTEM data. The inversion process is adaptive which means that the predicted model can be modified, and improved by introducing the isosurface, neighborhood anomalies search, 3D trace envelope, and false targets elimination during the inversion process to reduce the complexity. Then, a more plausible resistivity model can be achieved.

Although the present method developed as part of our research project was dedicated to BHTEM data inversion, it would be easy to modify and adapt the inversion method to the inversion of other types of EM data. The last case study shows the potential to map good conductors for mineral exploration.

We would like to mention that the 3D trace envelope to delimit the anomalous zones is semi-automatic at present time using the resistivity distribution in the 3D visualization. Automation of this operation will be carried out in our following research.

## CHAPTER 6

### CONCLUSIONS, MAIN CONTRIBUTIONS AND DISCUSSION

The purpose of the Ph.D. research project is

- 1. To improve the efficiency of BHTEM forward modeling using parallel computing and the optimization of simulation.
- 2. To study the impact of different system parameters on TEM responses of conductors, in order to improve the design of measurement protocol for field work.
- 3. To develop a new interpretation tool to map physical models from BHTEM data to deliver more plausible inversion results.

The entire project starts with 3D BHTEM forward modeling, followed by 3D inversion, which involves data pre/post-processing and the development of algorithms. Paralleled *Loki* is carried out in BHTEM forward modeling which benefits the research of the impact of various system parameters as well as the study of the impact of different geological situations on electromagnetic responses. In addition, the efficient and fast forward modeling optimized the calculation of the inversion. We briefly conclude the achievements obtained, as follows.

First, a simple and fast 3D geological model generator is designed, in which the preprocessing and postprocessing of data have been carried out before the BHTEM forward modeling and after inversion. It is a useful tool to help adjust the model to perform the simulation and interpretation timely and easily.

Second, based on MPI and hybrid MPI/OpenMP methods, the parallelization algorithms with multiple meshes are developed to improve the computation efficiency of 3D BHTEM forward modeling. As reducing the number of cells at low frequencies decreases the dimensions of the stiffness matrix, consequently, it makes the forward modeling saving memory and time, we used the multiple meshes strategy in the parallel EM forward modeling. This strategy further improves the computation efficiency after the fast forward modeling made by parallel computing.

Third, the parallel forward modeling was used to analyze the impact of the pulse width, time constant and measurement time on the efficiency of TEM surveys. Those studies allow to establish a new relationship between the pulse width ( $\Delta$ ), the target time constant ( $\tau$ ), and the measurement time ( $t$ ). Under certain conditions, the new formula has been extended to all TEM systems that use square or trapezoidal waveforms. A series of numerical simulations illustrate the consistent behaviors of the surface-borehole, ground and airborne TEM responses. The new relationship is therefore applied to evaluate optimal pulse widths for different off-times for helping TEM survey design.

Finally, a new strategy for 3D inversion of BHTEM data has been developed based on the Gauss-Newton method. Starting the inversion from a uniform half-space model and searching for anomaly zones, the anomaly zones are then delineated using the isosurface and trace envelope from the predicted data after a few iterations. The initial model is modified for the next iteration of the inversion, and the inversion process continues until the best fit between the observed and predicted TEM data is obtained. Tests on synthetic models and on

a field case study show better resolution of the model and faster convergence of the inversion than the inversion results from an uniform initial model.

Looking at the research carried out for this thesis, due to the time limitation, there are still issues to further explore. The developments below will continue within the framework of the research of 3D BHTEM data interpretation.

First, one component (**A**) is considered in the 3D inversion at present time. The three components (**A**, **U**, **V**) will be integrated into the 3D BHTEM inversion to constrain the search direction. Considering the characteristics of different components, of which **A**-component decays slowly and may benefit in recovering the physical properties; and **U**- and **V**-component decay rapidly and are distorted by noise easily, but they may aid the mapping of the shape of conductors. Therefore, the weights can be added to the different components, such as  $\mathbf{d} = \mathbf{A} + \lambda_1\mathbf{U} + \lambda_2\mathbf{V}$ ; it may possible to find the optimal direction of the inversion with more constraints.

Second, the spatial discretization could be made with hexahedral cells automatically. As mentioned above, the regular cells are used to discretize the model, which is not good to fit the complex geological environment. Using hexahedral cells is a desirable way to fit the complex physical model in the forward modeling and also to improve the predicted model in the inversion process.

Third, an automatic method should be investigated for the connection between the parts (isosurface, 3D trace envelope, false targets elimination, and the inversion process) because

it would be a novel approach to improving models and it would be a less subjective process. Therefore, automation of the update of the predicted model for the next step of inversion is necessary. For now, we unite the anomalous bodies together to guide the 3D inversion and achieve better convergence. In the future, more testing will be done on the detection sensitivity of TEM measurements to distinguish a large single source versus an agglomeration of sources. It may be possible to achieve a general conclusion from a large number of tests.

Furthermore, we classify and unite the anomalies according to the spatial distribution of resistivity as a result of inversion, indeed, it is a kind of geological reconstruction. Several geological reconstructions will go to a final model in the inversion process. There are several possible solutions to each inversion iteration, therefore it will be interesting to integrate geological constraints into the reconstruction process in order to approach a more accurate final model. In addition, the impact of the background resistivity on the TEM response and model convergence will be studied, as well as complex models with many more borehole distributions to estimate the limits of the method.

## REFERENCES

- Abubakar, A., Habashy, T.M., Druskin, V. L., Knizhnerman, L., and Alumbaugh, D., 2008. 2.5D forward and inverse modeling for interpreting low-frequency electromagnetic measurements: *Geophysics*, 73(4), p.F165–F177.
- Allard, M., and Milkereit, B., 2007. On the origin of the HTEM species. In *Proceedings of exploration*, Vol. 7, p.355-374.
- Asten, M.W., 1996. Drillhole EM - a strictly scientific Hokey-Pokey. *Exploration Geophysics*, 27(2/3), p.41-49.
- Asten, M.W., King, A., and Peacock, J., 1987. Sign changes in DHEM surveys for cindered coal in the Sydney basin. *Exploration Geophysics*, 18(3), p.319-323.
- Aster, R.C., Borchers, B., and Thurber, C.H., 2011. *Parameter estimation and inverse problems* (Vol. 90). Academic Press.
- Augustin, A.M., Kennedy, W.D., Morrison, H.F., and Lee, K.H., 1989. A theoretical study of surface-to-borehole electromagnetic logging in cased holes. *Geophysics*, 54(1), p.90-99.
- Avdeev, D.B., 2005. Three-dimensional electromagnetic modeling and inversion from theory to application. *Surveys in Geophysics*, 26(6), p.767-799.
- Avdeev, D., and Avdeeva, A., 2009. 3D magnetotelluric inversion using a limited-memory quasi-Newton optimization. *Geophysics*, 74(3), p.F45-F57.
- Avdeeva, A. D., and Avdeev, D. B., 2006. A limited-memory quasi-Newton inversion for 1D magnetotellurics: *Geophysics*, 71(5), p.G191–G196.
- Barnett, C.T., 1984. Simple inversion of time-domain electromagnetic data. *Geophysics*, 49(7), p.925-933.

- Bebendorf, M., 2000. Approximation of boundary element matrices. *Numerische Mathematik*, 86(4), p.565-589.
- Becker, A., DeCarle, R., and Lazenby, P.G., 1984. Simplified prediction of transient electromagnetic response. *Geophysics*, 49(7), p.913-917.
- Bishop, J.R., 1996. DHEM surveys of the 2K area, North Mine, Broken Hill. *Exploration Geophysics*, 27(2/3), p.51-65.
- Bishop, J.R., Lewis, R.J.G., and Macnae, J.C., 1987. Down-hole electromagnetic surveys at Renison Bell, Tasmania. *Exploration Geophysics*, 18(3), p.265-277.
- Boerner, R.U., Ernst, O.G., and Spitzer, K., 2008. Fast 3-D simulation of transient electromagnetic fields by model reduction in the frequency domain using Krylov subspace projection. *Geophysical Journal International*, 173(3), p.766-780.
- Buselli, G., 1977. Transient electromagnetic measurements to late delay times over the Woodlawn ore body. *Exploration Geophysics*, 8(1), p.1-5.
- Buselli, G., and Lee, S.K., 1996. Modelling of drill-hole TEM responses from multiple targets covered by a conductive overburden. *Exploration Geophysics*, 27, p.141-153.
- Cai, H., Cuma, M., and Zhdanov, M.S., 2015. Three-dimensional parallel edge-based finite element modeling of electromagnetic data with field redatuming. In *SEG Technical Program Expanded Abstracts 2015* (p.1012-1017). Society of Exploration Geophysicists.
- Chandra, R., Dagum, L., Kohr, D., Maydan, D., McDonald, J., and Menon, R., 2001. *Parallel Programming in OpenMP*. Morgan Kaufmann Publishers, San Francisco, 249p.
- Chapman, B., Jost, G., and Van Der Pas, R., 2008. *Using OpenMP: Portable Shared Memory Parallel Programming* (Vol. 10). MIT Press, London, 378p.
- Chen, S.D., Lin, J., and Zhang, S., 2012. Effect of transmitter current waveform on TEM response. *Chinese J. Geophys.* 55(2), p.709-716.

Cheng, L.Z., Smith, R.S., Allard, M., Keating, P., Chouteau, M., Lemieux, J., Vallée, M.A., Bois, D., and Fountain, D.K., 2006. Geophysical case study of the Iso and new InSCO deposits, Québec, Canada, part I: data comparison and analysis. *Exploration and Mining Geology*, 15(1-2), p.53-63.

Cheng, L.Z., Smith, R.S., Allard, M., Keating, P., Chouteau, M., Lemieux, J., Vallée, M.A., Bois, D., and Fountain, D.K., 2006. Geophysical case study of the Iso and New InSCO deposits, Québec, Canada, part II: modeling and interpretation. *Exploration and Mining Geology*, 15(1-2), p.65-74.

Chung, Y., Son, J.S., Lee, T.J., Kim, H.J., and Shin, C., 2011. 3D CSEM modeling and inversion algorithms for a surface-to-borehole survey. In 2011 SEG Annual Meeting. Society of Exploration Geophysicists.

Commer, M., and Newman, G.A., 2000. New advances in three-dimensional controlled-source electromagnetic inversion. *Geophysical Journal International* 172(2), p.513-535.

Commer, M., 2003. Three-dimensional inversion of transient-electromagnetic data: A comparative study (Doctoral dissertation, Universität Zu Köln).

Commer, M., and Newman, G. A., 2004. A parallel finite difference approach for 3D transient electromagnetic modeling with galvanic sources. *Geophysics* 69(5), p.1192-1202.

Commer, M., and Newman, G.A., 2006. An accelerated time domain finite difference simulation scheme for three-dimensional transient electromagnetic modeling using geometric multigrid concepts. *Radio Science* 41(03), p.1-15.

Constable, S.C., Parker, R.L., and Constable, C.G., 1987. Occam's inversion: A practical algorithm for generating smooth models from electromagnetic sounding data. *Geophysics*, 52(3), p.289-300.

- Cox, L.H., and Zhdanov, M.S., 2008. Advanced computational methods of rapid and rigorous 3-D inversion of airborne electromagnetic data. *Communications in Computational Physics*, 3(1), p.160-179.
- Cox, L.H., Wilson, G.A., and Zhdanov, M.S., 2010. 3D inversion of airborne electromagnetic data using a moving footprint. *Exploration Geophysics* 41(4), p.250-259.
- Cox, L.H., Wilson, G.A., and Zhdanov, M.S., 2012. 3D inversion of airborne electromagnetic data. *Geophysics* 77(4), p.WB59-WB69.
- Crone, D., 1977. Ground Pulse EM – examples of survey results in the research for massive sulphides and new equipment developments. *Bull. Aust. Soc. Explor. Geophys.*, 8, p.38-42.
- Crone, D., 1979. 37. Exploration for massive sulphides in desert areas using the ground Pulse electromagnetic method.
- CSIRO, 1984. Program OZPLTE user manual. Division of Mineral Physics, Sydney.
- Cull, J.P., 1993. Downhole three component TEM probes. *Exploration Geophysics*, 24(3/4), p.437-442.
- Cull, L.J., Asten, M.J., and Cull, J.P., 1998. Reflection models and ramp response for downhole TEM data. *Exploration Geophysics*, 29(3/4), p.320-323.
- Cuma, M., Zhdanov, M., and Cox, L., 2016. Large-scale parallel 3D inversion of frequency and time-domain AEM data. In *SEG Technical Program Expanded Abstracts 2016* (p.852-856). Society of Exploration Geophysicists.
- Da Silva, N.V., Morgan, J.V., MacGregor, L., and Warner, M., 2012. A finite element multifrontal method for 3D CSEM modeling in the frequency domain. *Geophysics* 77(2), p.E101-E115.

- Dehiya, R., Singh, A., Gupta, P.K., and Israil, M., 2017. Optimization of computations for adjoint field and Jacobian needed in 3D CSEM inversion. *Journal of Applied Geophysics*, 136, p.444-454.
- Deszcz-Pan, M., Lee, K.H., and Morrison, H.F., 1989. One-dimensional least-squares inversion of surface-to-borehole and cross-hole electromagnetic (EM) data. *Earth Sciences Division Annual Report*. 1989, p.149-150
- Dongarra, J.J., Hempel, R., Hey, A.J., and Walker, D.W., 1993. A proposal for a user-level, message passing interface in a distributed memory environment (No. ORNL/TM-12231). Oak Ridge National Lab., TN (United States), 69p.
- Druskin, V., Knizhnerman, L., and Zaslavsky, M., 2009. Solution of large scale evolutionary problems using rational Krylov subspaces with optimized shifts. *SIAM Journal on Scientific Computing*, 31(5), p.3760-3780.
- Duncan, A.C., 1987. Interpretation of down-hole transient EM data using current filaments. *Exploration Geophysics*, 18(1/2), p.36-39.
- Duncan, A.C., and Cull, J.P., 1988. Three-component downhole TEM surveys. *Exploration Geophysics*, 19(1/2), p.51-53.
- Dyck, A.V., Bloor, M., and Vallée, M.A., 1980. User manual for programs PLATE and SPHERE. *Research in Applied Geophysics*, no. 14, Geophysics Laboratory Department of Physics, University of Toronto.
- Dyck, A.W., 1981. A method for quantitative interpretation of wideband drill-hole surveys in mineral exploration. Ph.D., thesis, University of Toronto. Available as research in applied geophysics, no. 23, Geophysics Laboratory Department of Physics, University of Toronto.

Dyck, A.W., and West, G.F., 1984. The role of simple computer models in interpretation of wide-band drill-hole electromagnetic surveys in mineral exploration. *Geophysics*, 49(7), p.957-980.

Dyck, A.V., and Young, R.P., 1985. Physical characterization of rock masses using borehole methods. *Geophysics*, 50(12), p.2530-2541.

Dyck, A., 1991. Drill-Hole Electromagnetic Methods, in Nabighian, M. N., *Electromagnetic Methods in Applied Geophysics*. Society of Exploration Geophysics 3, p.881-930.

Eaton, P.A., and Hohmann, G.W., 1984. The influence of a conductive host on two-dimensional borehole transient electromagnetic responses. *Geophysics*, 49(7), p.861-869.

Egbert, G.D., and Kelbert, A., 2012. Computational recipes for electromagnetic inverse problems. *Geophysical Journal International*, 189(1), p.251-267.

EMIT Electromagnetic Imaging Technology. CSIRO Modules. <https://www.electromag.com.au/csiro.php>. accessed in 2021.

Farquharson, C.G., 1995. Approximate sensitivities for the multi-dimensional electromagnetic inverse problem (Doctoral dissertation, University of British Columbia).

Fitterman, D.V., and Anderson, W.L., 1984. Effect of transmitter turnoff characteristics on transient soundings. In: *Expanded Abstracts with Biographies, 1984 Technical Program, Society of exploration geophysicists' 54th annual international meeting, December 2-6, 1984, Atlanta, Georgia*, p.69-71.

Fitterman, D. V., and Anderson, W. L., 1987. Effect of transmitter turn-off time on transient soundings. *Geoexploration*, 24(2), p.131-146.

Frandsen, P.E., Jonasson, K., Nielsen, H.B., and Tingleff, O., 2004. Unconstrained optimization. Technical University of Denmark, Lecture Note, IMM-LEC-2.

Fraser, D.C., 1974. Survey experience with DIGHEM-AEM system. CIM Bulletin, 67(744), p.97-103.

Fullagar, P.K., 1987. Inversion of downhole TEM data using circular current filaments. Exploration Geophysics, 18(3), p.341-344.

Fullagar, P.K., and Schaa, R., 2014. Fast 3D inversion of transient electromagnetic (TEM) resistive limit data. In SEG Technical Program Expanded Abstracts 2014, p.1827-1831. Society of Exploration Geophysicists.

Fullagar, P.K., Pears, G.A., Reid, J.E., and Schaa, R., 2015. Rapid approximate inversion of airborne TEM. Exploration Geophysics, 46(1), p.112-117.

Fullagar, P.K., 2016. VPem3D user documentation. Fullagar Geophysics Pty Ltd., V3.2, 45 Tahune Crescent, Blackmans Bay, TAS 7052, Australia.

Geonics Limited, 2012. Geophysical instrumentation for exploration and the environment. 12p, 50th anniversary.

Geotech, Evaluating signal to noise and depth investigation of airborne time domain EM systems. [http://www.geotech.ca/documents/VTEM\\_SignaltoNoise.pdf](http://www.geotech.ca/documents/VTEM_SignaltoNoise.pdf), accessed in June 2021.

Graglia, R.D., Wilton, D.R., and Peterson, A.F., 1997. Higher order interpolatory vector bases for computational electromagnetics. IEEE Transactions on Antennas and Propagation 45(3), p.329-342.

Grayver, A.V., Streich, R., and Ritter, O., 2013. Three-dimensional parallel distributed inversion of CSEM data using a direct forward solver. Geophysical Journal International, 193(3), p.1432-1446.

Guptasarma, D., 1982. Computation of the time-domain response of a polarizable ground. Geophysics 47(11), p.1574-1576.

- Grama, A., Kumar, V., Gupta, A., and Karypis, G., 2003. Introduction to Parallel Computing, 2ed ed. Pearson Education, 656p.
- Haber, E., Ascher, U.M., and Oldenburg, D.W., 2000. On optimization techniques for solving nonlinear inverse problems. *Inverse problems*, 16(5), p.1263-1280.
- Haber, E., Ascher, U.M., and Oldenburg, D.W., 2004. Inversion of 3D electromagnetic data in frequency and time domain using an inexact all-at-once approach. *Geophysics*, 69(5), p.1216-1228.
- Haber, E., 2005. Quasi-Newton methods for large-scale electromagnetic inverse problems. *Inverse problems*, 21(1), p.305-323.
- Haber, E., Oldenburg, D.W., and Shekhtman, R., 2007. Inversion of time domain three-dimensional electromagnetic data. *Geophysical Journal International*, 171(2), p.550-564.
- Haber, E., and Schwarzbach, C., 2014. Parallel inversion of large-scale airborne time-domain electromagnetic data with multiple OcTree meshes. *Inverse Problems*, 30(5), p.055011.
- Hohmann, G.W., 1983. Three-dimensional EM modeling. *Geophysical Surveys* 6(1-2), p.27-53.
- Hone, I.G., and Pik, J.P., 1980. SIROTEM down-hole logging, Elura, Cobar, NSW. *Exploration Geophysics*, 11(4), p.170-175.
- Hughes, N.A., and Ravenhurst, W., 1996. Three component DHEM surveying at Balcooma. *Exploration Geophysics*, 27(2/3), p.77-89.
- Ilic, M.M., and Notaros, B.M., 2003. Higher order hierarchical curved hexahedral vector finite elements for electromagnetic modeling. *IEEE Transactions on microwave theory and techniques* 51(3), p.1026-1033.
- Jackson, J.C., Fallon, G.N., and Bishop, J.R., 1996. DHEM at Isa mine. *Exploration Geophysics*, 27(2/3), p.91-104.

- Jin, J.M., 2002. *The Finite Element Method in Electromagnetics*. New York: John Wiley & Sons, 753p.
- Kelbert, A., Egbert, G.D., and Schultz, A., 2008. Non-linear conjugate gradient inversion for global EM induction: resolution studies. *Geophysical Journal International*, 173(2), p.365-381.
- Kelbert, A., Meqbel, N., Egbert, G.D., and Tandon, K., 2014. ModEM: A modular system for inversion of electromagnetic geophysical data. *Computers & Geosciences*, 66, p.40-53.
- Key, K., and Weiss, C., 2006. Adaptive finite-element modeling using unstructured grids: The 2D magnetotelluric example. *Geophysics*, 71(6), p.G291-G299.
- King, A., 1996. Deep drillhole electromagnetic surveys for nickel/copper sulphides at Sudbury, Canada. *Exploration Geophysics*, 27(2/3), p.105-118.
- Knight, J.H., and Raiche, A.P., 1982. Transient electromagnetic calculations using the Gaver-Stehfest inverse Laplace transform method. *Geophysics*, 47(1), p.47-50.
- Kristensson, G., 1983. The electromagnetic field in a layered earth induced by an arbitrary stationary current distribution. *Radio Science*, 18(3), p.357-368.
- Lamontagne, Y., 1975. Applications of wideband time-domain EM measurements in mineral exploration. Ph.D. thesis, Univ. of Toronto.
- Lamontagne, Y., 2007. Deep exploration with EM in boreholes. In *Proceedings of Exploration: Fifth Decennial International Conference on Mineral Exploration*, 7, p.401-415.
- Levy, G.M., and McNeill, J.D., 1984. Transient electromagnetic borehole logging. Technical note TN-15, Geonics Limited.
- Li, J.H., and He, Z.X., 2012. 3D electrical response characteristics modeling for surface-to-borehole vertical electromagnetic walkaway profile. *Shiyou Diqu Wuli Kantan (Oil Geophysical Prospecting)*, 47(4), p.653-664.

- Li, M., Abubakar, A., Liu, J., Pan, G., and Habashy, T.M., 2011. A compressed implicit Jacobian scheme for 3D electromagnetic data inversion. *Geophysics*, 76(3), p.F173-F183.
- Li, Y., 2002. Edge-based finite element simulation of eddy current phenomenon and its application to defect characterization. Ph.D. Dissertation, Iowa State University, Ames, Iowa, 133p.
- Liu, G., 1998. Effect of transmitter current waveform on airborne TEM response. *Exploration Geophysics*, 29(1/2), p.35-41.
- Liu, C., Cheng, L. and Abbassi, B., 2020, 3D parallel surface-borehole TEM forward modeling with multiple meshes: *Journal of Applied Geophysics*, 172, p.103916.
- Liu, C., Cheng, L., and Abbassi, B., 2020. Validation data of parallel 3D surface-borehole electromagnetic forward modeling. *Data in brief*, 29, p.105209.
- Liu, C., Cheng, L., Dai, X., and Diallo, M.C., 2020. Improvement of the Efficiency of Time-Domain Electromagnetic Measurement. *Pure and Applied Geophysics*, p.1-12.
- Liu, Y., and Yin, C., 2016. 3D inversion for multipulse airborne transient electromagnetic data. *Geophysics*, 81(6), p.E401-E408.
- Liu, Y, Yin, C, Ren, X., and Qiu, C., 2016. 3D parallel inversion of time-domain airborne EM data. *Applied Geophysics*, 13(4), p.701-711.
- Liu, Y., Zhang, J., Yin, C., Qiu, C., Zhang, B., Ren, X., and Wang, Q., 2019. GEM3D: A 3D inversion code for geophysical electromagnetic data based on unstructured tetrahedron grid. In *International Workshop on Gravity, Electrical & Magnetic Methods and Their Applications*, Society of Exploration Geophysicists and Chinese Geophysical Society, p.416-419.
- Lu, J.G., 1999. The effect of transmitter waveform on TEM response. *Journal of Henan College of education*, 8(3), p.23-24.

- Luan, X., Di, Q., Xue, G. and Chen, B., 2020. Ground-wire Source TEM 3D Full Time Multinary Inversion Using Adaptive Regulation. *Journal of Environmental and Engineering Geophysics*, 25(3), p.403-413.
- Lytle, R.J., Laine, E.F., Lager, D.L., and Davis, D.T., 1979. Cross-borehole electromagnetic probing to locate high-contrast anomalies. *Geophysics*, 44(10), p.1667-1676.
- Macnae, J., 1980. An Atlas of Primary Fields Due to fixed Transmitter Loop EM Sources. *Research in Applied Geophysics*, 13.
- Macnae, J., 2015. Rapid modeling and inversion of airborne electromagnetic data. *Jour. of Geophysics*, XXXVI(2), p.63-70.
- Macnae, J., and Staltari, G., 1987. Classification of sign changes in borehole TEM decays. *Exploration Geophysics*, 18(3), p.331-339.
- Madsen, K., Nielsen, H.B., and Tingleff, O., 2004. Methods for non-linear least squares problems. Technical University of Denmark, IMM-DTU.
- Major, J.A., 1984. Down-hole TEM Response in the Presence of a Conductive Overburden. Canberra: Austral. Gov. publ. service.
- Malmqvist, L., Pantze, R., Kristensson, G., and Karlsson, A., 1990. Electromagnetic fields in boreholes-measurements and theory in three dimensions. Technical Report LUTEDX/(TEAT-7008)/1-17/(1990).
- McGillivray, P.R., and Oldenburg, D.W., 1990. Methods for calculating Fréchet derivatives and sensitivities for the non-linear inverse problem: A comparative study. *Geophysical Prospecting*, 38(5), p.499-524.
- McGillivray, P.R., Oldenburg, D.W., Ellis, R.G., and Habashy, T.M., 1994. Calculation of sensitivities for the frequency-domain electromagnetic problem. *Geophysical Journal International*, 116(1), p.1-4.

McNeill, J.D., Edwards, R.N., and Levy, G.M., 1984. Approximate calculations of the transient electromagnetic response from buried conductors in a conductive half-space. *Geophysics*, 49, p.918-924.

Menke, W., 1989. *Geophysical data analysis: discrete inverse theory*. Academic Press.

Midtgård, O.M., 1997. Construction and assessment of hierarchical edge elements for three-dimensional computations of eddy currents. Ph.D. Dissertation, Norwegian University of Science and Technology, Trondheim, Norway, 139p.

Minami, T., and Toh, H., 2012. An improved forward modeling method for two-dimensional electromagnetic induction problems with bathymetry, *Earth, Planets Space*, 64, p.e9-e12.

Mienseopust, M.P., Queralt, P., Jones, A.G., and 3D MT modellers, 2013. Magnetotelluric 3-D inversion—a review of two successful workshops on forward and inversion code testing and comparison. *Geophysical Journal International*, 193(3), p.1216-1238.

Mogilatov, V.S., Antonov, E.Y. and Shein, A.N., 2019. 3D Tomographic Inversion of TEM Sounding Data. *Russian Geology and Geophysics*, 60(1), p.97-107.

Mutton, A.J., 1987. Applications of downhole SIROTEM surveys in the Agnew Nickel Belt, WA. *Exploration Geophysics*, 18(3), p.295-303.

Nabighian, M.N., 1988. *Electromagnetic Methods in Applied Geophysics: Theory*. Volume 1, Tulsa, Oklahoma: Society of Exploration Geophysicists, 531p.

Nédélec, J.C., 1980. Mixed finite elements in  $R^3$ . *Numerische Mathematik* 35(3), p.315-341.

Nabighian, M.N., and Macnae, J.C, 1991. Time domain electromagnetic methods. In Nabighian, M.N., ed., *Electromagnetic methods in applied geophysics: Application, parts A and B: Volume 2*. Tulsa, Oklahoma: Society of Exploration Geophysicists. p.427-520.

Napier, S., 2007. Practical inversion of 3D time domain electromagnetic data (Doctoral dissertation, University of British Columbia).

Newman, G.A., Hohmann, G.W., and Anderson, W.L., 1986. Transient electromagnetic response of a three-dimensional body in a layered earth. *Geophysics*, 51(8), p.1608-1627.

Newman, G.A., and Hohmann, G.W., 1988. Transient electromagnetic responses of high-contrast prisms in a layered earth. *Geophysics*, 53(5), p.691-706.

Newman, G.A., Anderson, W.L., and Hohmann, G.W., 1989. Effect of conductive host rock on borehole transient electromagnetic responses. *Geophysics*, 54(5), p.598-608.

Newman, G.A., and Alumbaugh, D.L., 1997. Three-dimensional massively parallel electromagnetic inversion - I. Theory. *Geophysical journal international*, 128(2), p.345-354.

Newman, G.A., and Alumbaugh, D.L., 2000. Three-dimensional magnetotelluric inversion using non-linear conjugate gradients. *Geophysical journal international*, 140(2), p.410-424.

Newman, G.A., and Boggs, P.T., 2004. Solution accelerators for large-scale three-dimensional electromagnetic inverse problems. *Inverse Problems*, 20(6), p.S151-S170.

Oldenburg, D.W., 1990. Inversion of electromagnetic data: An overview of new techniques. *Surveys in Geophysics*, 11(2), p.231-270.

Oldenburg, D.W., and Pratt, D.A., 2007. Geophysical inversion for mineral exploration: A decade of progress in theory and practice. In *Proceedings of Exploration 07: Fifth Decennial International Conference on Mineral Exploration*, p.61-95.

Oldenburg, D.W., Heagy, L.J., Kang, S., and Cockett, R., 2020. 3D electromagnetic modeling and inversion: a case for open source. *Exploration Geophysics*, 51(1), p.25-37.

Oristaglio, M.L., and Worthington M.H., 1980. Inversion of surface and borehole electromagnetic data for two-dimensional conductivity models, *Geophysical Prospecting* 28(4), p.633-657.

Pacheco, P., and Ming, W., 1995. *MPI User's Guide in Fortran*. Department of Mathematics, University of San Francisco, San Francisco, CA, 51p.

Pardo, D., Torres-Verdín, C., and Zhang, Z., 2008. Sensitivity study of borehole-to-surface and crosswell electromagnetic measurements acquired with energized steel casing to water displacement in hydrocarbon-bearing layers. *Geophysics*, 73(6), p.F261-F268.

Puzyrev, V., Koldan, J., de la Puente, J., Houzeaux, G., Vázquez, M., and Cela, J.M., 2013. A parallel finite-element method for three-dimensional controlled-source electromagnetic forward modeling. *Geophysical Journal International* 193, p.678-693.

Qin, Q.Y., 2013. Effect of transmitter current waveform variation on the fixed-wing airborne transient electromagnetic response. *Progress in Geophys. (in Chinese)*, 28(5), p.2673-2679.

Raiche, A. P., 1984. The effect of ramp function turn-off on the TEM response of layered earth. *Exploration Geophysics*, 15(1), p.37-41.

Raiche, A.P., and Bennett, L.A., 1987. Layered earth models using downhole electromagnetic receivers. *Exploration Geophysics*, 18(3), p.325-329.

Raiche, A., Sugeng, F., and Soininen, H., 2003. Using the Loki 3D edge-finite-element program to model EM dipole-dipole drill-hole data. *ASEG Extended Abstracts*, 2003(2), p.1-4.

Raiche, A., Sugeng, F., and Wilson, G., 2007. Practical 3D EM inversion? The P223F software suite. *ASEG Extended Abstracts*, 2007(1), p.1-5.

Raiche, A., and Sugeng, F., 2008. Report – P223 EM modeling projects. AMIRA International.

Ren, X., Yin, C., Macnae, J., Liu, Y., and Zhang, B., 2018. 3D time-domain airborne electromagnetic inversion based on secondary field finite-volume method. *Geophysics*, 83(4), p.E219-E228.

Reyes, O.C., de la Puente, J., Puzyrev, V., and Cela, J.M., 2015. Edge-based electric field formulation in 3D CSEM simulations: a parallel approach. In Computing and Communication (IEMCON), 2015 International Conference and Workshop on, IEEE, p.1-8.

Richards, D.J., 1987. CRAE's approach to downhole TEM at Broken Hill. *Exploration Geophysics*, 18(3), p.279-284.

Rodi, W., and Mackie, R.L., 2001. Nonlinear conjugate gradients algorithm for 2-D magnetotelluric inversion. *Geophysics*, 66(1), p.174-187.

SanFilipo, W.A., and Hohmann, G.W., 1985. Integral equation solution for the transient electromagnetic response of a three-dimensional body in a conductive half-space. *Geophysics*, 50(5), p.798-809.

Sasaki, Y., 1994. 3-D resistivity inversion using the finite-element method. *Geophysics*, 59(11), p.1839-1848.

Sasaki, Y., 2001. Full 3-D inversion of electromagnetic data on PC. *Journal of Applied Geophysics*, 46(1), p.45-54.

Sato, T., Osato, K., Takasugi, S., and Uchida, T., 1996. Development of the multi-reguency array induction logging (MAIL) tool. *Geothermal resources council transactions*, 20(9), p.637-642.

Schmidt, K., and Cull, J., 1995. Application of Euler deconvolution and a neural network system as interpretation aids for three component downhole TEM data. *Exploration Geophysics*, 26(2/3), p.154-157.

Singh, A., Dehiya, R., Gupta, P.K., and Israil, M., 2017. A MATLAB based 3D modeling and inversion code for MT data. *Computers & Geosciences*, 104, p.1-11.

Siripunvaraporn, W., 2012. Three-dimensional magnetotelluric inversion: an introductory guide for developers and users. *Surveys in geophysics*, 33(1), p.5-27.

- Smith, R., 1998. On the effect of varying the pulse width to detect high conductance bodies. *Exploration Geophysics*, 29(1/2), p.42-45.
- Snieder, R., and Trampert, J., 1999. Inverse problems in geophysics. In *Wavefield inversion* (p.119-190). Springer, Vienna.
- Stalnaker, J., Everett, M.E., Benavides, A., and Pierce, C.J., 2006. Mutual inductance and the effect of host conductivity on EM induction response of buried plate targets using 3-D finite element analysis, *IEEE Trans Geosci Remote Sens*, 44, p.251-259.
- Stolz, E.M., 2003. Direct detection of gold bearing structures at St Ives, WA—DHEM vs DHMMR. *Exploration Geophysics*, 34(1/2), p.131-136.
- Sugeng, F., and Raiche, A., 2004. Modeling the electromagnetic response in complex geological structures using the 3D finite-element method based on the hexahedral and the tetrahedral edge-element technique. *ASEG Extended Abstracts 2004*(1), p.1-4.
- Sunwall, D., Cox, L., and Zhdanov, M., 2013. Joint 3D inversion of time-and frequency-domain airborne electromagnetic data. In *SEG Technical Program Expanded Abstracts 2013*, p.713-717. Society of Exploration Geophysicists.
- Sun, X.Y., and Nie, Z.P., 2008. Vector finite element analysis of multicomponent induction response in anisotropic formations. *Progress in Electromagnetics Research* 81, p.21-39.
- Tan, H., Tong, T., and Lin, C., 2006. The parallel 3D magnetotelluric forward modeling algorithm. *Applied Geophysics* 3(4), p.197-202.
- Telford, W.M., and Becker, A., 1979, Exploration case histories of the Iso and New Inscro ore bodies, in Hood, P.J., ed., *Geophysics and Geochemistry in the search for metallic ores: Geological Survey of Canada, Economic Geology*, report 31, p.605–629.
- Tikhonov, A.N., and Arsenin, V.I., 1977. *Solutions of ill-posed problems*. V.H. Winston & Sons.

- Thomas, L., 1987. Short note: A simple interpretation aid for downhole time-domain electromagnetic anomalies. *Exploration Geophysics*, 18(3), p.349-351.
- Tweeton, D.R., Hanson, J.C., Friedel, M.J., Sternberg, B.K., and Dahl, L.J., 1994. A field test of electromagnetic geophysical techniques for locating simulated in situ mining leach solution. Report of investigations 9505, United States Department of the Interior and Bureau of mines.
- Um, E.S., Harris, J.M., and Alumbaugh, D.L., 2012. An iterative finite element time-domain method for simulating three-dimensional electromagnetic diffusion in earth. *Geophysical Journal International* 190(2), p.871-886.
- Wang, G.L., Torres-Verdín, C., Salazar, J.M., and Voss, B., 2009. Fast 2D inversion of large borehole EM induction data sets with an efficient Fréchet-derivative approximation. *Geophysics*, 74(1), p.E75-E91.
- Wang, M., Tan, H., Yao, C., Yang, M., and Ma, H., 2015. A study on parallel computation based on forward modeling and inversion algorithm of 2D magnetotelluric. In *Ubiquitous Intelligence and Computing and 2015 IEEE 12th Intl Conf on Autonomic and Trusted Computing and 2015 IEEE 15th Intl Conf on Scalable Computing and Communications and Its Associated Workshops (UIC-ATC-ScalCom)*, 2015 IEEE 12th Intl Conf on. IEEE, p.589-594.
- Wilkinson, B., and Allen, M., 2004. *Parallel Programming: Techniques and Applications Using Networked Workstations and Parallel Computers*, 2ed ed. Prentice-Hall, Inc. Upper Saddle River, 496p.
- Wilson, G.A., Raiche, A.P., and Sugeng, F., 2006. 2.5 D inversion of airborne electromagnetic data. *Exploration Geophysics*, 37(4), p.363-371.

Wilt, M.J., Morrison, H.F., Becker, A., and Lee, K.H., 1991. Cross-borehole and surface-to-borehole electromagnetic induction for reservoir characterization (No. DOE/BC-91002253). Lawrence Livermore National Lab., CA (United States).

Wilt, M.J., Alumbaugh, D.L., Morrison, H.F., Becker, A., Lee, K.H., and Deszcz-Pan, M., 1995. Crosswell electromagnetic tomography: System design considerations and field results. *Geophysics*, 60(3), p.871-885.

Wilt, M, Lee, K H, Becker, A, Spies, B, and Wang, B., 1996. Crosshole EM in steel-cased boreholes. In SEG Technical Program Expanded Abstracts, Society of Exploration Geophysicists, p.230-233.

Woods, D.V., 1975. A model study of the Crone borehole pulse electromagnetic (PEM) system. M.Sc. thesis, Queens University, Kingston, Ontario, Canada.

Woods, D.V., and Crone, J.D., 1980. Scale model study of a borehole pulse electromagnetic system. *Can. Min. and Metall. Bull.*, May, 73(817), p.96-104.

Yang, D., Oldenburg, D.W., and Haber, E., 2013. 3-D inversion of airborne electromagnetic data parallelized and accelerated by local mesh and adaptive soundings. *Geophysical Journal International*, 196(3), p.1492-1507.

Yang, Y.J., Wang, X.B., Liu, X.J., Mi, X.L. and Mao, L., 2020. A three-dimensional transient electromagnetic data inversion method based on a time-frequency transformation. *Applied Geophysics*, 17(3), p.361-376.

Yin, C., Huang, X., Liu, Y., and Cai, J., 2014. Footprint for frequency-domain airborne electromagnetic systems. *Geophysics* 79(6), p.E243-E254.

Yin, W.L., 2010. Study and application on higher order vector FEM in electromagnetic field. Ph.D. Dissertation, National University of Defense Technology, Changsha, Hunan, China, 139p.

Zaslavsky, M., Druskin, V., Abubakar, A., Habashy, T., and Simoncini, V., 2013. Large-scale Gauss-Newton inversion of transient CSEM data using the model order reduction framework. *Geophysics*, 78(4), p.E161-E171.

Zhang, Z., and Xiao, J., 2001. Inversions of surface and borehole data from large-loop transient electromagnetic system over a 1-D earth. *Geophysics*, 66(4), p.1090-1096.

Zhdanov, M.S., and Tartaras, E., 2002. Three-dimensional inversion of multitransmitter electromagnetic data based on the localized quasi-linear approximation. *Geophysical Journal International*, 148(3), p.506-519.

Zhdanov, M. S., 2002, *Geophysical inverse theory and regularization problems*: Elsevier.

Zhdanov, M.S., and Chernyavskiy, A., 2004. Rapid three-dimensional inversion of multi-transmitter electromagnetic data using the spectral Lanczos decomposition method. *Inverse Problems*, 20(6), p.S233-S256.